

Tungsten Transport in the Plasma Edge at ASDEX Upgrade



Der Fakultät für Physik
der Ludwig-Maximilians-Universität München
zur Erlangung des akademischen Grades eines
Doktors der Naturwissenschaften (Dr. rer. nat.)
vorgelegte Dissertation

von

Michael Arthur Janzer

München, den 04 Februar 2015

Erstgutachter: Prof. Dr. Hartmut Zohm

Zweitgutachter: Prof Dr. Harald Lesch

Tag der mündlichen Prüfung: 30.04.2015

Zusammenfassung

Die dem Plasma ausgesetzten Wandkomponenten werden eine entscheidende Rolle in einem zukünftigen Fusionskraftwerk, das Deuterium- und Tritium-Ionen magnetisch einschließt, spielen, da sie enormen Teilchen- und Energieflüssen widerstehen und gleichzeitig ein geringes Tritium Rückhaltevermögen aufweisen müssen. Diese Anforderungen werden höchstwahrscheinlich den Einsatz von hoch-Z Materialien wie z.B. Wolfram notwendig machen, denn sie weisen sehr gute Erosionseigenschaften auf und speichern nur wenig Tritium. Allerdings emittieren diese Materialien starke Linienstrahlung im Plasmazentrum, welche als effizienter Energieverlustmechanismus wirkt. Daher muss die Konzentration dieser Elemente kontrolliert und auf niedrigem Niveau gehalten werden, um ein selbständig brennendes Plasma zu erreichen. Dabei ist es essentiell die Transportphänomene im Plasmarand zu verstehen, um die richtigen Kontrollmechanismen einzusetzen. Diese Kontrollmechanismen umfassen zum einen die Erhöhung des Verunreinigungsausflusses, z.B. durch randlokalisierte Moden (ELM), da diese Verunreinigungen aus dem Hauptplasma austossen, zum anderen eine Reduktion der Erosionsflüsse oder eine Erhöhung des Abschirmeffekts der Abschältschicht (SOL). ASDEX Upgrade (AUG) ist seit mehreren Jahren erfolgreich mit einer Wandverkleidung aus Wolfram in Betrieb und bietet die Möglichkeit diese Randtransportprozesse zu untersuchen. Diese Arbeit konzentriert sich auf die Entflechtung von Typ-I ELMs und der Gasinjektionsrate im Hauptraum, zwei Parametern, die normalerweise in "H-mode" Entladungen gekoppelt sind. Solch eine Trennung erlaubte zum ersten Mal eine direkte Untersuchung des Einflusses jedes einzelnen Parameters auf die Wolframkonzentration. Die ELM-Frequenz wurde kontrolliert, indem die obere Triangularität, also die Plasmaform angepasst wurde.

Der radiale Wolframtransport wurde untersucht, indem man eine modulierte Wolframquelle implementierte. Um diese zu erzeugen wurde die lineare Abhängigkeit der Erosionsrate an den Limitern der Ionen-Zyklotron-Resonanz-Heizung (ICRH) von der eingespeisten ICRH-Leistung benutzt. Die Phase und Amplitude des sich ausbreitenden Wolframsignals wurde dann an der Erosionsstelle und an drei radialen Positionen im Hauptplasma beobachtet. Zwei dieser Positionen wurden im Verlauf dieser Arbeit durch eine genaue Untersuchung des Wolframspektrums im Vakuum-Ultra-Violett (VUV)-Spektralbereichs identifiziert. Diese liegen genau im Bereich der steilen Gradienten nahe der Randbarriere und etwas weiter innen im AUG-Plasma. Darüberhinaus wurden die parallelen Flüsse in der SOL mit spektroskopischen Mitteln als auch mit Langmuir-Sonden gemessen.

Die experimentellen Ergebnisse waren überraschend, da die ELM-Frequenz keinen Einfluss auf die Wolframkonzentration ausübte und nur die Gasinjektionsrate diese Grösse beeinflusste. Die Auswertung des modulierten Wolframsignals ergab, dass weder das Gasblasen noch die Plasmaform einen messbaren Einfluss auf radialen Transportprozesse von Wolfram hatte. Ausserdem waren die Wolframquellen nur zu einem kleinen Teil für das beobachtete Wolframverhalten verantwortlich. Diese Beobachtungen führten zu einem simplen Modell, welches den Wolframausfluss mit dem Wolframzufluss ausgleicht. In diesem Modell ist der Wolframausstoss durch ELMs nicht diffusiv sondern turbulent und an die Grösse der ELMs gekoppelt. Aus diesem Modell folgte eine lineare Abhängigkeit zwischen der Wolframkonzentration und der parallelen Geschwindigkeit in der SOL. Diese lineare Abhängigkeit wurde durch die spektroskopischen Untersuchungen der SOL-Flüsse bestätigt.

Abstract

The Plasma Facing Components (PFC) will play a crucial role in future deuterium-tritium magnetically confined fusion power plants, since they will be subject to high energy and particle loads, but at the same time have to ensure long lifetimes and a low tritium retention. These requirements will most probably necessitate the use of high-Z materials such as tungsten for the wall materials, since their erosion properties are very benign and, unlike carbon, capture only little tritium. The drawback with high-Z materials is, that they emit strong line radiation in the core plasma, which acts as a powerful energy loss mechanism. Thus, the concentration of these high-Z materials has to be controlled and kept at low levels in order to achieve a burning plasma. Understanding the transport processes in the plasma edge is essential for applying the proper impurity control mechanisms. This control can be exerted either by enhancing the outflux, *e.g.* by Edge Localized Modes (ELM), since they are known to expell impurities from the main plasma, or by reducing the influx, *e.g.* minimizing the tungsten erosion or increasing the shielding effect of the Scrape Off Layer (SOL). ASDEX Upgrade (AUG) has been successfully operating with a full tungsten wall for several years now and offers the possibility to investigate these edge transport processes for tungsten. This study focused on the disentanglement of the frequency of type-I ELMs and the main chamber gas injection rate, two parameters which are usually linked in H-mode discharges. Such a separation allowed for the first time the direct assessment of the impact of each parameter on the tungsten concentration. The control of the ELM frequency was performed by adjusting the shape of the plasma, *i.e.* the upper triangularity.

The radial tungsten transport was investigated by implementing a modulated tungsten source. To create this modulated source, the linear dependence of the tungsten erosion rate at the Ion Cyclotron Resonance Heating (ICRH) limiters on the injected ICRH power was used. The phase and amplitude of the inwardly propagating tungsten signal was then observed at the erosion site and at three radial positions in the main plasma, from which two were identified in the course of this work by a thorough investigation of the tungsten radiation features in the Vacuum Ultra-Violet (VUV) spectral range. The newly found observation sites are located right in the steep gradient region, close to the Edge Transport Barrier (ETB) and slightly further inside at the pedestal top of AUG H-mode discharges. Furthermore, the parallel flows in the SOL have been monitored by spectroscopical means and Langmuir probes.

The experimental results were quite unexpected, since the ELM frequency had no influence on the tungsten concentration, and the sole actuator on this quantity was the gas injection rate. The evaluation of the modulated tungsten signal revealed that neither gas puffing nor plasma shape had an measureable influence on the radial tungsten transport processes. In addition, the tungsten erosion sources were only partially responsible for the observed tungsten behavior. These observations inspired a simple model, which balanced the tungsten outflux with the tungsten influx. In this model the impurity exahst by ELMs is not diffusive, but turbulent and linked to the ELM size. The model predicted a linear dependence between the tungsten concentration and the parallel velocity in the SOL. This linear dependence was confirmed by the spectroscopical evaluation of the SOL parallel flows.

Contents

1	Introduction	1
1.1	Magnetically Confined Fusion	3
1.2	Burn Condition and Impurities	5
1.3	Thesis Motivation	7
1.3.1	Classical and Neoclassical Transport	10
2	Tungsten Diagnostics	16
2.1	Tungsten Erosion measurements	16
2.1.1	SXB Method and Corona Model	16
2.1.2	Visible Light Spectrometer System	19
2.2	Tungsten Radiation from the Plasma Edge and Core Plasma	22
2.2.1	VUV-spectrometer SPRED	22
2.2.2	Absolute Intensity Calibration of SPRED spectrometer	25
2.3	Tungsten Concentration Measurements	26
2.3.1	Radiation from Highly Charged Tungsten	27
2.3.2	Grazing Incidence VUV-spectrometer	28
2.4	Detector Systems	29
3	VUV Tungsten Spectra in the Plasma Edge	33
3.1	Characterisation via Tungsten Accumulation	33
3.2	Characterisation via Tungsten-LBO	41
3.3	Comparison with other experiments and calculations	50
4	Probing of W-transport with a Modulated W-source	57
4.1	Using ICRH for the W-erosion modulation	57
4.2	Experimental Setup, Decoupling of Gas Puff and ELM frequency	59
4.3	STRAHL Predictions	61
4.3.1	ELM-free Transport Calculations	62
4.3.2	Transport Calculations regarding ELMs	66
5	Experimental Results	74
5.1	Dependence of W-concentration on Gas Puff and Triangularity	74
5.2	Evaluation of Phase Lag and Relative Amplitude	83
5.2.1	Edge Profiles and their dependence on Gas Puff and Triangularity	85
5.3	Simple 0-D Model for W-transport	89

5.4	Influence of gas puffing on SOL flows	92
5.4.1	Spectroscopic measurements of SOL flows on the HFS	94
5.4.2	Langmuir probe measurements of SOL flows on the LFS	101
6	Conclusion and Outlook	108

Chapter 1

Introduction

With the beginning of the industrial age the economic development was tied to the availability of cheap energy. As a result, these days the "western" economy and lifestyle demand a very high input of primary energy sources. Their energy consumption per capita and in total is a multiple of what developing countries consume. Since the late eighties of the 20th century China, India and other newly industrializing countries have entered the path to an economic development, that will lead them to a standard of living comparable to the industrialized countries. The impact of this development on their energy consumption is already tremendous. In the year 2009 China has surpassed the USA in terms of total energy consumption [1]. However, considering the Chinese per capita energy consumption which is still only 1/5 of the American one, the huge requirements to the future energy supply systems become obvious.

The present day energy needs are covered mainly by burning fossile fuels like coal, oil or natural gas. However, these fuels come with a bundle of problems. On the one hand there is the localization of oil or natural gas. The main deposits are located in politically unstable regions like the Middle East imposing a threat on the reliability of supply. On the other hand there is the problem of dwindling resources in case of natural gas and especially oil [2]. Besides the problems of localization and the impending scarcity, the CO₂ exhaust caused by burning these fuels is the major problem. The continuous use of fossile fuels threatens to trigger a climatic change. It is recognized that the increase of CO₂ levels in the earth's atmosphere promote the 'green house' effect, leading to an increase of the average temperature [3] and references therein. This climatic change is expected to have a worldwide negative impact on many regions and their inhabitants. It is therefore inevitable to search for ways to reduce the worldwide CO₂ production.

There are several approaches which are considered feasible in reducing green house gas output. The most obvious one is the reduction of energy consumption in the first place. This can be reached by either the lowering of the standard of living which is a very unfavourable and unlikely scenario, or by increasing the energy efficiency, e.g. proper insulation of houses, enhanced public transportation systems etc. The costs for the envisaged efficiency gain would be considerable; hundreds of billions of Euro only for the thermal insulation of the buildings in Germany [4]. It is understood, that in the present short-term profit oriented economy these kind of investements are avoided. An appropriate charge on the emitted amount of CO₂ would most probably have the strongest reduction effect on the consumption of energy from fossile fuels. However, the system of CO₂ certificates initialised in the past years does not seem to have a significant impact on the consumption of fossil fuels. This

statement follows from the predicted doubling of the energy consumption until 2035 as compared to the value from the year 2007 [5].

With a constantly increasing energy demand comes the need to identify alternative energy sources with a low carbon footprint. As it is, there are three possible candidates: renewables, nuclear fission and nuclear fusion. The renewable energies hold the potential to provide energy with a very low CO₂ output and a low risk of environmental hazards. For example, the use of water and wind as an energy source dates back to pre-industrial times, but is now only of marginal importance to the worldwide energy output [6]. Nevertheless, the rising costs for fossile fuels and additional subsidies might make new offshore wind power or large scale solar thermal facilities a profitable investment, therefore increasing the fraction of renewable energies. One problem of the renewable energy sources is their reliability which is a matter of weather conditions for most of the renewables. This calls for the implementation of large scale energy storage capacity with good efficiency and fast response times. At the moment this is still a matter of ongoing research and will be a major point when it comes to large scale application of renewables. Another problem is the location of energy production far off the economic centers of energy consumption, e.g. offshore wind mills in the North Sea are located hundreds of kilometers away from the industrial areas in Germany. The distances between producer and consumer for the scheduled Desertec project (production of solar thermal electricity in the northern Sahara) are even larger and make the use of new power cables inevitable [7]. All in all the renewables are an option, that, even though it most probably will not be able to provide 100% of the demanded energy, will add a good share to the energy output in the future.

The second candidate, nuclear fission, is nearly CO₂ free, but poses other threats to the environment. The 2011 Japan earthquake revealed that even in highly developed countries this technology is prone to failure under certain, extreme environmental conditions. In addition to these external conditions, there is the internal human factor to this technology. It is a source for errors which in the end can lead to major incidents, as showed the Chernobyl accident in 1985 [8]. There are still other unsolved problems to this energy source, as for example the waste disposal which in combination with the risk of large scale radioactive contamination, have led to a very low acceptance of this technology in the population of countries like Germany and Japan. Seen in this light, it is preferable, that this energy source will play a minor role in the future.

The last candidate is nuclear fusion. The power plants envisaged for the near future will most probably use the hydrogen isotopes deuterium (D) and tritium (T) for fuel. As deuterium can be extracted from sea water - the natural isotopic abundance is $\approx 0.015\%$ - its fuel capacities are almost infinite at the current energy consumption. Due to its short half life of 12 years, there are no natural tritium deposits. Therefore, it has to be produced on site by breeding it from lithium (Li). The lithium resources in the earth's crust are quite limited and only the utilization of the lithium from seawater (0.17 ppm) would make this a truly abundant fuel [9]. Furthermore, there is no radioactive waste or environmental risk of large scale contamination with long lived radioactive isotopes involved with this technology. Although the reactor materials themselves will be activated by the high neutron fluxes during power plant operation, the application of new materials, e.g. ferritic-martensitic steels should reduce the time window for reaching the hands-on limit to 100 – 150 years. This technology would combine low environmental risks, fuel abundance and reliability and, together with the renewables, would ensure the high standard of living not only for the already industrialized countries, but also for the ones stepping up now.

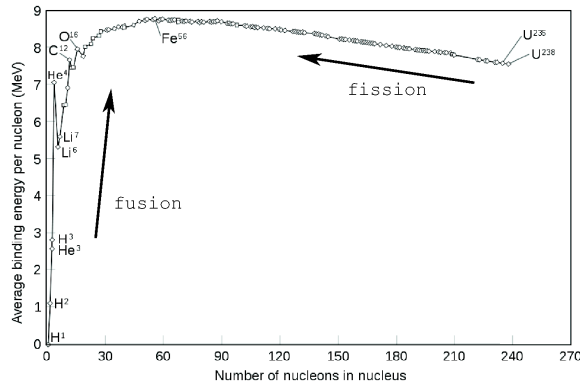


Figure 1.1: Average binding energy per nucleon versus mass number for various elements

1.1 Magnetically Confined Fusion

Fission as well as fusion power plants harvest the kinetic energy released in the nuclear processes. This kinetic energy is transferred from the very fast moving reaction products, carrying several MeV of energy, to some coolant. The coolant releases the heat to produce steam which is used to drive the turbines and subsequently generate electrical power. The steps from steam production to electricity are the same for all thermal power plants. It is the initial step, the primary reaction, that makes nuclear power so much different than conventional power. The reaction products from conventional power have kinetic energies in the range of eV which is a factor of 10^{-6} smaller than the values for the nuclear reactions.

The fact that fusing two light nuclei to a heavier one, or splitting one heavy nucleus into two lighter ones releases energy, is due to the dependence of the binding energy per nucleon on the mass of the nucleus. This relation is shown in 1.1. It exhibits a peak at iron (${}^{56}_{26}\text{Fe}$) which means that this nucleus represents the most stable configuration of neutrons and protons. Fusing D and T results in the production of a neutron (n) and a helium (${}^4_2\text{He}$) nucleus and, what is the most important, releases with the reaction products a total of 17.6 MeV:



Besides fusing D and T there are other options available for the fusion process in principle:



That these options are not considered for the first generation of fusion power plants has reasons, that will be explained further below.

The fast alpha particles (He-nuclei) remain inside the plasma and transfer their energy to the surrounding particles via Coulomb collisions, therefore heating the plasma, while the neutrons leave the production site. They carry the main part of the released energy and have to be used for tritium breeding. The reactions leading from Li to tritium are well understood:



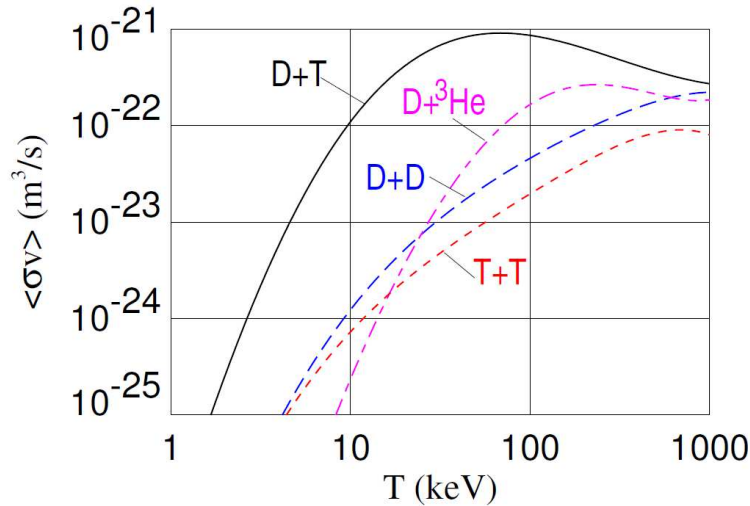


Figure 1.2: *Temperature dependence of the reaction parameter for some fusion processes. (figure from [11])*



However, the details of the technical implementation, especially regarding the aspect of neutron capture efficiency are still a pressing issue. For example, using only ${}^6_3\text{Li}$ would implicate that 100% of the produced neutrons would have to undergo the breeding reaction. Clearly, this is technically unachievable. The use of neutron multipliers and a mix of ${}^6\text{Li}$ and ${}^7\text{Li}$ would be a possible solution, but both would have to be positioned just behind the first wall to ensure as little as possible attenuation of the neutron flux from the plasma. At the same time the coolant has to be able to reach the first wall in order to protect it from damage by overheating. These are two contradicting requirements which should present exemplary one of the many difficulties that have to be overcome on the way to an efficient breeding process. Naturally, this is one of the problems that will have to be addressed by the International Thermonuclear Experimental Reactor (ITER), the next generation experimental reactor [10].

As was shown above, the reaction of D and T is not the only one to produce He (see equations 1.2-1.4). Yet, it is the process that exhibits the highest reaction rates at feasible plasma temperatures which is the result of a resonance in the unstable ${}^5_2\text{He}$ nucleus. Feasible plasma conditions in this context translates to a few 10 keV. Only at these high temperatures can the D and T ions overcome the Coulomb repulsion and undergo the fusion process with a sufficiently high probability. Present day tokamak experiments reach the needed plasma temperatures and enter a region in which the reaction parameter of D and T reaches a maximum as depicted in figure 1.2. This is also the temperature range in which a future fusion power plant is designed to work and the choice for the D-T reaction is straight forward, since at these temperatures it is by one order of magnitude higher than any of the other possible reactions.

The scheme of magnetically confined fusion (MCF) is to confine the charged particles of a hot (10 – 20 keV), moderately dense (10^{20} m^{-3}) D-T plasma via the Lorentz force exerted by magnetic fields. There are many possibilities for the configuration of the magnetic fields, each with its advantages and disadvantages. At the moment the toroidal configuration is the most feasible with

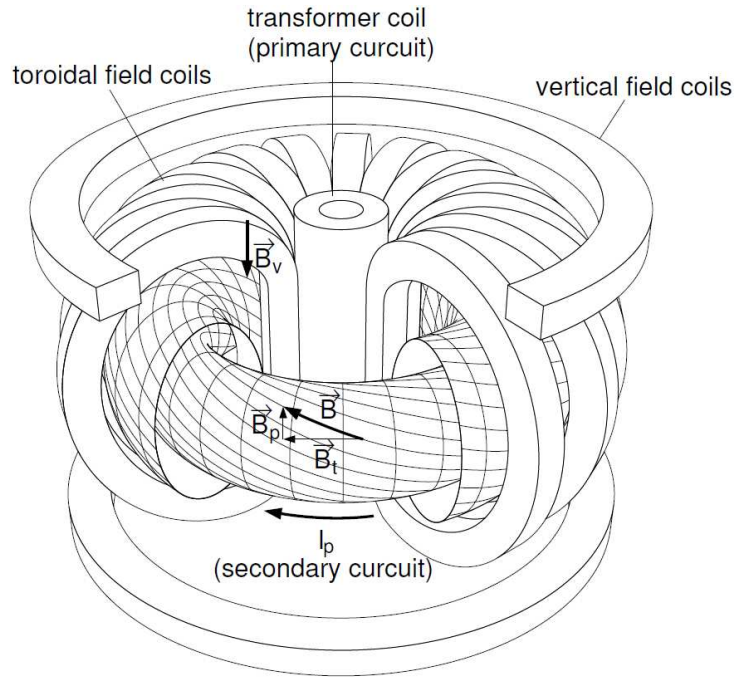


Figure 1.3: *Schematic view of a tokamak reactor showing the main coils needed for operation.*

respect to future power plants. A toroidal plasma calls for a helical configuration of the magnetic fields to reduce the drifts caused by the radial gradient of the toroidal magnetic field. The helicity of the field is achieved by two different designs, dividing the toroidal configurations into two sub-groups: "tokamak" and "stellarator". While the magnetic fields in the stellarator concept are all generated by coils located outside the plasma, the tokamak generates the poloidal component of its magnetic field by a plasma current and only the toroidal component is generated by external coils. The plasma current itself is induced by the transformer effect. The primary "coil", the so called solenoid, is located close to the axis of the torus, while the secondary coil is the plasma itself. Without additional effort, such a configuration can only be run in a pulsed mode due to the current ramp needed in the solenoid to drive the plasma current. Figure 1.3 shows a schematic view of the tokamak concept. Since the experimental implementation of the stellarator design is rather difficult, research has focused more on the tokamak concept. It is now so far advanced that plasma ignition is thought to be in reach. ITER is being built at the moment to achieve this ignition and study the physics of a self heated plasma.

1.2 Burn Condition and Impurities

To clarify the term "ignition" it is necessary to provide the definition of the gain factor:

$$Q = \frac{P_{fus}}{P_{ext}}. \quad (1.7)$$

with P_{fus} being the power generated from the fusion reactions and P_{ext} the power applied externally to heat the plasma. A plasma reaches ignition, when no external heating power has to be fed to the plasma ($P_{ext} = 0$), but the plasma heats itself by the production of energetic alpha particles. In this case $Q \rightarrow \infty$. Up to now most machines run H or D plasmas and their Q values are negligible.

From the few cases which experimented with D-T plasmas, JET tokamak has reached the highest value with $Q = 0.6$ [12].

The self sustaining heating process relies on the alpha particles produced in the fusion process. As equation 1.1 shows, the alpha particle carries 3.52 MeV. If it is assumed that this energy is fully released into the plasma and only thermalised alpha particles leave the plasma, then the burn condition can be deduced from a simple power balance:

$$P_\alpha = P_{rad} + P_{trans}. \quad (1.8)$$

in which the heating power density from the alpha particles, P_α balances the losses by radiation, P_{rad} , and heat transport, P_{trans} . It is useful to relate the various particle densities n_X to the electron density n_e via the concentration f_X of the particle species X , $n_X = f_X n_e$. The heating power density by alpha particles is then

$$P_\alpha = P_{fus}/5 = n_D n_T \langle \sigma_{DT} v \rangle E_\alpha = f_{DT}^2 n_e^2 \langle \sigma_{DT} v \rangle E_\alpha, \quad (1.9)$$

where f_{DT} is the concentration of the fuel ions of D or T (assuming $n_D = n_T$) and $\langle \sigma_{DT} v \rangle$ is the fusion reaction parameter. It is calculated as the average over a Maxwellian energy distribution and is only a function of ion temperature [13].

The radiated power density is the sum over radiative losses from Bremsstrahlung, line transitions and recombination radiation emitted from all plasma constituents. Each particle species contributes with a specific radiative power parameter L_X . Splitting up the total radiated power density into the contributions from fuel ions, alpha particles (He) and impurities one can write for the radiated power density:

$$P_{rad} = n_e^2 (2f_{DT} L_{DT} + f_{He} L_{He} + f_I L_I). \quad (1.10)$$

It should be noted that L_X is temperature dependent.

The power density for the loss mechanism by heat transport can be expressed by the plasma energy density W_{plasma} and the energy confinement time τ_E :

$$P_{trans} = \frac{W_{plasma}}{\tau_E} = \frac{3f_{tot} n_e k_B T}{2\tau_E}. \quad (1.11)$$

The quantity $f_{tot} = 2 - f_{He} - \langle Z \rangle f_I$ is the total particle fraction including electrons, fuel ions, alpha particles and impurity ions with average charge $\langle Z \rangle$. It can be derived from the quasi-neutrality of the plasma. By substituting equations 1.9, 1.10, 1.11 into equation 1.8 and reordering the terms the condition for ignition is obtained as function of the impurity concentrations:

$$n_e T \tau_E = \frac{3}{2} \frac{f_{tot} k_B T^2}{2f_{DT}^2 \langle \sigma v \rangle E_\alpha - (f_{DT} L_{DT} + f_{He} L_{He} + f_I L_I)} = f(T, f_{He}, f_I). \quad (1.12)$$

However, the fraction of He inside the plasma is not a free parameter, but the result of the rate at which it is produced and a rather complicated process (efflux from the plasma, recycling at the vessel walls and pumping efficiency) of He ash removal from the plasma. All processes involved in the He removal can be expressed in a global He ash confinement time $\tau_{He} = \rho \tau_E$ which is usually expressed as a fraction of the energy confinement time. In steady state conditions, the production rate equals the removal rate and this balance is expressed as:

$$f_{DT}^2 n_e^2 \langle \sigma v \rangle = \frac{n_{He}}{\tau_{He}} = \frac{n_e f_{He}}{\rho \tau_E}. \quad (1.13)$$

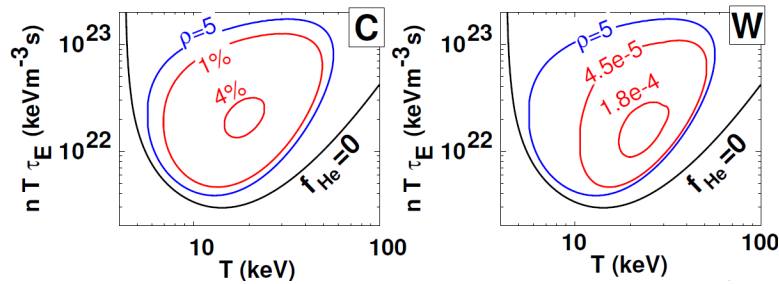


Figure 1.4: Operating window for a burning plasma under the influence of various He and impurity concentrations, taken from [11]

It is now possible to explore the parameter space (f_I, τ_{He}) with respect to the ignition condition, using equations 1.12 and 1.13. The result is shown in figure 1.4. First there is the black curve which represents the ideal case, in which the alpha particle transfers 100% of its energy to the plasma and is removed immediately after production, therefore neither diluting nor cooling the plasma. Then there is the more realistic case (blue line), representing the case where $\tau_{He} = 5\tau_E$. Already such a "clean" plasma exhibits a smaller region of ignition in the parameter space of triple product and temperature. Adding impurities besides the He ash, in this case carbon and tungsten, to the plasma restricts the operating window even more (red lines). The plot on the left shows calculations for carbon and the plot on the right for additional tungsten. While the light impurity carbon becomes fully ionized in the plasma and therefore radiates mainly bremsstrahlung, the tungsten ions are only partially ionised even in the core of the plasma and emit strong line radiation. This difference in radiative power also reflects in the acceptable amount of W in the plasma which is about two orders of magnitude smaller than for C. If the impurity concentration surpasses a certain level, the operating window closes fully, rendering ignition impossible. This makes impurity control for fusion plasmas a matter of high importance.

1.3 Thesis Motivation

As was shown in the previous section impurities impose a serious threat to achieving a burning plasma. The sources of impurities are the plasma facing components (PFC) installed in the vacuum vessel. Depending on the requirements the optimum material has to be chosen. For present day experimental reactors carbon fibre composites offer the best solution. However, carbon based PFC are not an option for ITER or a future power plant, due to its high erosion rate and high tritium retention. The solution envisaged for ITER is a wall that consists mainly of beryllium, a very light element, in combination with a tungsten divertor which can withstand the high energy fluxes in this part of the reactor. The divertor is a target plate onto which the plasma flowing outside the last closed flux surface is directed. Thus, the divertor plates encounter the highest energy loads of all PFCs. Even with a tungsten divertor, the erosion rates will be considerable. Nevertheless, only a small fraction of the eroded particles reach the main plasma from the divertor which is due to the large connection length between divertor and main plasma [14]. This makes the divertor a very important means to keep the plasma clean.

Tungsten being a rather heavy element ($Z = 74$) is a strong radiator in a fusion plasma, since, as

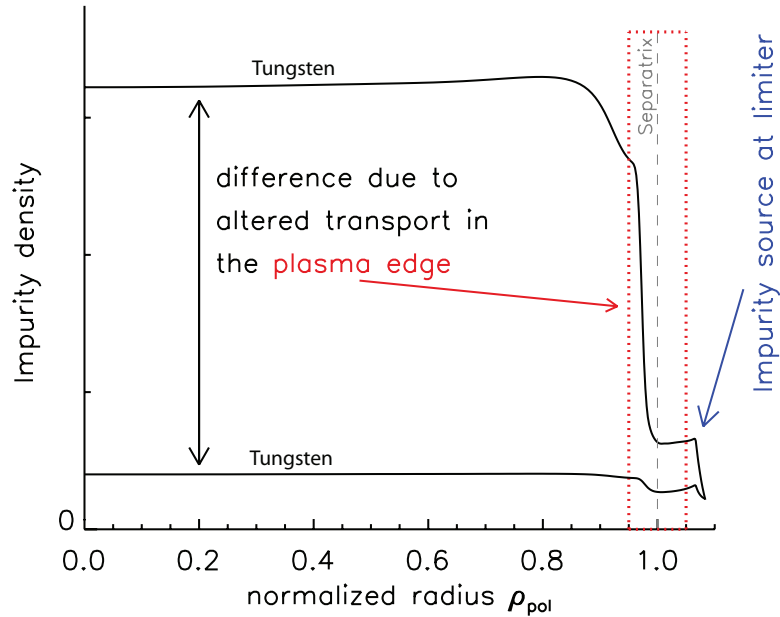


Figure 1.5: *Schematic plot of the importance of edge transport processes for the total impurity content in the core plasma*

mentioned, it will not be fully ionised. Therefore the concentrations have to be kept low. The low sputtering rate of tungsten is very helpful in this context. However, the erosion of tungsten can never be fully avoided, thus schemes have to be developed to control the concentration of tungsten in the plasma.

The ASDEX Upgrade (AUG) tokamak, being a device with a full tungsten wall offers optimum experimental conditions to investigate various tungsten control mechanisms. It has been shown, that strong central electron cyclotron heating reduces the central tungsten concentration, by increasing the diffusivity and possibly even creating an outward drift [15, 16]. However, before the tungsten reaches the core plasma it has to cross the edge plasma. The impurity transport parameters in this part of the plasma therefore determine the final concentration in the core plasma.

ITER, as well as future power plants, will be operated in the high confinement mode (H-mode). This operational mode is distinguished by a very narrow region (2 cm in AUG) right inside the last closed flux surface (LCFS, commonly called separatrix), with steep gradients in temperature as well as density. The steep gradients are caused by the so called edge transport barrier (ETB) in which turbulence is strongly suppressed and whose formation is still a matter of ongoing research. The high confinement of the H-mode refers to both, particles and energy. The steep gradients of the temperature and density profiles in the ETB lead to an upward shift of the whole profiles further inside the plasma, therefore affecting the full plasma volume. Investigations with charge exchange recombination spectroscopy (CXRS) have revealed, that for all observed impurities (He, C, Ne, Ar) the transport in the ETB is characterised by a strongly reduced diffusivity and a very high inward drift velocity [17]. It was deduced, that impurity transport in the ETB is neoclassical, imposing a strong inward drift for tungsten in this plasma region. This pinch would then cause a very high peaking factor between pedestal top and the concentration of tungsten right outside the LCFS.

Figure 1.5 shows schematically the drastic impact of the edge transport on the core plasma. This plot also introduces the coordinate system used throughout this thesis. The natural choice for the

radial axis in a tokamak is the normalized radius ρ_{pol} , which is defined as

$$\rho_{pol} = \sqrt{\frac{\Psi - \Psi_0}{\Psi_s - \Psi_0}}, \quad (1.14)$$

where Ψ is the poloidal magnetic flux at some position between the magnetic axis (index 0) and the separatrix (index s). This coordinate system has therefore its origin located at the magnetic axis and reaches the value 1 at the separatrix.

The two cases shown in figure 1.5 differ by their transport values in the ETB and the SOL. In the case with low tungsten content, the inward drift in the ETB was set to a low value, while the parallel losses in the SOL were chosen to be high. For the case with the high tungsten content, the transport settings were reversed. In the end, the transport parameters in this very narrow region of few centimeter width (in AUG) determine the impurity content in more than 90% of the plasma volume.

Connected with the H-mode are the edge localised modes (ELM) which cause periodic expulsions of plasma from the ETB region. The expulsions not only remove electrons and main ions from the plasma, but naturally also impurities. This effect has been observed for carbon in DIII-D by means of CXRS [18]. If it is assumed that the ELM event causes an increased diffusivity, ELMs would expell the impurities with a higher efficiency than the background ions, due to their higher peaking factor [17]. Therefore, following this diffusive ansatz, the frequency with which ELMs occur would have a strong impact on the impurity content of the main plasma. Experiments performed at AUG addressing this question seemed to confirm this hypothesis [14]. However, the experiments conducted in the framework of [14] did, by design, not allow for a separate assesement of radial and parallel transport phenomena. It is the scope of this work to achieve the disentanglement between the radial ELM-driven outflux of impurities and their parallel transport in the outermost layers of the plasma, the so called scrape off layer (SOL). A proper understanding of the influence of each of these two parameters on the core plasma impurity content is important, since only such an understanding allows to choose the correct means to control the impurities in future fusion devices.

This disentanglement is based on active plasma shaping, therefore the concept of triangularity will be explained briefly with the help of figure 1.6. The figure shows the influence of different triangularity values on the plasma shape. Higher upper triangularity means that the plasma is

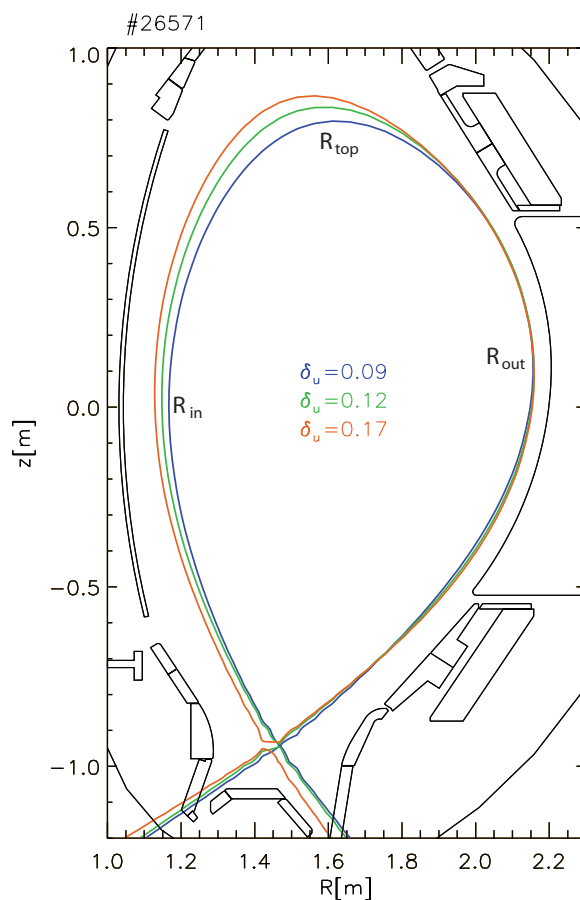


Figure 1.6: *Plasma shape (separatrix) for three different upper triangularity values. The plasma features important for the calculation of δ_u have been marked by R_{top} , R_{out} and R_{in} .*

more pointed at the top, while low upper triangularity leads to a more circular plasma. The upper triangularity is calculated by means of the following formula:

$$\delta_u = \frac{R_m - R_{top}}{a_m} \quad (1.15)$$

where $R_m = (R_{out} + R_{in})/2$ is the major radius and $a_m = (R_{out} - R_{in})/2$ is the minor radius of the plasma. R_{top} , R_{out} and R_{in} are the topmost, outmost and inmost radial positions of the separatrix. It is known that higher upper triangularity leads to higher particle confinement as well as lower ELM frequencies [19]. This makes δ_u the perfect tool for the investigations performed in this study.

1.3.1 Classical and Neoclassical Transport

In one of the previous paragraphs the terminus neoclassical transport was brought up. It is thought to be the dominating transport phenomena in the ETB [17] and will therefore be presented curtly in this section. However, the neoclassical transport is best introduced together with the classical transport. This section will give a brief overview of the cause and main equations of both transport mechanisms. A detailed derivation of the classical and neoclassical equations can be found in [20], [11] and references therein.

Both, classical and neoclassical transport, are based on the Coulomb interaction of charged particles in a magnetized plasma and are therefore collisional transport phenomena. The collisions between like particles do not give rise to particle transport, since the particles would only exchange positions. Therefore, only the collisions between unlike particles need to be accounted for. Thus, in a pure hydrogenic plasma the transport should be very low due to the very ineffective momentum exchange in electron-proton collisions. As soon as impurities are present, the ion-ion collisions become the driving mechanism for the collisional transport.

The classical transport is derived on a cylindrical geometry without anisotropy of the magnetic field, where the magnetic field is aligned parallel to the rotational symmetry axis of the cylinder. The motion of the particles is divided in parallel and perpendicular (to the magnetic field) components, where the latter one is in the radial direction. Calculating in this model the radial velocity $u_{\perp a}$ of particle species a with mass m_a and charge Z_a which arises from the collisions with particle species b with mass m_b and charge Z_b and multiplying $u_{\perp a}$ with the particle density of species a , n_a , one obtains the classical radial flux of species a :

$$\begin{aligned} \Gamma_{\perp a} &= n_a u_{\perp a} \\ &= -\nabla n_a \frac{m_a k_B T}{Z_a^2 B^2} \sum_{b \neq a} \nu_{ab} + \\ &\quad + n_a \frac{m_a k_B T}{Z_a^2 B^2} \sum_{b \neq a} \nu_{ab} \frac{Z_a}{Z_b} \left\{ \frac{\nabla n_b}{n_b} - \frac{\nabla T}{T} \left[\frac{3m_{ab}}{2m_b} - 1 - \frac{Z_b}{Z_a} \left(\frac{3m_{ab}}{2m_b} - 1 \right) \right] \right\} \end{aligned} \quad (1.16)$$

where $m_{ab} = m_a m_b / (m_a + m_b)$ is the reduced mass and ν_{ab} is the collision frequency of species a and b . One of the assumptions that flowed into this equation was that the temperature of the various particle species are equal, $T_a = T_b = T$. The terms of 1.16 can be reordered to a representation with a diffusive (terms proportional to ∇n_a) and a convective (terms proportional to n_a) part:

$$\Gamma_a = n u_a = -D \nabla n_a + v n_a \quad (1.17)$$

The classical diffusion coefficient for particle species a is then easily identified:

$$\begin{aligned} D_{CL}^a &= \frac{m_a k_B T}{Z_a^2 B^2} \sum_{b \neq a} \nu_{ab} = \frac{k_B T / m_a}{Z_a^2 B^2 / m_a^2} \sum_{b \neq a} \nu_{ab} \\ &= \frac{v_{Ta}^2 m_a^2}{2 Z_a^2 B^2} \sum_{b \neq a} \nu_{ab} = \frac{\rho_{La}^2}{2} \sum_{b \neq a} \nu_{ab} \end{aligned} \quad (1.18)$$

This resembles exactly the diffusion coefficient of a random walk process with a radial step length equal to the Larmor radius ρ_{La} and a stepping frequency ν_a which is given by the sum over the collision frequencies $\nu_a = \sum_{b \neq a} \nu_{ab}$. Even though it is not obvious at first sight, the classical diffusion coefficient is independent of Z_a since the collisional frequency is proportional to $\nu_{ab} \propto Z_a^2 Z_b^2$.

The further interpretation of the classical flux focuses on the convective terms which show a clear charge dependence. Therefore, the convective processes become increasingly important for highly charged heavy elements. The convective terms in 1.16 can be simplified for fully ionized ions where the relation $Z \approx m/2$ holds. This reduces the multiplier of the ∇T term to $1/2(1 - m_b/m_a)$ and the classical drift velocity writes under this approximation:

$$\vec{v}_{CL}^a = \frac{\rho_{La}^2}{2} \sum_{b \neq a} \nu_{ab} \frac{Z_a}{Z_b} \left\{ \frac{\nabla n_b}{n_b} - \frac{\nabla T}{T} \left[\frac{1}{2} \left(1 - \frac{m_b}{m_a} \right) \right] \right\} \quad (1.19)$$

Thus, the density profiles of the main ions and the other impurities lead always to convective fluxes of impurity species a which are directed towards the peak of those density profiles. The density peak is usually located in the center, which causes an inward flow of the impurity. The strongest effect of this pinch is expected in the ETB, where the density gradient is the steepest. The effect of the temperature driven convection is not so straightforward. For the case where light impurities interact with heavy impurities, *i.e.* $m_a < m_b$, the temperature gradient leads to an inward flux. However, this case is not so important, since the main contribution to \vec{v}_{CL}^a comes from the collisions of impurity ions with the background ions. For this case $m_a > m_b$ and the temperature gradient causes an outwards directed impurity flux, called temperature screening. This effect plays a major role in the central regions of the plasma as well as in the ETB, where the steepest temperature gradients in the plasma are found.

The classical transport equations were derived on a cylindrical geometry without magnetic anisotropy, therefore a local treatment of the particle interactions was suitable. However, the magnetic configuration of a tokamak is not cylindrical but toroidal and shows strong magnetic anisotropy (the toroidal field B_t varies along the major radius with approximately $1/R$). Particles travelling along the magnetic field lines of a tokamak will experience varying magnetic fields and curvatures. This necessitates the averaging of the particle motion over the magnetic flux surfaces. Figure 1.3 shows the geometric setup of such flux surfaces. It is assumed in this model that the density as well as the temperature are constant on the flux surfaces and the motion of the particle is described by its gyro-average (the center of mass when averaging over many gyrations around the magnetic field). This model delivers not only the neoclassical transport parameters, but also includes the classical impurity flows in a flux surface average.

The radial neoclassical fluxes arise eventually from the friction forces of the particles moving parallel to the flux surface. In this context it is important to introduce a quantity called collisionality, since it allows to distinguish between certain regimes of the neoclassical fluxes. It is defined as:

$$\nu_a^* = \frac{\nu_a}{\nu_B} \quad (1.20)$$

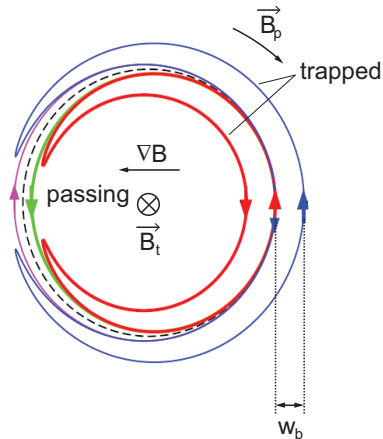


Figure 1.7: *Projections in the poloidal plane of passing and trapped particles in a tokamak plasma. The machine axis is on the left hand side, the magnetic axis is in the center of the figure. The width of a banana orbit is also depicted. Taken from [11]*

where $\nu_a = \sum_{b \neq a} \nu_{ab}$ is the collision frequency of particle species a with all other particle species and ν_B is the bounce frequency of a trapped particle. The trapping of charged particles occurs in anisotropic magnetic fields with zero electric field, if:

$$|v_{\parallel, \min}| \leq |v_{\perp, \min}| \sqrt{\frac{B_{\max} - B_{\min}}{B_{\min}}} \quad (1.21)$$

and is due to the conservation of the particle's energy as well as its magnetic dipole moment $\mu = mv_{\perp}^2/2B$. The minimum of the magnetic field in a tokamak is found on the outboard side of the plasma, therefore called Low Field Side (LFS), while the maximum is found on the inboard side which is called High Field Side (HFS). A particle for which condition 1.21 applies will not be able to execute a full circle around the magnetic axis, but will be reflected back when approaching the HFS of the plasma. In addition, the particle will also experience a ∇B drift and a drift caused by the circular toroidal motion which together cause the particle to switch between different magnetic flux surfaces. Thus, the particle will be moving on different flux surfaces when crossing the midplane depending on whether it is coming from or going to the HFS. This gives the poloidal projection of such a particle trajectory a distinct banana-shaped appearance as can be seen in figure 1.7.

Equation 1.21 can be expressed in terms of a geometrical relation for large aspect ratio tokamaks where the inverse of the aspect ratio $\epsilon = r/R \ll 1$, r being the minor radius of the plasma. For such machines the magnetic fields on the HFS and LFS can be approximated as $B_{HFS} \approx B_0/(1 - \epsilon)$ and $B_{LFS} \approx B_0/(1 + \epsilon)$ and condition 1.21 can be rewritten:

$$\left| \frac{v_{\parallel}}{v_{\perp}} \right|_{LFS} \leq \sqrt{\frac{B_{HFS} - B_{LFS}}{B_{LFS}}} \approx \sqrt{\frac{1 + \epsilon}{1 - \epsilon} - 1} \approx \sqrt{2\epsilon} \quad (1.22)$$

In the case of low collisionality where the trapped particles will be able to perform at least one bounce before colliding with another particle, these trapped particles play a dominating role in the neoclassical transport. Due to their banana-shaped orbits the transport these particles give rise to is called Banana regime. It usually also incorporates a plateau regime in which the transport does not change drastically with the collisionality and is therefore called the Plateau regime. The process behind this transport is based on the Coulomb collisions between trapped particles which move on

the same flux surface but in opposite poloidal directions. If these particles collide in such a way as to reverse their parallel velocities, the orbits will move radially by a distance w_b , which is the width of the banana orbit. The transport process can be interpreted as a random walk process with step width w_b , which is a much larger step width as compared to the Larmor radius governing the random walk process of the classical case. Additionally, the collision frequency at which such collisions occur is enhanced by a factor approximately $1/\epsilon$, since unlike in the classical case, no Coulomb scattering of roughly $\Delta\alpha \sim 90^\circ$ but only a change of pitch angle of about $\Delta\alpha \sim \sqrt{\epsilon}$ is needed. The collision frequency for the random walk in the Banana regime is therefore:

$$\nu_{a,eff} = \frac{\nu_a}{\Delta\alpha^2} \approx \frac{\nu_a}{\epsilon} \quad (1.23)$$

And the diffusion coefficient in the Banana-Plateau regime writes then:

$$D_{BP}^a = \frac{n_t}{n} \nu_{a,eff} w_b^2 \quad (1.24)$$

In large aspect ratio devices the estimation of the fraction of trapped particles yields $n_t/n \approx \sqrt{\epsilon}$. The banana width w_b can be expressed in terms of the toroidal Larmor radius also used in the classical diffusion coefficient and the so called "safety factor" $q \approx r/R \cdot B_t/B_p$ which is in the range of 4-5 at the separatrix in ASDEX Upgrade.

$$w_b \approx \frac{q}{\sqrt{\epsilon}} \rho_{La} \quad (1.25)$$

The Banana-Plateau diffusion coefficient can now be rewritten in terms of the classical one:

$$\begin{aligned} D_{BP}^a &\approx \frac{n_t}{n} \frac{\nu_a}{\epsilon} w_b^2 \\ &\approx \sqrt{\epsilon} \frac{\nu_a}{\epsilon} \left(\frac{q}{\sqrt{\epsilon}} \rho_{La} \right)^2 \\ &\approx \frac{q^2}{\epsilon^{3/2}} D_{CL} \end{aligned} \quad (1.26)$$

Hence, the diffusive impurity flux caused by this random walk process is easily one order of magnitude higher than in the classical case. However, if the collisionality increases beyond a certain point this process will quickly lose its importance, since the trapped particles will no longer be able to perform a full bounce before a collision takes place and the whole ansatz will no longer be valid due to the lack of the banana orbits.

In the case of high collisionality the so called Pfirsch-Schlüter regime will be dominating the neoclassical transport. Its driving mechanism are parallel flows which build up to even out an up/down density asymmetry which is driven by the diamagnetic fluid velocity which is within the fluid velocity but perpendicular to B. The parallel velocity of these flows is given by

$$\vec{u}_{\parallel a} = \frac{RB_t}{Z_a n_a} \frac{\partial p_a}{\partial \Psi} \left(\frac{1}{B} - \frac{B}{\langle B^2 \rangle} \right) \vec{e}_{\parallel} \quad (1.27)$$

where p_a is the pressure of particle species a . These parallel flows will cause a parallel friction force $\vec{F}_{\parallel a}$ which gives rise to the flux surface averaged diffusion coefficient:

$$D_{PS}^a \approx \left(\frac{dr}{d\Psi} \right)^2 (RB_t)^2 \left(\left\langle \frac{1}{B} \right\rangle - \frac{1}{\langle B^2 \rangle} \right) \frac{m_a k_B T}{Z_a^2} \sum_{a \neq b} \nu_{ab} \quad (1.28)$$

With some approximations suitable for large aspect ratio tokamaks it is possible to rewrite this diffusion coefficient in terms of the safety factor and the classical diffusion coefficient:

$$D_{PS}^a \approx 2q^2 D_{CL}^a \quad (1.29)$$

This transport mechanism is again, just as in the case of the Banana regime, much more efficient than the classical one.

The last contribution from the neoclassical transport phenomena is a convection which is directed radially inward. It arises when the toroidal electric field is considered in the case of low collisionality. The electric field leads to an acceleration of the trapped particles, but the canonical toroidal angular momentum of these particles is conserved. Thus, the turning points of the banana orbits lay on a surface with constant poloidal flux Ψ which moves inward with a radial velocity $v = E_t/B_p$.

This leads to a radial convective velocity, the so called Ware pinch, which can be written as:

$$v_{ware}^a = -k_{ware}(\nu_a^*) \frac{E_t}{B_p} \quad (1.30)$$

The factor $k_{ware}(\nu_a^*)$ depends on the collisionality and goes to zero for high collisionalities, since the particles can no longer travel on banana orbits but collide before completing a full orbit.

The introduction closes with a brief overview of this thesis' structure. Chapter 2 deals with the main diagnostic tools applied during the investigations undergone in the framework of this study. These tools are spectrometers for various spectral regions. If the data from the various spectrometers are combined, the tungsten ions can be followed from the erosion site at the wall up to the plasma center. A special focus is put on the SPRED spectrometer which provides new insights in the tungsten spectra in the vacuum ultraviolet (VUV) spectral region. Chapter 3 explains the means by which the tungsten radiation in the VUV region $\lambda = [10, 25]$ nm was evaluated. The evaluation aimed at differentiating the spectral features at electron temperatures (T_e) below 1 keV. This temperature range is of high importance, since it covers the ETB and the pedestal top. The results obtained from the evaluation of the spectra allowed for the first time for the observation of tungsten in this plasma region. Chapter 4 presents the experimental setup which used a modulated tungsten source as a method to probe the edge tungsten transport. The implementation of the source will be explained in detail, since it involves the use of the ICRH system in a new way. Furthermore calculations with a transport code will check the sensitivity of the probing method to detect changes of the radial transport in the ETB. The experimental results and their interpretation are finally laid out in chapter 5 and the conclusion and outlook can be found in chapter 6.

Chapter 2

Tungsten Diagnostics

For the observation of tungsten in AUG a set of spectrometers for visible as well as vacuum ultraviolet (VUV) light are available. All tungsten measurements rely on passive spectroscopy. This chapter will present the diagnostic tools required for the observation of tungsten at the various positions in a tokamak and give the physical background, that is needed to interpret the spectroscopical data.

2.1 Tungsten Erosion measurements

2.1.1 SXB Method and Corona Model

The tungsten erosion flux is determined from the line radiation of neutral tungsten at $\lambda_{vis} = 400.875 \text{ nm}$ ($5d^56s^7S_3 - 5d^56p^7P_4$). This transition has been studied extensively in this context([21] and references therein). The relation between the line intensity and the erosion flux is linked via the inverse photon efficiency S/XB . The advantage of this method is, that it provides erosion fluxes without the need for detailed knowledge of the electron density in the emitting region. The level of sophistication that flows into the determination of the S/XB value depends on the electron density range for which it is determined. At low densities the corona ionisation approximation can be applied, while at higher densities the use of a collisional radiative model is necessary. Here we discuss the easiest case, where collisional deexcitation can be neglected, *i.e.* the pure corona approximation. Furthermore, the recombination is also considered negligible.

In the corona approximation the dominant excitation process into state σ is by electron collision,

$$\dot{n}_\sigma = X_{\rho \rightarrow \sigma} \cdot n_\rho \cdot n_e \quad (2.1)$$

and the only balancing deexcitation process is spontaneous emission,

$$\dot{n}_\sigma = - \sum_{\kappa < \sigma} A_{\sigma \rightarrow \kappa} \cdot n_\sigma, \quad (2.2)$$

with n_ρ the density of ions in the ground state ρ , n_σ the density of those ions in excited state σ , $X_{\rho \rightarrow \sigma}$ the excitation rate coefficient (electron temperature dependent), $A_{\sigma \rightarrow \kappa}$ the Einstein coefficient for spontaneous decay from state σ into κ and n_e the electron density. A plasma that is governed mainly by the above two processes must have a low electron density ($< 10^{19} \text{ m}^{-3}$). Only then can the spontaneous decay of the excited state be more frequent than electron atom collisions. This leads to the result that most atoms or ions are in the ground state configuration and electron atom

collisions have only the effect of an excitation of the atom from the ground state or an ionization. Further, the emission rate density of photons of a certain transition $\sigma \rightarrow \delta$ is given as

$$\epsilon_{\sigma \rightarrow \delta} = A_{\sigma \rightarrow \delta} \cdot n_{\sigma}, \quad (2.3)$$

which can be rewritten with equations 2.1, 2.2 and gives

$$\epsilon_{\sigma \rightarrow \delta} = n_e n_{\rho} X_{\rho \rightarrow \sigma} \cdot \frac{A_{\sigma \rightarrow \delta}}{\sum_{\kappa < \sigma} A_{\sigma \rightarrow \kappa}}. \quad (2.4)$$

The fraction $A_{\sigma \rightarrow \delta} / \sum_{\kappa < \sigma} A_{\sigma \rightarrow \kappa}$ is the so called branching ratio $B_{\sigma \rightarrow \delta}$ of transition $\sigma \rightarrow \delta$. Since $\epsilon_{\sigma \rightarrow \delta}$ contains the excitation rate coefficient $X_{\rho \rightarrow \sigma}(T_e)$ it is itself an electron temperature dependent quantity. The plasma conditions at the first wall with the rather low electron densities justify the use of the corona approximation in most cases. Integrating the emission rate along the LOS of the spectrometer one obtains the photon flux

$$\Gamma_{ph, \sigma \rightarrow \delta} = \int_0^R \epsilon_{\sigma \rightarrow \delta}(l) dl. \quad (2.5)$$

To connect the photon flux with an erosion flux this work follows the derivation of the S/XB method as presented in [22] and [23]. The time evolution of the density of an impurity ion $n_Z(x, t)$ of charge Z at position x is governed by transport, ionisation and recombination. All these effects are combined in a 1-dimensional transport equation:

$$\frac{\partial n_Z}{\partial t} = -\frac{d}{dx} \Gamma_Z - S_Z n_e n_Z - \alpha_Z n_e n_Z + S_{Z-1} n_e n_{Z-1} + \alpha_{Z+1} n_e n_{Z+1} - \frac{n_Z}{\tau_{\parallel}}, \quad (2.6)$$

where Γ_Z is the flux of ions of charge Z , S_Z is the collisional ionisation rate coefficient and α_Z is the recombination rate coefficient. Parallel transport, important to limiter sources, is represented by the expression n_Z / τ_{\parallel} . Under the assumption of equilibration ($\partial n_Z / \partial t = 0$) an integration of equation 2.6 along the line of sight gives:

$$\Gamma_Z(R) - \Gamma_Z(0) = \int_0^R -S_Z n_e n_Z + S_{Z-1} n_e n_{Z-1} - \frac{n_Z}{\tau_{\parallel}} dx. \quad (2.7)$$

The recombination terms have been skipped in the previous equation. Under the plasma conditions in the plasma edge ($n_e \approx 1e19 \text{ m}^{-3}$, $T_e \approx 20 \text{ eV}$) the recombination from W^{20+} down to neutral tungsten was calculated to take about $\tau_{rec} \approx 80 \text{ ms}$, while the parallel and perpendicular loss time ($\tau_{\perp} = \Delta x^2 / D_{\perp}$, with $\Delta x = 5 \text{ cm}$, $D_{\perp} = 1 \text{ m}^2/\text{s} \rightarrow \tau_{\perp} = 2.5 \text{ ms}$) is on the order of few milliseconds. The omission of recombination is therefore justified. The summation over the ionisation stages $i < Z$ results in an equation that relates the neutral erosion flux with higher ionisation stages. It also leads to the cancellation of the ionisation terms of neighbouring ionisation stages since the loss of stage i is the gain of stage $i + 1$. The only term that is left in the integral of equation 2.7 is the one connecting stage Z with the next higher ionisation stage and of course the parallel loss term. The summation can then be written:

$$\sum_{i=1}^Z \Gamma_i(0) - \sum_{i=0}^Z \Gamma_i(R) = \int_0^R S_Z n_e n_Z + \sum_{i=1}^Z \frac{n_i}{\tau_{\parallel}} dx. \quad (2.8)$$

The integration along the line of sight is at the same time an integration along a temperature profile. If the maximum ionisation stage Z is chosen small enough, *e.g.* $Z = 4$, then the density of the ionisation stages $i \leq Z$ at a position R inside the main plasma $n_{i \leq Z}(R) = 0$. With a zero

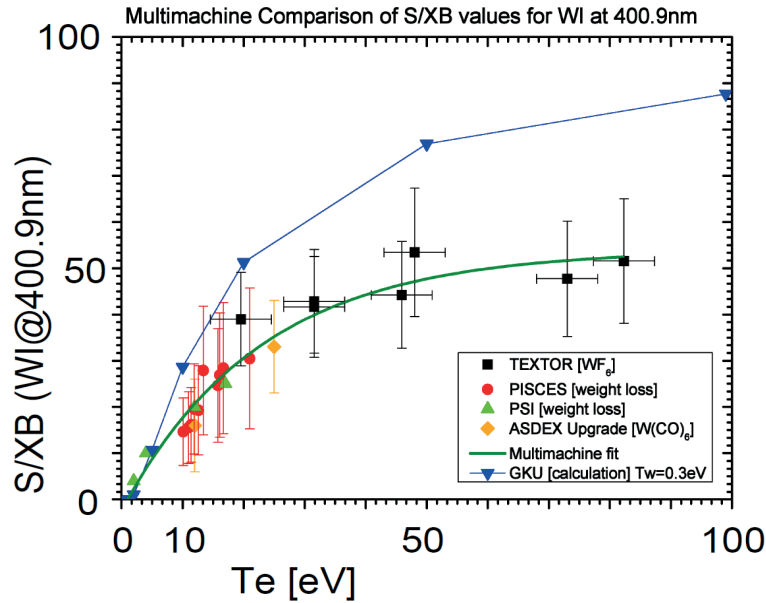


Figure 2.1: *Experimental S/XB data for neutral tungsten at $\lambda_{vis} = 400.875$ nm and theoretical predictions for different tungsten temperatures; taken from reference [24]*

ion density also the flux of the ions at a position R inside the main plasma $\Gamma_{i < Z}(R) = 0$. For such low ionisation stages the losses to the total inward impurity flux due to parallel transport can be neglected and $\int_0^R \sum_{i=0}^Z \frac{n_i}{\tau_{\parallel}} dx = 0$. Under the assumption that no sputtered ion is produced in an ionisation stage higher than Z , the total impurity influx Γ_Z is then given by the symplified equation 2.8:

$$\Gamma_Z = \sum_{i=0}^Z \Gamma_i(0) = \int_0^R S_Z n_e n_Z dx. \quad (2.9)$$

Γ_Z is a function of the line integrated ionisation rate of the highest ionisation stage considered. Dividing Γ_Z by $\Gamma_{ph, \sigma \rightarrow \delta}$, the line integrated photon flux of transition $\sigma \rightarrow \delta$, gives:

$$\frac{\Gamma_Z}{\Gamma_{ph, \sigma \rightarrow \delta}} = \frac{\int_0^R S_Z n_e n_Z dx}{B_{\sigma \rightarrow \delta} \cdot \int_0^R n_e n_{Z, \rho} X_{\rho \rightarrow \sigma} dx}. \quad (2.10)$$

With the corona approximation it is valid to assume that all impurity ions at ionisation stage Z are in the ground state, $n_{Z, \rho} = n_Z$. For the next step it should be recalled that the light used for this method is in the visible range. This means that the transition occurs between the upper energy levels, close to the ionisation energy. With the atom or ion being mostly in the ground state an excitation into one of the upper levels needs almost as much energy as the ionisation.

Since the energy needed for an ionisation or excitation is almost the same, the temperature dependence of $X_{\rho \rightarrow \sigma}$ and S_Z can be assumed to be similar in a small temperature range. This approximation is valid since the temperature range in which the individual ionisation stages exist is rather narrow for the low ionisation stages of tungsten. The electron temperature needed to excite the atom into the high energy levels sets the lower boundary for neutral tungsten. If now each ionisation stage exists only on an interval $x_Z = [x_{Z,0} - \delta x, x_{Z,0} + \delta x]$ the ionisation rate coefficient and the excitation rate coefficient can be approximated on that interval by:

$$S_Z(x) = S_{Z,0} \cdot f(x) \quad \text{and} \quad X_{\rho \rightarrow \sigma}(x) = X_{\rho \rightarrow \sigma,0} \cdot f(x). \quad (2.11)$$

With this expansion of S and X equation 2.10 can be rewritten as:

$$\frac{\Gamma_Z}{\Gamma_{ph,\sigma\rightarrow\delta}} = \frac{S_{z,0} \cdot \int_0^R f(x)n_e n_Z dx}{X_{\rho\rightarrow\sigma,0} B_{\sigma\rightarrow\delta} \cdot \int_0^R f(x)n_e n_Z dx}. \quad (2.12)$$

This gives the desired link between the measured photon flux and the ion flux, without the need for detailed knowledge of the electron density. Photon and ion flux are connected by the proportionality factor S/XB which can be interpreted as ionisations per emitted photon:

$$\Gamma_Z = \frac{S_{z,0}}{X_{\rho\rightarrow\sigma,0} B_{\sigma\rightarrow\delta}} \cdot \Gamma_{ph,\sigma\rightarrow\delta}. \quad (2.13)$$

The factor S/XB has to be determined separately for each temperature range and each transition. The transition of interest for tungsten is, as mentioned above, at $\lambda_{vis} = 400.875$ nm and is emitted by neutral tungsten. In [21] the experimental findings and theoretical predictions have been compared and the result is shown in figure 2.1 The experimental results show a very flat behaviour of S/XB for temperatures above 10 eV. Measurements of the electron temperature in the AUG divertor usually deliver temperatures in this range. The flatness of the S/XB profile beyond 7 eV allows for the determination of the neutral tungsten erosion flux without having to know the exact electron temperature at the erosion site. Furthermore the method delivers well localized measurements for the tungsten erosion since the ionisation length for tungsten is 0.1 – 0.2 mm in the SOL of AUG [14]. This makes this method a very powerful tool for the investigation of the local tungsten sources in AUG.

2.1.2 Visible Light Spectrometer System

A set of spectrometers for visible light is available at AUG for the measurement of tungsten erosion fluxes. Each spectrometer can be used to analyse the light from multiple lines of sight (LOS). The individual LOS are defined by the geometry of the optical heads mounted inside the vacuum vessel. An optical head holds several optical fibers which are connected to an optical switchboard in vicinity of the spectrometer. Each fiber then corresponds to one LOS. The spectrometer on its side is equipped with up to 18 optical fibers which can be connected on the switchboard to the fibers coming from the torus. The setup including an optical switchboard gives the freedom to choose the combination of LOS best suited for the individual experiment.

The spectrometer has a grating with 2400 grooves per millimeter. The setup is optimized to obtain spectra from the -1 grating order with a moderate spectral resolution of $\Delta\lambda/\lambda = 4.6 \cdot 10^{-4}$ at $\lambda = 470$ nm. It comprises two identical camera lenses (Leica, Apo Elmarit-R) with focal length 180 mm and f number of 2.8. A slit with adjustable width is positioned between the optical fiber heads and the first lens allowing to control the intensity of the collected light. The first lens is focused on the entrance slit, creating parallel light that impinges on the spectrometer grid. The light diffracted into the -1 order is then collected by the second lens, whose focal plane is located on the camera. With this setup the light from the slit is imaged on the CCD-camera. Its main advantages are a good image quality with almost no astigmatism and a large focal plane ($\sim 30 \times 30$ mm) which allows for the previously mentioned simultaneous measurement of many (ideally up to 50) LOS. The sensitivity of the complete system starting from the optical fibers in the vacuum vessel is determined experimentally. For the sensitivity determination an integrating sphere is used for which the spectral radiance is known. The wavelength dependence of the sensitivity shows a broad

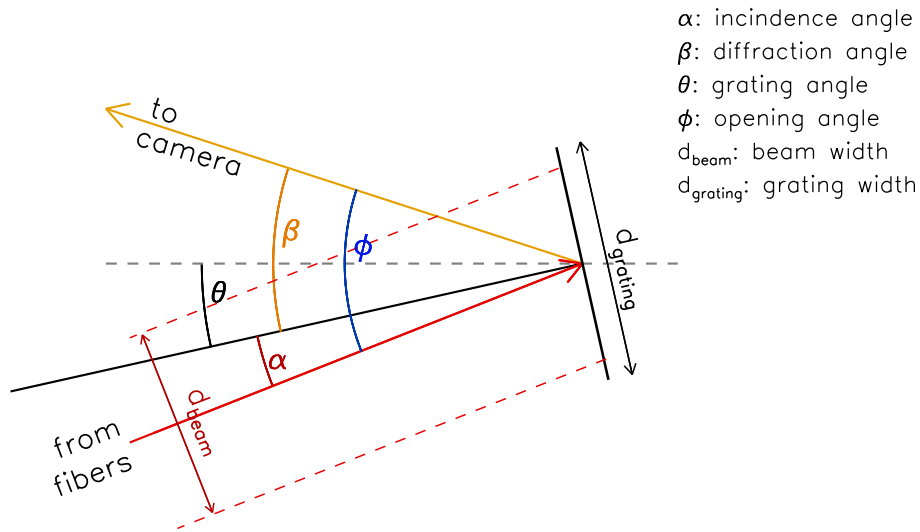


Figure 2.2: Schematic view of the angles involved in the diffraction. The angle θ is controlled via a sine drive.

maximum at about 550 nm. Towards shorter wavelengths down to 370 nm it drops by more than one order of magnitude, but exhibits a slower decay towards longer wavelengths. The lower boundary of the overall detectable wavelength interval is set by the decrease of sensitivity, while the long wavelength limit is set by the diffraction mechanism and the dimensions of light beam and grating.

In this context it is of importance to mention that the orientation of the grating is controlled via a sine drive. This is necessary since for one orientation of the grating only a wavelength interval of ≈ 13 nm width is observable. To derive the maximum wavelength detectable with this system one has to start from the grating equation:

$$n \cdot g \cdot \lambda = \sin\alpha + \sin\beta, \quad (2.14)$$

with n the grating order, g the groove density, λ the wavelength of the light, α and β the angles of the light ray with grating normal. Introducing the angle of the grating with the axis of symmetry θ and the opening angle of the spectrometer $\phi = \alpha + \beta$ the angles α and β can be rewritten as:

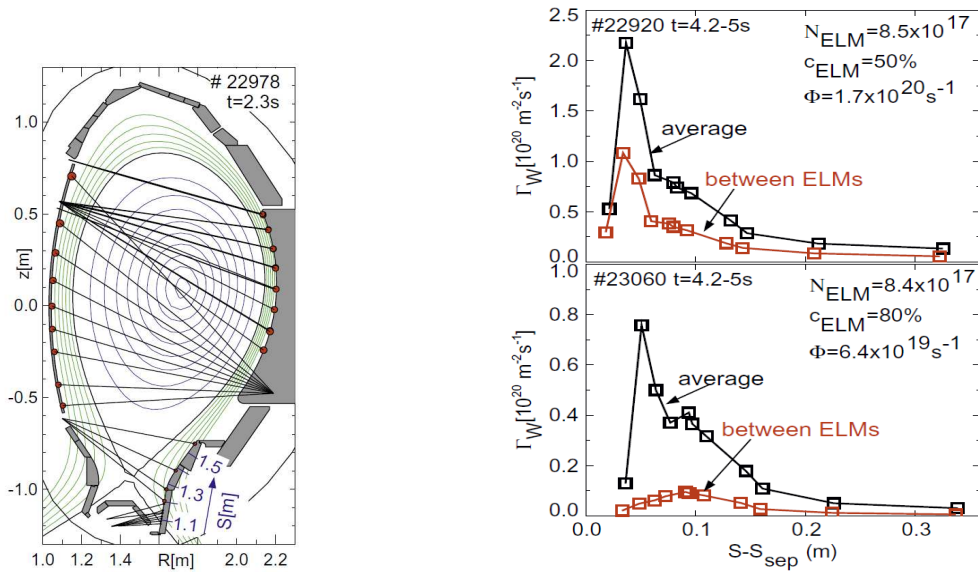
$$\alpha = \phi/2 - \theta, \quad \beta = \phi/2 + \theta. \quad (2.15)$$

Using these definitions, the grating equation becomes a function of the opening angle and the adjustable turning angle:

$$n \cdot g \cdot \lambda = \cos(\phi/2) \cdot \sin\theta, \quad (2.16)$$

In order to find the longest detectable wavelength the turning angle of the grating θ has to be maximized. The absolute limit is reached, when either the incident or the diffracted light ray is parallel with the grating surface, *i.e.* α or $\beta = \pi/2$. A more stringent limit is set by the size of the light beam and the grating dimensions:

$$\cos\alpha, \cos\beta \leq \frac{d_{\text{beam}}}{d_{\text{grating}}}, \quad (2.17)$$



(a) Various LOS used for tungsten erosion measurements in AUG. The flux surfaces are shown for #22978 at 2.3s. The red dots indicate the site of measurement.

(b) Profiles of tungsten influx in the outboard divertor. Inter-ELM divertor temperature close to separatrix for #22920 is 20 eV and 6 eV for #23060.

Figure 2.3: Examples for tungsten erosion measurements in AUG. Taken from reference [14].

where d_{beam} and d_{grating} are the width of the light beam and the grating. With this limitation for α and β one can use equation 2.15 to calculate θ_{max} :

$$\theta_{\text{max}} = \pm \left(\arccos \left[\frac{d_{\text{beam}}}{d_{\text{grating}}} \right] + \frac{\phi}{2} \right) \quad (2.18)$$

The width of the beam is calculated from the focal length and the f number $d_{\text{beam}} = 180 \text{ mm} / 2.8$. The grating has a width of 100 mm, the opening angle $\phi = 30^\circ$ (given by the position of the two lenses) and the grating density is $g = 2400 \text{ L/mm}$. With these settings the maximum observable wavelength is $\lambda_{\text{max}} = 778.7 \text{ nm}$.

The spectra created with this setup are recorded with CCD-cameras. The cameras can be used in two modes. In the first mode the camera records the spectra from several (usually up to 17) LOS simultaneously. This leads, however, to a rather low temporal resolution which is 3 – 4 ms. This mode is usually used when the spatial information on the erosion profile is of interest. The second mode uses only one LOS or a binning (summation) of the spectra of several LOS which means a limitation to the spatial information on the erosion profile. The gain is on the temporal resolution. The camera, run in this mode, frames each spectra in less than $300 \mu\text{s}$ and is fast enough to even resolve the effects of ELMs on the erosion clearly [14]. The efficiency of this diagnostic in terms of a global tungsten erosion flux measurement relies strongly on the availability of a suitable set of LOS. At the moment several dozens of LOS are installed in AUG, covering the lower outboard divertor, the low field side (LFS) limiters at the ion cyclotron resonance heating (ICRH) antennae and the inner heat shield. Figure 2.3a shows a typical setup for the global measurement of the tungsten erosion.

This diagnostic has been used successfully in many experiments and has provided valuable insight in the processes guiding the tungsten erosion [14, 25–27]. At this point only one result should be presented curtly to give an idea of the performance of the system. This result is taken from [14]

and sheds light on the erosion processes in the divertor in ELMy H-Mode plasmas. With the setup as shown in figure 2.3a the erosion flux was measured on the outboard side of the lower divertor. Not only the spatial distribution of the erosion flux, but also the temporal behaviour was part of the investigation. The quantity $S - S_{Sep}$ (see figure 2.3a) gives the distance along the divertor with respect to the position where the separatrix impinges on the divertor tiles. Since the spatial profile was of interest in these experiments the time resolution was rather low, but still high enough to distinguish between ELMs and inter-ELM phases. The main results of this particular investigation were that ELMs contribute up to 80% of the total erosion flux in the divertor and inter-ELM erosion behaviour is affected by changes in electron temperature. Figure 2.3b shows the effects described above.

The only weak point of this diagnostic is its inability to determine the fraction of tungsten that is redeposited on the tile immediately after the erosion. This process called prompt redeposition is a result of the small ionisation length of neutral tungsten (0.1 – 0.2 mm) and the relatively large ion gyro radius which is ≈ 2 mm at 2.5 T. If the neutrals get ionized at a distance from the wall that is smaller than one gyro radius they impinge on the wall and reattach to it with a certain probability. According to reference [14] this happens theoretically to 90% of the eroded particles.

2.2 Tungsten Radiation from the Plasma Edge and Core Plasma

Tungsten is a powerful radiator in the spectral range of the vacuum ultra violet (VUV) and soft X-ray spectral range [28]. As soon as it enters the plasma region enclosed by the separatrix it radiates mainly in these short wavelengths. For the observation of tungsten radiation, this fact necessitates a very different spectrometer type as compared to the erosion measurement with visible spectroscopy. The main difference is, that the light in the VUV and soft X-ray can not penetrate through optical fibers, lenses or windows. It is therefore not possible to transfer the light to a spectrometer located far away from the vacuum vessel. Since the light is also attenuated strongly by air, the spectrometers themselves have to be kept in vacuum. The solution is to position the spectrometer at the end of a long duct, from where it looks directly into the plasma. The only optical instruments that can be used in such a setup are slits, mirrors and collimators. The spectrometer systems installed at AUG do not use mirrors, but imaging gratings which perform the dispersion as well as the imaging of the entrance slit onto the detector. This already limits the number of available lines of sights to usually one per spectrometer.

2.2.1 VUV-spectrometer SPRED

For the investigation of tungsten transport in the plasma edge the VUV spectral range is of special importance. The specific wavelength interval is $\lambda_{VUV} = [10, 25]$ nm. In this wavelength range tungsten radiation from the ETB and pedestal top has been identified, as will be shown in chapter 3. The spectrometer installed at AUG capable of monitoring this spectral range is the 'survey, poor resolution, extended domain' (SPRED) spectrometer. It is equipped with an aberration-corrected grating with a groove density $g = 2105$ L/mm manufactured by Jobin Yvon ([29] and references therein). The main characteristic of this type of grating is its virtually astigmatism-free image. The advantage of an astigmatism free image is an increased intensity of the diffracted light in the

Element	W^{44+}	O^{3+}	O^{5+}	O^{4+}	Cu^{17+}	N^{4+}	Cu^{17+}	Cu^{16+}	Cu^{18+}
λ [nm]	13.29	15.01	17.30	19.28	19.64	20.41	20.93	21.88	22.14
Element	Cu^{17+}	N^{3+}	N^{3+}	Cu^{18+}	N^{3+}	He^{1+}	C^{3+}	N^{3+}	
λ [nm]	23.42	24.72	26.63	27.337	28.35	30.38	31.24	32.27	

Table 2.1: List of elements and wavelengths used for the wavelength calibration.

meridional cut of the focal plane (plane of diffraction) [30]. The grooves of the grating are etched on a toroidal substrate to achieve the minimisation of the astigmatism. Furthermore, the grooves are not equidistant and straight, but have a varying curvature and distance as to create a 40 mm wide flat focal field. The toroidal substrate has a radius of 919 mm in the plane of dispersion and a radius of 102.5 mm in the plane perpendicular to it. The optimum incidence angle is 71.9° for this type of grating.

However, the grating installed in the SPRED spectrometer at AUG exhibits a slightly different incidence angle (68.3°). This is due to an in situ manual readjustment. The readjustment became necessary since the screw locking the grating in place had become loose and consequently the grating had moved by the vibrations during tokamak operation. The misaligned grating produced spectra that were strongly out of focus and therefore unsuitable for evaluation. After the realignment an equally good focusing of the transition lines was achieved over the whole observed spectral range. This and the following paragraphs present the calibrations and evaluations of the spectra recorded with the new geometrical setup of the spectrometer.

The wavelength calibration and the determination of the dispersion needed essentially two informations: wavelength and pixel number of an observed transition. Obtaining these two informations was, however, a rather complicated undertaking. First, the starting point was a spectrum, where only the position of the He^+ line at $\lambda = 30.38$ nm was known from special He-glow discharges inside the spectrometer duct. Second, the dispersion is by design not constant over the spectral range. It differs by more than 10% for the lower and the upper range of the observed spectral range. Therefore, the identification of other lines in the rest of the observed spectrum had to start from the upper end of the accessible wavelength range. Injecting impurities into the plasma significantly helped the identification process. The impurity injection was achieved either by gas puffing (N_2) or by laser ablation (Cu). Besides these impurities also intrinsic impurities like carbon, oxygen and, of course, tungsten were used for the wavelength calibration. All identified elements and their transition wavelengths used in the calibration process are listed in table 2.1.

The resulting wavelength calibration and dispersion relation are plotted in figure 2.5a. The aforementioned non-constant dispersion shows very well in the experimental data. The increased scatter of the dispersion at the edges of the range where experimental data is available is caused by

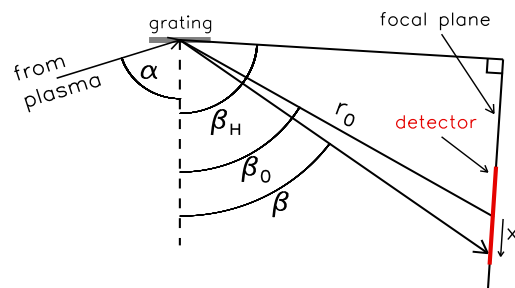


Figure 2.4: Schematic drawing of the angles and distances involved in the diffraction at the SPRED spectrometer

the method to calculate the dispersion. It takes into account the wavelengths and pixel values of all neighbouring spectral lines.

In addition to the experimental values in the top plot of figure 2.5a two fits are also drawn into that plot. The models corresponding to the fits are on the one hand an analytical model of the SPRED wavelength dependence and on the other hand a simple fourth order polynomial. The analytical model is based on first principles, but the calculations are rather lengthy and will therefore only be sketched here. The aim is to derive a relation between the pixel number (spatial coordinate 'x' on the detector) and the wavelength diffracted onto that pixel. Starting from the grating equation 2.14 the spectrum has to be projected on to the flat field focal plane in order to obtain $\lambda(x)$. This introduces three more parameters in the equation:

- r_0 , the distance from grating to the center of the detector
- β_0 , the angle between grating normal and line to the center of the detector
- β_H , the angle defining the orientation of the focal plane

Figure 2.4 shows a schematic drawing of the angles and distances involved in the diffraction and detection process. After some calculations the desired dependence of λ on the position on the detector, x , writes as:

$$\lambda(x) = \frac{1}{gk} \cdot \left(\sin\alpha - \sin \left[\beta_0 + \arctan \left(\frac{x \cdot \cos(\beta_H - \beta_0)}{r_0 - x \cdot \sin(\beta_H - \beta_0)} \right) \right] \right), \quad (2.19)$$

with g being the groove density and k the diffraction order, -1, for the SPRED spectrometer.

Both models reproduce the experimental data very well (see residuals in figure 2.5a), but only the fit with the analytical model provides additional information on the geometric setup of the spectrometer. One important finding from the analytical model was already presented above. It is the incidence angle of the readjusted grating. The other parameters presented in 2.19 have also been determined with this method and they all differ slightly from the original design values. However, the difference is on the order of 2 – 3% for most parameters and the strongest deviation from the design was found for the angle between grating normal and center of the focal plane which differs by 4.8%. The realignment of the grating extended the accessible spectral range from the design value $\lambda_{design} = [9.5, 32]$ nm to $\lambda_{exp} = [8.5, 32.5]$ nm, at a cost of a slightly increased dispersion. As mentioned above, the dispersion $d\lambda(x)/dx$ is also calculated for both models and drawn in the lower plot of figure 2.5a. It is obvious that the trends are very different for the two models. The dispersion obtained from the polynomial model resembles the experimental data somewhat better, but the difference to the analytical model is marginal in the regions where experimental data is available.

After the successful calibration of the wavelength, the next important step in the calibration process is the determination of the line width and shape generated by the spectrometer. One impediment to this task are the large number of lines present in the spectrum of the SPRED spectrometer. These lines often blend and distort the line shape. This makes it difficult to find single lines that can be evaluated with respect to line width and line shape, without the disturbing influence of closely neighbouring lines. From the relatively long list of transitions presented in table 2.1 only few are suited for the determination of the line properties.

The line shape produced by this type of spectrometer is a convolution of a Gaussian and a

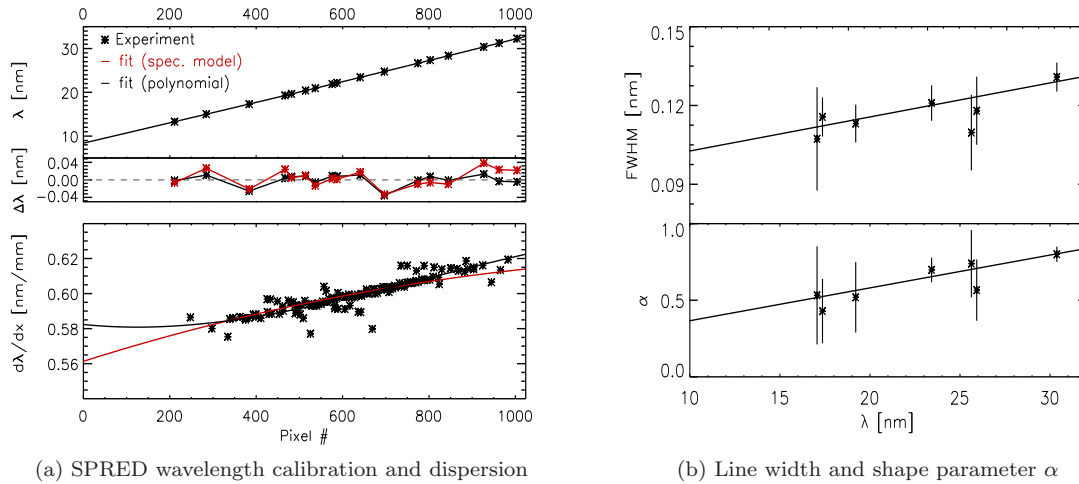


Figure 2.5: *Specifications of the SPRED-spectrometer. Figure a), top shows the wavelength versus pixel number. An analytical model (in red) and a fourth order polynomial (in black) were used to fit the dependence. The residuals $\Delta\lambda$ of the analytical model and the polynomial are plotted in the box below. Figure a), bottom shows the dispersion as obtained from the experimental data and the models. In figure b) the line width (top) and the line shape parameter (bottom) are displayed as function of wavelength.*

Lorentz profile [31]. A suitable representation of this variable profile is given by:

$$F(p) = \frac{1}{\left(1 + (2\alpha^2 - 1) \left(\frac{p-p_0}{\Delta p_{1/2}}\right)^2\right)^{1/\alpha^2}}, \quad (2.20)$$

where α is the parameter that determines whether the profile is more Gaussian ($\alpha \rightarrow 0$) or resembles a Lorentzian ($\alpha = 1$). The independent variable p is the pixel number, while the central position of the profile is given by p_0 and its FWHM in pixel by $\Delta p_{1/2}$. This function is fitted to the selected lines with width and shape parameter as fitting parameters. The fit then provides the desired values for width and shape parameter. With the rather sparse data figure 2.5b still gives an overview of the trends of these two values. The shape is more of the Lorentzian type but becomes more Gaussian for lower wavelengths. The linewidth allows for a spectral resolution of about 0.1 nm and has a trend to lower values at lower wavelengths.

2.2.2 Absolute Intensity Calibration of SPRED spectrometer

Unlike for the visible and near ultraviolet, where the well known blackbody radiation allows to construct an intensity-calibrated light source, there are no calibrated light sources available for the VUV spectral range. One exception is synchrotron radiation from accelerator storage rings. However, using such a light source for an absolute intensity calibration involves a high experimental effort which is not proportionate for the foreseen application of the presented spectrometer. Therefore, the branching ratio method, first mentioned in [32], was successfully applied to obtain an absolute intensity calibration.

The method allows for the calibration to be carried out in situ which significantly reduces the experimental requirements. It relies on the measurement of two transition lines, one in the VUV range of interest, the other in the visible region, while both lines originate from the same excited

level (see figure 2.6). In this case the excitation rate for both transitions is exactly the same and can be cancelled out in equation 2.22. Furthermore, the light source has to be optically thin for both observed lines which is the case for the plasmas produced in AUG tokamak. It is self-evident, that the light from both transitions has to be observed along the same LOS for this approach to lead to correct results.

If all prerequisites are fulfilled the radiative line intensities read:

$$I_s = \int_{LOS} N_e(r) A_s h\nu_s dr = \frac{1}{k} \cdot I_s^{cts} , \quad I_l = \int_{LOS} N_e(r) A_l h\nu_l dr , \quad (2.21)$$

with A_s and A_l the transition probabilities for spontaneous emission from excited state e to state v and u , $h\nu_s$ and $h\nu_l$ are the energies per photon for the short, index s and long, index l wavelength transition, while k is the desired sensitivity connecting the intensity from the VUV given as count rate I_s^{cts} to physical dimensions. The density of atoms in the excited state N_e is the same for both intensities and from I_s/I_l follows the sensitivity of the VUV spectrometer:

$$k = \frac{A_l \lambda_s}{A_s \lambda_l} \cdot \frac{I_s^{cts}}{I_l} . \quad (2.22)$$

In the end, one pair of transitions was found to be suitable for the calibration. They are emitted by He^+ . The long wavelength light is emitted via the $n = 4 \rightarrow n = 3$ transition at $\lambda = 468.6$ nm, while the short wavelength stems from $n = 4 \rightarrow n = 1$ at $\lambda = 24.3$ nm. These transition were found in [33]. Since the helium transition at $\lambda = 24.3$ nm is very weak under normal plasma operation a helium injection was applied in discharge #24176 from 5.15 s to 5.6 s to increase the signal to noise ratio. The sensitivity at $\lambda = 24.3$ nm was evaluated on the time interval $t = [5.16, 5.6]$ s and a 20% error was assumed for the absolute intensity observed with the visible spectrometer. The LOS of the visible spectrometer is the same as the one of the SPRED, since the light is extracted with a

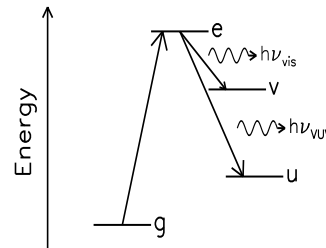


Figure 2.6: Schematic drawing of the 4 energy levels used in the branching ratio method.

mirror at the end of the vacuum duct of the SPRED spectrometer. From the line intensities observed in this discharge the sensitivity was evaluated to be $k = 2.17 \pm 0.70 \cdot 10^{-13}$ cts/(Ph/m²).

This single point for which the sensitivity is now known, allows for the calculation of the sensitivity over the full spectral range of the SPRED spectrometer. The wavelength dependence of the sensitivity is given in [29] for a similar SPRED spectrometer. Even though the voltages applied to the image intensifiers differ between the system presented in [29] and the system presented here, it is justified to simply shift the sensitivity curve in order to agree with the sensitivity evaluated for the AUG SPRED at $\lambda = 24.3$ nm, thus obtaining an absolute intensity calibration over the full wavelength range of the spectrometer.

2.3 Tungsten Concentration Measurements

The tungsten concentrations in AUG are routinely evaluated from the tungsten features in the 5 nm spectral region. The evaluation delivers concentrations at two electron temperature ranges, one

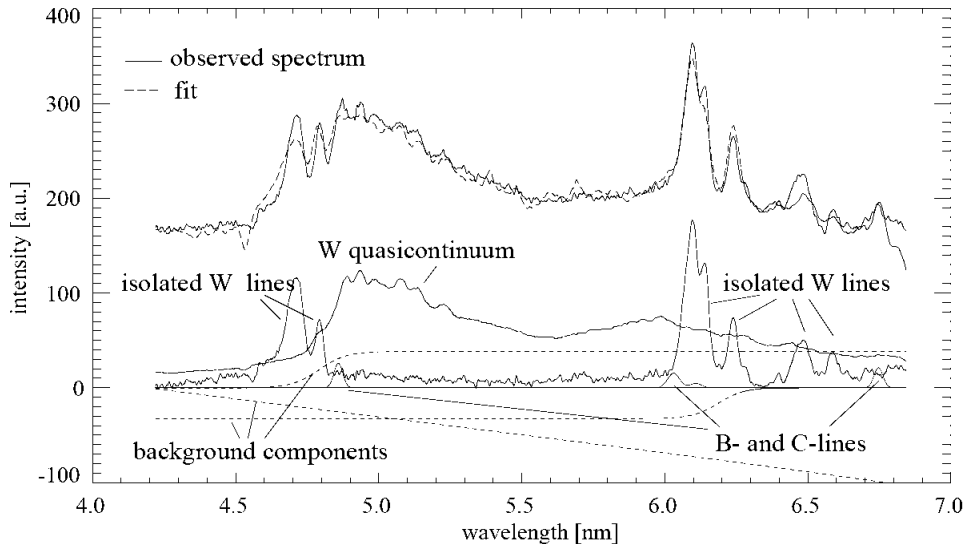


Figure 2.7: Tungsten spectrum at 5nm and the result of the fitting procedure used to evaluate the quasicontinuum radiation. On a broad quasicontinuous spectral band several individual lines are located. (Taken from [37])

located at $T_e \approx 1$ keV, the other extending from $T_e \approx 2$ keV to the plasma center. The evaluation procedure relies on calculated cooling factors for the different ionisation stages, therefore a significant experimental effort has been undertaken to verify and further improve the accuracy of these factors [34].

2.3.1 Radiation from Highly Charged Tungsten

The tungsten radiation in the spectral range $\lambda = [4.5, 7]$ nm exhibits a strong quasicontinuous feature and many distinct single lines as shown in figure 2.7. Due to its brightness, this tungsten radiation has drawn much attention since it was first observed in the late 1970s in the ORMAK [35] and PLT [36] devices. It attracted additional interest with the transition of AUG from a carbon device to a tokamak with a full tungsten wall.

With the installation of the first tungsten tiles a new method to evaluate the tungsten concentration in the presence of a continuous tungsten source became a pressing matter. The method used before the installation of the tungsten tiles relied on the evaluation of the bolometer data. This evaluation was only possible for scenarios in which a controlled tungsten injection into an otherwise tungsten free plasma led to a sudden increase in radiation. After subtracting the background radiation observed immediately before the tungsten injection a deconvolution of the bolometer data delivered the profile of the radiation emitted specifically by tungsten:

$$P_W = n_e^2(r, t) c_W(r, t) p_W(r, t), \quad (2.23)$$

with $n_e(r)$ the electron density profile, $c_W(r)$ the tungsten concentration profile and $p_W(T_e(r, t))$ the calculated radiation loss parameter of tungsten. Equation 2.23 delivers the tungsten concentration profile, if n_e and p_W are known. A continuous tungsten source renders this method useless, since no tungsten-free radiation background can be subtracted.

The method currently in use was first presented in [38] and then further developed in [37] and [34]. The original evaluation method only used the information present in the quasicontinuous feature, while the latest version also includes the information from the individual lines found in the spectrum at temperatures $T_e > 1.8$ keV. The evaluation from the quasicontinuum will be presented first. In contrast to the determination of the tungsten concentration from the bolometer signals, where full profiles of $c_W(r)$ were obtained, the evaluation of the spectroscopic data only gives $c_W(r_{L,qc})$ in the plasma layer where the quasicontinuum-emitting ions exist. The ion stages responsible for the quasicontinuum are $W^{27+} - W^{35+}$. They are located in the temperature range $0.8 < T_e < 1.6$ keV, radiating mainly at 1 keV [34]. This defines the effective thickness of the layer Δr , in which the tungsten concentration can be evaluated from the quasicontinuum. The measured intensity from the quasicontinuum is then:

$$I_{W,qc} = \int d\lambda \int_{\Delta r} dr n_e^2(r) c_W(r) \eta(r, \lambda) C_{GI}^{cal}(\lambda), \quad (2.24)$$

where $\eta(r, \lambda)$ is the emissivity summarizing the excitation rates and branching ratios of all transitions contributing to the quasicontinuum in this wavelength region. The sensitivity of the spectrometer, in this case a grazing incidence spectrometer (GI), is given by $C_{GI}^{cal}(\lambda)$. Assuming that the emissivity and the tungsten concentration are constant over the emitting plasma layer Δr the integration over λ and r leads to an equation with mean values $c_{W,qc}$, $\bar{\eta}_{qc}$, $C_{GI,qc}^{cal}$ and $n_e(r_{L,qc})$:

$$I_{W,qc} = n_e^2(r_{L,qc}) c_{W,qc} \bar{\eta}_{qc} C_{GI,qc}^{cal} \Delta r. \quad (2.25)$$

The calibration factor $C_{qc}^{cal} = \bar{\eta}_{qc} C_{GI,qc}^{cal} \Delta r$ is determined by comparing

$$c_{W,qc} = \frac{I_{W,qc}}{C_{qc}^{cal} \cdot n_e^2 r_{L,qc}} \quad (2.26)$$

with the tungsten concentration $c_{W,bolo}$ obtained from the bolometer evaluation after tungsten injection. The value used for the electron density is approximated from the line averaged DCN-interferometer channel H-1. The difference between the averaged value \bar{n}_e and the actual density profile is small for the evaluation of $c_{W,qc}$ in H-mode discharges, since the density profiles in these type of discharges are usually flat. However, in discharges with peaked central tungsten density or hollow temperature profiles this standard evaluation method is no longer suitable.

Even though the bolometer evaluation is not suitable for an absolute evaluation of the tungsten concentration, it still allows for the determination of relative changes in concentration. This relative change in concentration is used at the beginning of each campaign to reassess the calibration factor for the GI spectrometer C_{qc}^{cal} .

The evaluation of the individual lines in the spectral range $4.5 < \lambda < 7.0$ nm follows the same concept as for the quasicontinuum. Using the line radiation from $W^{40+} - W^{46+}$, it allows for the determination of the tungsten concentration in the temperature region $1.8 < T_e < 5.0$ keV which covers the range of central temperatures for most H-mode discharges. The calibration of the GI sensitivity for the individual lines was performed once via the double branching rate method and once via cross calibration with the quasicontinuum intensity at 5 nm and the bolometer signals (for a detailed description please refer to [37]). Both calibrations agreed within 20%.

2.3.2 Grazing Incidence VUV-spectrometer

The major workhorse for the evaluation of tungsten concentrations is a 2.2 m grazing incidence spectrometer manufactured by McPherson. A detailed description is given in [39], while here only

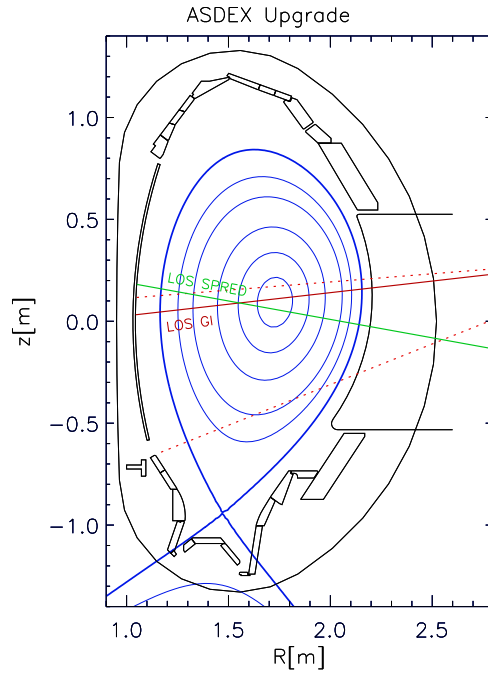


Figure 2.8: *LOS of the SPRED and the GI spectrometer. The dashed lines for the GI indicate the accessible range of LOS, while the solid line shows the standard LOS.*

the major features of the spectrometer will be covered. The spectrometer is equipped with two microchannel plates (MCP), each observing a wavelength interval of $\Delta\lambda \approx 4$ nm. The full wavelength range of the spectrometer is $\Delta\lambda_{tot} = [2, 50]$ nm. Each MCP can be moved independently along the Rowland circle to observe an interval of width $\Delta\lambda$. The Rowland circle setup in combination with a shallow angle of incidence $\alpha = 2^\circ$ ensures a nearly constant reflection for the full spectral range. This gives the possibility to keep one MCP on the position suitable for the tungsten concentration measurement, while the second MCP is free to observe other parts of the accessible spectral range $\Delta\lambda_{tot}$.

Besides its wide spectral range its variable LOS makes this spectrometer very valuable for the investigations performed in this study. Figure 2.8 shows the range of accessible LOS. However, for each discharge only one LOS can be set, since the equipment moving the LOS is located in the experiment hall and is not designed for remote operation.

The detector system is similar to the one of SPRED spectrometer and will be presented in the following section. It should be mentioned that during the investigations performed during this study a damage to one of the MCPs was detected.

2.4 Detector Systems

The detector systems of the SPRED as well as the grazing incidence spectrometer are very similar. A schematic view of the detector is shown in figure 2.9. The VUV photons from the plasma are converted by the photoelectric effect into electrons in the open MCP. The primary electrons are accelerated by an electrical field along the MCP which has a thickness of a few hundred μm . They travel in thin channels of $8 \mu\text{m}$ diameter, that have an angle of 10° to the MCP axis. The electrons

are multiplied when hitting the channel walls, creating an avalanche effect. This intensified electron signal is converted into visible light on a phosphor screen. The voltages applied to the MCP and screen are $HV_{MCP,GI} = 1.2\text{ kV}$ and $HV_{Scr,GI} = 5.0\text{ kV}$ for the GI and $HV_{MCP,SP} = 1.0\text{ kV}$ and $HV_{Scr,SP} = 6.0\text{ kV}$ for the SPRED. The screen not only converts the electron signal from the MCP into visible light, but with the high voltage applied to it, avoids a divergence of the electron beam leaving the MCP. With the conversion into visible light, normal optical tools can be applied. The fiber-optical coupler, a so called taper, reduces the size of the image to the dimensions of the camera. The taper is fixed externally only for the SPRED spectrometer, where it reduces the image from $d = 4.0\text{ cm}$ to $d = 2.5\text{ cm}$.

The camera system is a device recently installed at the GI and SPRED spectrometers. Its most outstanding feature is its frame rate which allows to continuously record spectra at a frequency of 1000 full spectra per second. This is the fastest value among the detectors installed on the VUV/Soft-Xray spectrometers in AUG which usually work at 3 to 4 ms per full spectra. With this temporal resolution it becomes possible to observe transport effects at the plasma edge, *e.g.* the effect of ELMs on the edge tungsten radiation.

As can be seen from figure 2.9 the camera is composed of off the shelf parts and parts manufactured at the Institut für Plasmaphysik (IPP) in Garching, Germany. The sensor itself is a NMOS linear photodiode array (Hamamatsu S3904-F). This is a 1024 pixel array, with high signal to noise ratio, low dark current and excellent output linearity. Each pixel functions as a small capacitor, that is charged to a certain voltage before measurement and then discharged by the impacting photons. The number of detected photons is calculated from the peak value of the voltage applied during the recharge process. The low dark current and high signal to noise ratio is achieved by correlating every irradiated pixel to an identical pixel, that is protected from irradiation. The “blind” pixel measures the dark current which is then subtracted from the value measured with the “live” pixel, producing a signal that is nearly free of dark current. Under optimum conditions the readout data rate is 2.0 MHz which translates into a frame rate of slightly below 2 kHz. The sensor is operated by a driver card (Hamamatsu C7883). This card provides the timing of the voltages needed to run the image sensor and delivers the output signal in form of the voltage characteristic described above. The triggers for each readout cycle are applied from an external source. This source are the components designed and built at the IPP. They provide the triggers for the readout, the possibility to work with different gain factors, allow for offset subtraction and convert the voltage signal into a 14bit digital signal which is then transferred by optical fibers to a serial IO card, transferring the digital signal to a computer. The camera system as described above was tested for linear dependence of output height on irradiation intensity, gaussian noise characteristic, proper gain functionality, spatial photoresponse

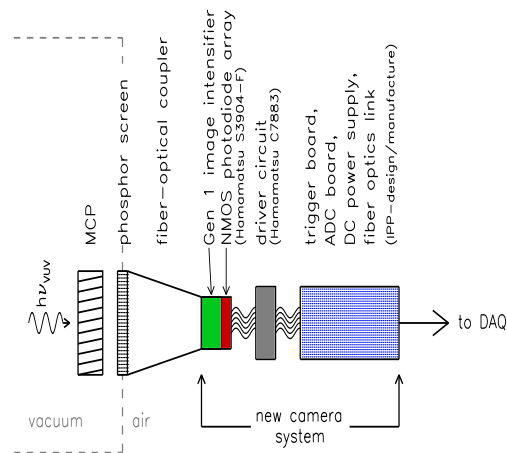


Figure 2.9: Schematic drawing of the detector system installed on the SPRED and GI spectrometer

uniformity and shielding from electromagnetic stray radiation. While most tested properties fulfilled the requirements, the photoresponse non-uniformity was much better than expected (expected: $\pm 5\%$, measured $< \pm 2\%$) and the electrical shielding was catastrophic. The problem of the stray e-m radiation was caused by the high voltage supply of the image intensifier located directly in front of the camera. It was solved by creating a Faraday cage around the driver card. The 1st generation image intensifier (Proxitronic BV2533QX10100N) was also tested and accepted for linearity, noise characteristic and photoresponse uniformity.

Chapter 3

VUV Tungsten Spectra in the Plasma Edge

The study of tungsten transport in a tokamak plasma relies mainly on passive spectroscopy. It is therefore of crucial importance for transport studies to understand the spectra emitted by tungsten. The spectral region of interest of this investigation lies in the vacuum ultraviolet (VUV) range $\lambda = [10, 25]$ nm and contains radiation from highly ionized W^{45+} down to W^{15+} and below [40,41]. While highly ionized tungsten (W^{39+} and above) exhibits few distinct spectral lines in this spectral range, the radiation from the lower ionization stages is emitted as thousands of individual lines. The small wavelength separation of these lines exceeds the resolution capabilities of the used spectrometers creating a quasi-continuous feature in the observed spectra (see figure 3.1). This spectral feature is very interesting for edge transport studies, since the radiating W-species exist in the electron temperature range $0.1 < T_e < 1.5$ keV which includes the temperatures of the steep gradient region and the pedestal top of the AUG H-mode plasmas.

The characterization of this quasi-continuous feature was approached by two means. First, by a series of dedicated discharges, in which laser ablations created a controlled tungsten source and the emitted W-radiation was observed along varying lines of sight. This method will be discussed in section 3.2. Second, by evaluating discharges that experienced central tungsten accumulation and a successive drop in electron temperature. The following section will deal with the latter approach.

3.1 Characterisation via Tungsten Accumulation

Plasmas in AUG, being a tokamak with a full tungsten wall, usually contain tungsten concentrations in the range $c_W \approx 10^{-5}$. In plasmas with central wave heating the tungsten is distributed evenly from pedestal top to the plasma center. Without central wave heating the turbulent transport in the plasma center is reduced and neoclassical transport becomes predominant. In case of central density peaking this causes a neoclassical inward drift for impurity ions which is strongly dependent on the charge of the impurity [15, 42]. For tungsten this inward drift is substantial, leading to a peaked central tungsten concentration on time scales of tens of milliseconds. Even in the hottest AUG plasmas tungsten is only partially ionized which makes it a very powerful radiator and leads to a high cooling factor [28]. The increased radiation from the plasma core results in a drop of central temperature and often in an early stop of the discharge.

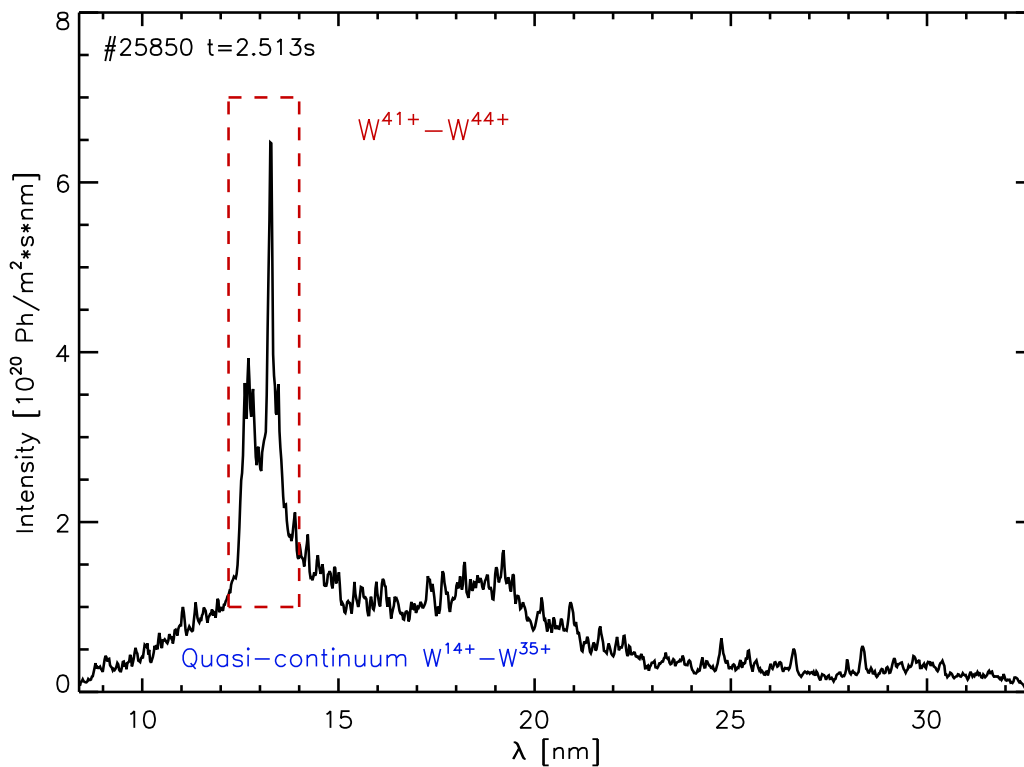


Figure 3.1: Spectrum of a typical AUG H-mode discharge as observed with the SPRED-spectrometer

In discharge #25180 the observed tungsten accumulation did not lead to a radiative collapse and the end of the discharge but to a plasma with reduced central temperature and a very peaked radiation profile. The electron temperature then decayed slowly over the time span of several hundred milliseconds from ≈ 1000 eV to ≈ 250 eV, figure 3.2.

As mentioned in the previous chapter, the spectra observed with the SPRED spectrometer are line of sight integrated. This makes evaluation of the spectra with respect to differentiating temperature effects rather difficult, since the temperature exhibits a continuous change along the line of sight. The discharges chosen for the present evaluation offer a very good possibility to disentangle the contributions to the spectra at various low T_e . First, there is the effect of a flat T_e -profile over a wide plasma radius which allows to determine a dominant temperature for each spectrum. Second, the additions to the spectrum from temperatures lower than the dominant temperature can be assumed to be minimal, since the radiation profiles are peaked

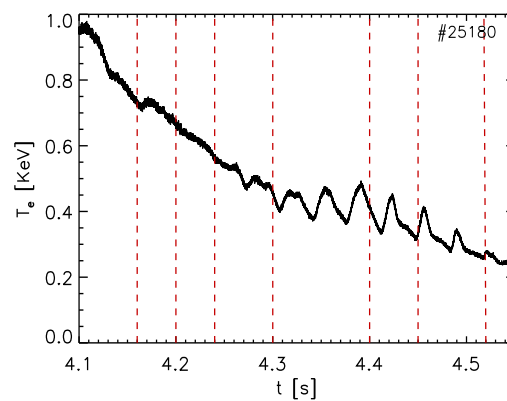


Figure 3.2: Central T_e from ECE-diagnostic. The broken red lines indicate the time points at which spectra were evaluated.

inside the flat T_e -region for the chosen time points and it can be assumed that most of the detected light originates from this region.

Since the discharges exhibit a transient behaviour during the investigated time intervals, it is important to determine whether the ion distribution of tungsten equilibrates on the given time scales. Using the recombination rate coefficients found in [40], the time needed for the recombination processes from W^{40+} down to W^{20+} to take place was calculated to be $\tau_{rec} = 0.63$ ms. For this calculation the central electron temperature ($T_e = 740$ eV) and density ($n_e = 4.2 \cdot 10^{19} \text{ m}^{-3}$) found in the experiment at $t = 4.160$ s were used. This allows to assume equilibration of the different tungsten ionization stages at each observed timepoint. It is noteworthy that the electron temperature, obtained from electron cyclotron emission (ECE), is flat inside $\rho_{pol} < 0.6$ for the time points chosen for evaluation. The T_e -profiles are presented in the left row of plots in figure 3.3. The red horizontal line drawn in each of these plots represents the average electron temperature inside $\rho_{pol} < 0.6$ and was added to guide the eye.

In order to extend the range of observed temperatures, another spectrum from a different discharge was added to the series (first line in figure 3.3). This discharge (#25658) also suffered from central tungsten accumulation in the ramp-down phase and shows a flat temperature and a peaked radiation profile. It was therefore considered useful for this investigation.

The deconvolution of the bolometer data is shown in blue in the left row of plots in figure 3.3. It is obvious that for discharge #25658 the deconvolution suffers from artefacts and displays negative emissivities for $0.75 < \rho_{pol} < 1.0$. The main point however, the peaked radiation profile of the plasma, is not affected by this slight error. For #25180 the displayed deconvolutions were achieved with a better quality. Since only the profile of the radiation is of interest the radiation data was normalized to fit into the graphs. The SPRED spectrometer has an almost radial LOS going through the plasma centre. Thus the radiation profiles versus ρ_{pol} also reflect the radiation profile along the LOS of the SPRED. An interesting feature of this discharge is that for time points $t > 4.4$ s the radiation profiles become hollow. The maximum is no longer located in the plasma center, but has moved further outwards. For the investigation undergone in this work this has no negative effect, since the peak is still located well within the flat T_e -region.

Transitions from elements other than tungsten are visible in the plots on the right hand side of figure 3.3. This line radiation exhibits a strong time evolution which means strong evolution with temperature. These dynamics allowed for the identification of the individual lines, as shown in figure 3.3. The identification rests upon the wavelength information obtained from the atomic data base by Kelly [43] and the temperature dependence of the fractional abundance of the various elements and ionization stages. The ionisation and recombination rates needed to determine the fractional abundance were taken from ADAS [44]. The presence of these transition lines is the result of impurity events during the discharge and therefore the impurities differ in the two discharges evaluated for this graph. While in #25180 Cu, Ni, Al and Fe are present, in #25658 only Fe and Al are detectable in this stage of the discharge.

Tungsten shows two distinct features in the observed spectral and temperature range. One is the radiation peak at longer wavelengths which is located at $\lambda = 21$ nm for $T_e = 190$ eV and moves to $\lambda = 18.5$ nm for $T_e = 790$ eV. This shift of radiation towards shorter wavelengths makes it feasible to define a wavelength range for which tungsten radiation originates mainly from plasma regions with $T_e < 450$ eV.

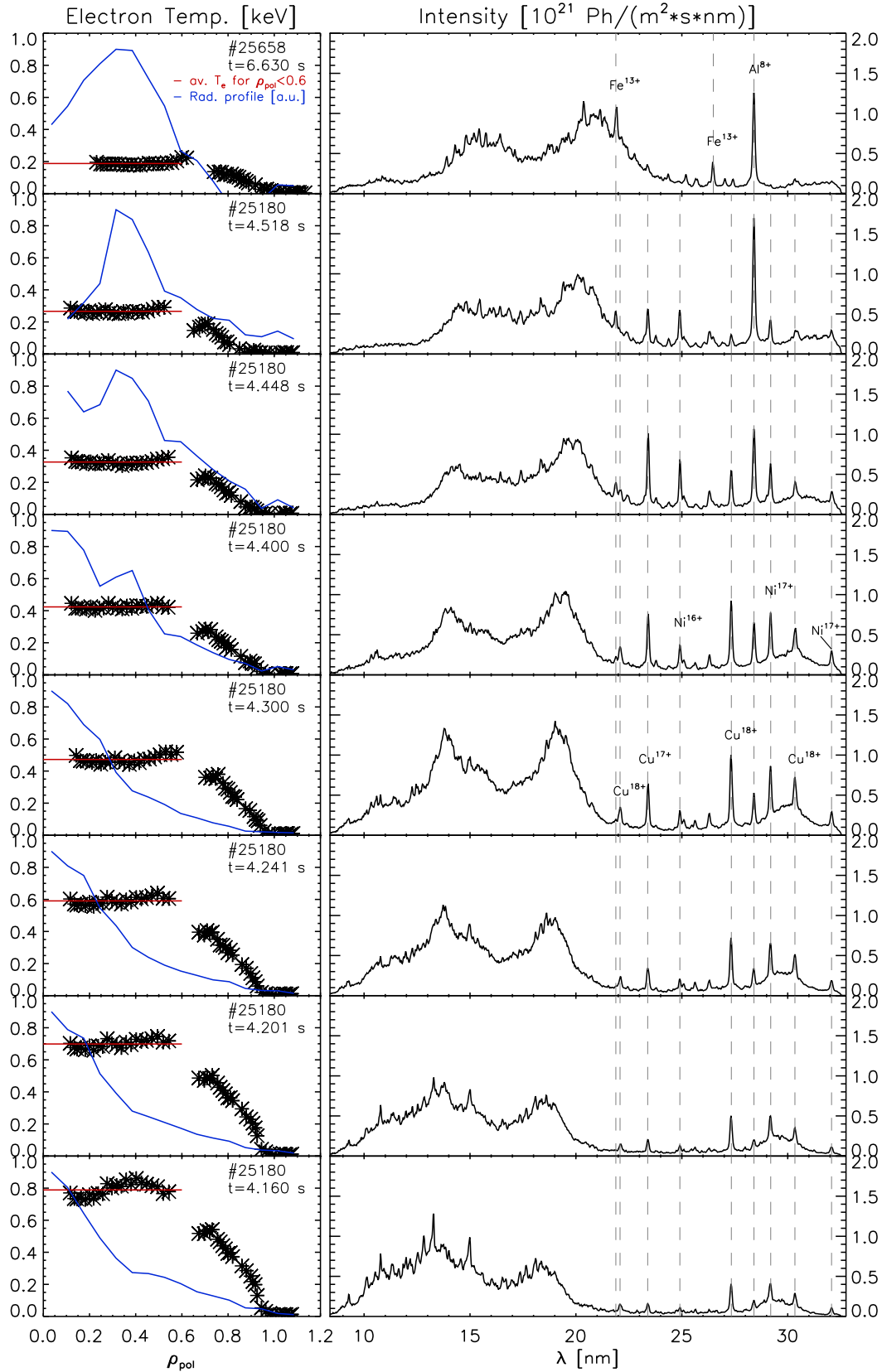


Figure 3.3: VUV Spectra at different electron temperatures. The spectra were recorded with the SPRED spectrometer and are dominated by emissions from tungsten. The left column shows information on the radial electron temperature profile (black stars and red line) and the radial radiation profile (in blue).

The selection of the wavelength range was restricted by several demands:

- tungsten radiation in the specific wavelength range measured in typical AUG discharges should be clearly above background level, even at low tungsten concentrations. This restriction defines the limit for the upper wavelength to be $\lambda = 23$ nm.
- contributions from tungsten at $T_e > 450$ eV should be minimal. With this the lower wavelength of the interval is set to $\lambda = 21$ nm.
- the wavelength interval should not contain strong transition lines from neither intrinsic impurities like carbon, nitrogen or oxygen, nor from frequently injected impurities like argon or neon. This leads to the final restriction of the wavelength interval to $\lambda = [21, 22]$ nm.

In order to address the question of the tungsten ionisation stages which are emitting the light in the investigated wavelength interval, one has to use transport code calculations. The corona ionisation equilibrium gives the fractional abundances without transport and with constant electron temperature. Figure 3.4 shows the results of a calculation with corona ionisation equilibrium (a) and on a H-mode plasma background with transport (b). In the corona approximation the low ionisation stages exist each in a very narrow temperature interval and their maximum abundances are quite well separated.

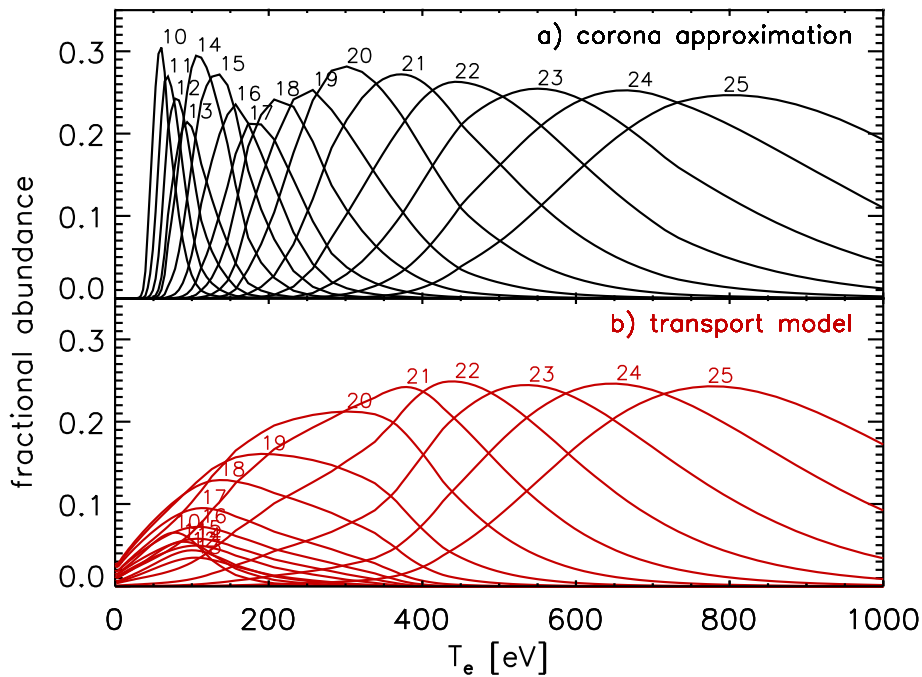


Figure 3.4: Fractional abundances for various tungsten ionisation stages over T_e a) in the corona ionisation equilibrium and b) from STRAHL calculations, including transport

This is in strong contrast with the ion stage distribution which was obtained with the 1-D transport code STRAHL. The impact of transport is dominating the distribution of the stages W^{20+} and below. This is the temperature range of the ETB in which transport has a strong effect on the distribution of the ionisation stages. For higher temperatures the effect of transport on the distribution is much smaller and there is almost no deviation from the corona ionisation

equilibrium for ion stages W^{23+} and above. The reason for widening of the low charge distributions with transport are the timescales needed for ionisation and recombination which are on the same order as the time needed to cross the very steep temperature gradient in the ETB. The ions just do not have the time to equilibrate on their path through the ETB. The regions of the plasma where temperature gradients are small allow for the equilibration of the ionisation stages, leading to the good agreement with the corona ionisation equilibrium.

The ionisation stages of tungsten that are contributing to the emission in a specific temperature range can be estimated using the fractional abundances found in that specific temperature range. For this estimation, the temperature is first mapped on a grid of the normalized radius ρ_{pol} . Building the integral of the fractional abundance f_i for each ion stage i over $\rho_{pol}^{ETB} = [\rho(T_{e,min}), \rho(T_{e,max})]$ and normalizing by the sum over all fractional abundances one gets the averaged fractional abundance for ion stage i in the radial range ρ_{pol}^{ETB} :

$$f_{av,i} = \frac{\int_{\rho_1}^{\rho_2} f_i(\rho_{pol}) d\rho_{pol}}{\rho_2 - \rho_1} \quad (3.1)$$

This averaged fractional abundance gives a weight to each ion stage found in the specified plasma region. For the case presented here we are interested in the temperature range $100 < T_e < 450$ eV defined by the spectral range $\lambda = [21, 22]$ nm which is the temperature range of the ETB and the pedestal top. This averaged ETB fractional abundance is a weighting factor for each ion stage inside ρ_{pol}^{ETB} and can give a first rough estimate of the radiating shell. It peaks strongly at W^{21+} . In addition, the distribution of the weighting factors is quite narrow with $f_{av,i}^{17,24} < f_{norm,21}/e$.

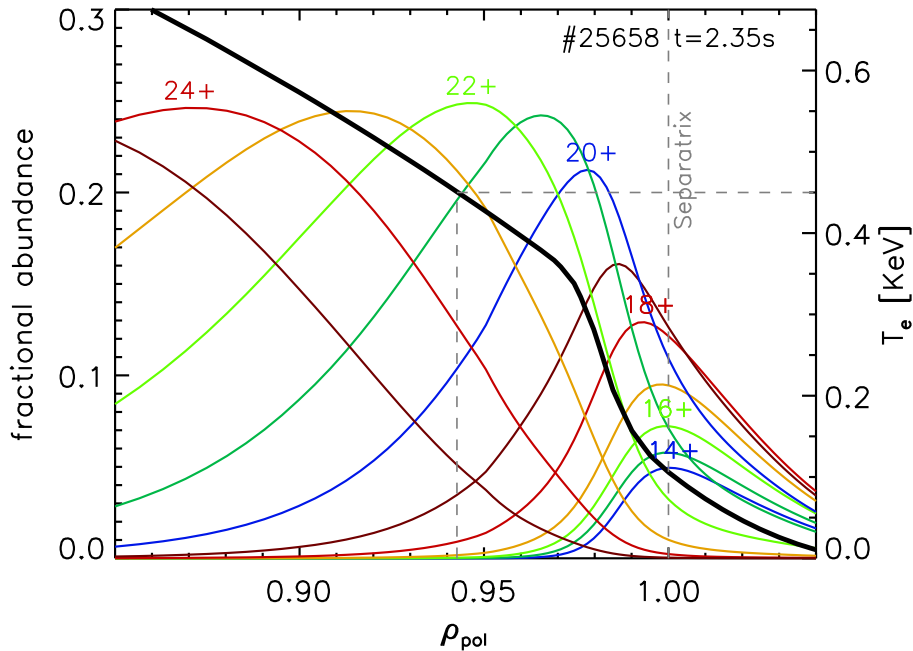


Figure 3.5: Fractional abundances for various tungsten ionisation stages in the edge of H-mode discharge #25658. The black line shows T_e

These results were obtained using the 1-D transport code STRAHL. Electron temperatures and densities extracted from #25658 on inter-ELM time intervals in the time range $t = [2.0, 2.7]$ s were

used to run the code. The assumptions regarding tungsten radial transport are following the findings by [17] and will be only sketched at this instance. Suppression of turbulent transport in the ETB leads to the reduction of the radial diffusion coefficient while a strong, localised neoclassical pinch ($v_d = -80$ m/s) is assumed. The diffusion coefficient increases fast at radii smaller than the pedestal top and decays slowly to neoclassical values in the plasma core. The radial distribution of the various tungsten ionisation stages surely changes slightly with discharge parameters, but the main point remains valid: the radiation observed in this spectral interval originates from the very outmost layers of the core plasma and the full ETB and the dominating ionization stages are centered closely around W^{21+} . The radial distribution of the ionisation stages are shown in figure 3.5.

The wavelength interval defined this way is therefore extremely helpful to obtain information on tungsten from the steep gradient region. With the fast cameras (1 ms framing rate) mounted on the spectrometer, it even becomes possible to observe ELM-resolved tungsten time traces from the plasma edge. The result is shown in figure 3.6. As was to be expected, the time trace (red) of this wavelength-integrated photon flux is strongly disturbed by ELMs. For the chosen discharge the temperature at the pedestal top was 450 eV and this means that the observed radiation originates solely from the steep gradient region. The second time trace in figure 3.6 shows the time evolution of tungsten at electron temperatures above 450 eV which is the second region of interest of this study.

The identification of this second feature followed the same path as described before. However, the restrictions applied in order to find a suitable wavelength range differed slightly. While the line radiation from other impurities set the limit to the interval studied above, line radiation from tungsten itself limits the accessible range in this case. A look at figure 3.1 reveals that the lines of $W^{41+} - W^{45+}$ are located exactly on top of the interesting quasicontinuum region around 13 nm. These strong lines do not disappear unless the plasma cools down below $T_e < 1.9$ keV. However, this is not the case for most of the H-mode plasmas in AUG which pushes the useful wavelength range to smaller λ . Taking into consideration that the sensitivity curve of the grating declines by a factor of two from 15 nm to 10 nm [29], the lower wavelength limit was chosen to be $\lambda = 11$ nm. To allow for enough distance from the dominating W-transitions the upper limit was set to $\lambda = 12$ nm. The final wavelength interval for the observation of tungsten at electron temperatures above 450 eV is therefore $\lambda = [11, 12]$, nm.

The radiative contributions from tungsten at lower T_e are negligible in this wavelength interval which sets a rather hard outer boundary for the observed plasma region. For the inner (high T_e) boundary the results are not that clear, since the series shown in figure 3.3 terminates at $T_e \approx 800$ eV.

This question was approached by means of tungsten ablation via laser irradiation, also known as Laser Blow Off (LBO). During a LBO a small amount of tungsten is heated by a short intense laser pulse (1.2 J in 6 ns) and accelerated by the rocket effect. The tungsten then crosses the SOL

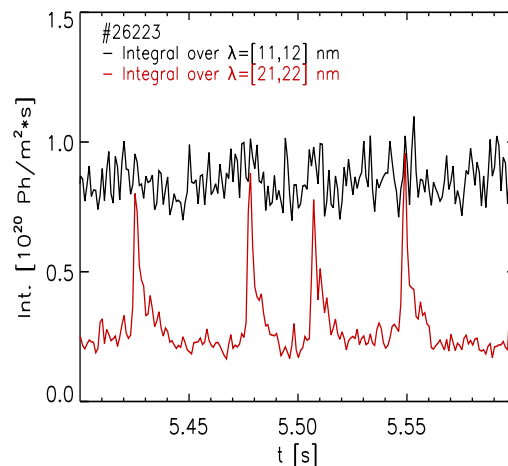


Figure 3.6: Time traces of the intensity of the two spectral intervals defined for $T_e < 450$ eV (red) and $T_e > 450$ eV (black)

as a narrow beam of neutral particles that become ionised mainly around the separatrix. Figure 3.7 shows the time traces of the intensity in three wavelength intervals, each corresponding to different temperatures and ionisation stages. The black time trace is the integrated intensity from tungsten at the ETB [21, 22] nm, while the red curve represents the tungsten radiation from ionisation stages $W^{30+} - W^{33+}$ [5.0, 5.3] nm, with the fractional abundance peaking at $T_e \approx 1.5$ keV. The time trace of the wavelength interval [11, 12] nm is plotted in blue. The decay of this and the black time trace from the ETB region obviously happens on two timescales. The characteristic times for both decay phases have been determined by fitting two exponentials to the data. The fast decay phase of both signals exhibits approximately the same decay time, while the second phase decays much slower for the blue signal.

	τ_{black} [ms]	τ_{blue} [ms]	τ_{red} [ms]
Phase I	3.3 ± 0.2	2.7 ± 0.5	-
Phase II	23.7 ± 0.6	52.7 ± 5.0	48.4 ± 2.2

The component of the fast decay is negligible after ≈ 8 ms in the blue signal and the signal can be fitted with only one exponential for $t > t_{LBO} + 8$ ms. Unlike the other two radiation signals, the radiation from $W^{\approx 30+}$ (red trace) reaches its maximum only ≈ 9 ms after the LBO and then shows a plateau phase (≈ 12 ms) before the decay sets in at $t = t_{LBO} + 21$ ms. This decay then happens with the about same decay time as was found for the blue signal. This was to be expected, since in the main plasma the tungsten concentration profile after a W-LBO decays self similarly after equilibration [11]. From the lag between the slow decay phases of the red and the blue signal it can be deduced that the major radiating shell responsible for the intensity in the blue signal must be located between the ETB and the radiating shell of the W^{30+} ions.

As for the ionisation stages responsible for the radiation observed in this wavelength interval an estimate of the upper limit (W^{29+}) can be given through comparison with the innermost (red) timetrace. Using the method of the normalized fractional abundance on the temperature range $450 < T_e < 1100$ eV this spectral region now translates into the ionisation stages W^{21+} up to W^{28+} . The peak of the distribution of these stages is found at $T_e \approx 650$ eV. However, the width of the distribution is rather large and a significant amount of these ionisation stages are found at temperatures as high as $T_e \approx 1.5$ keV. Therefore, it must be assumed that the radiating shell is significantly narrower than the radial distribution of the involved ionisation stages. It should be noted, that the steep rise and fast decay of the intensity in the wavelength interval $\lambda = [11, 12]$ nm suggests, that the usually small contributions from the ETB region to its intensity are strongly increased during an LBO and have to be taken into consideration for such events.

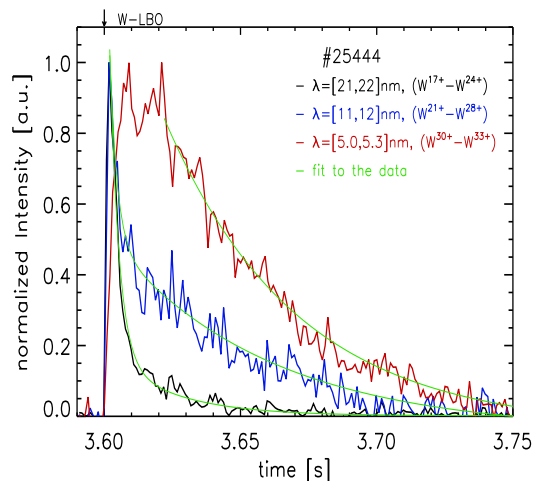


Figure 3.7: Time traces of the normalized intensity for three distinct W-quasicontinua intervals with W-LBO.

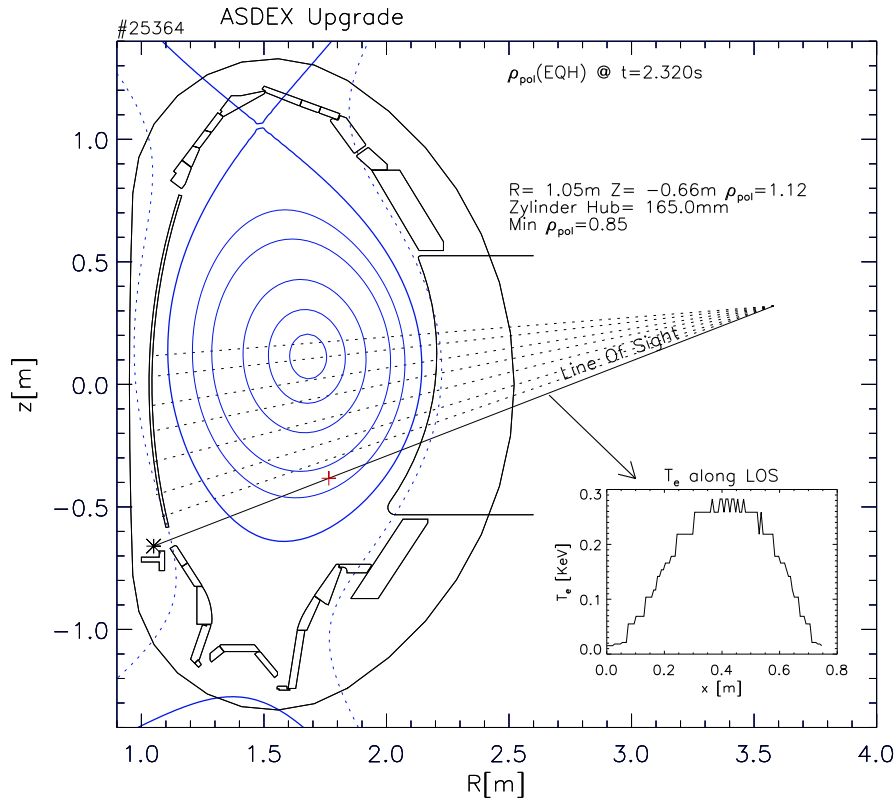


Figure 3.8: Poloidal cross section of AUG with equilibrium of #25364 at $t = 2.32$ s and LOS of GI spectrometer. The dotted lines show the range of possible LOS for the spectrometer. The embedded graph depicts the electron temperature along the LOS of the spectrometer inside the separatrix. $x=0$ is at the HFS.

With the identification of these new features it becomes possible to map the spectral information onto a radial temperature profile, thus obtaining information on the position of the radiating region.

3.2 Characterisation via Tungsten-LBO

The second approach to characterize the tungsten emission at electron temperatures below 1 keV utilized controlled injections of tungsten by laser ablation. This approach made use of a Grazing Incidence spectrometer (GI). Crucial for this approach is the mounting of the GI spectrometer at AUG which allows for the change of line of sight between discharges. It was therefore possible to explore tungsten emissions in the same type of discharge but at different temperatures by simply changing the line of sight and heating scheme. In addition, the controlled injection of tungsten allowed for the exclusion of other impurities from the recorded spectra. Using the electron temperature profiles the spectra were deconvoluted and tungsten emissivities were obtained in the spectral range $\lambda = [20.5, 25.5]$ nm.

The experimental setup is shown in figure 3.8. The discharges were run in Upper Single Null (USN) to have a higher power threshold for the LH-transition. Therefore, the discharges stayed in L-mode and auxiliary heating was at maximum 1.2 MW NBI power and 0.8 MW ECRH power. For

this investigation three different LOS were chosen, therefore each LOS gives only one temperature profile with a certain maximum temperature, depending on the innermost flux surface that the LOS encounters. With such a setup the temperature steps would have been too large in order to perform a deconvolution of the spectral data. Hence, smaller temperature steps had to be achieved. This task was tackled by two means. At first, the plasma was shifted upwards during the discharge, thus scanning the plasma. Unfortunately, the temperature profiles across the flux surfaces perpendicular to the LOS were too flat and the steps in z-direction too small to result in a significant change of the temperature profile. At second, the heating power was changed during the discharge. Each discharge experienced 4 heating phases: 1.6 MW NBI+ECRH, 1.2 MW NBI, 0.8 MW ECRH and no auxiliary heating. This approach lead to the desired temperature steps which are on average 80 eV.

Injection of tungsten into the plasma usually results in a drop of the temperature, due to increased radiation. This drop is well monitored with the ECE diagnostic. The affected region extends instantaneously up to electron temperatures around 700 eV. The temperature behaviour of the plasma from the edge up to this temperature range is similar. After a short decline (≈ 10 ms) the temperature stabilises at a value lower than before the tungsten injection, remains at this level for about 25 ms and finally returns to the initial value after a period of 50 ms. For plasma regions further inside the picture is almost the same, with the modification that the decline phase after the LBO lasts longer (≈ 15 ms at $T_e = 900$ eV) and the flat, reduced temperature phase is delayed. The time scales found in these temperature dynamics are big enough to rightfully assume equilibration of the individual tungsten ionisation stages. Since this investigation aims at the characterization of W-radiation below 1 keV electron temperature, the time window suitable for spectral analysis is 15 to 25 ms after the LBO. During this period plasma parameters are constant and the detected radiation can be related to the specific temperature profile measured in this time interval.

The dynamics of the injected tungsten reflects also on the intensity of the detected light. After the LBO the transport into the plasma leads first to an increase of tungsten emissions which lasts up to 7 ms for the innermost LOS setting. Then, unlike for the temperature, the intensity of the tungsten emissions does not reach a plateau phase but starts decaying immediately after reaching the peak. This decay is, however, rather slow and the intensity drops on average by less than 25% in the aforementioned time window. An average of the recorded spectra was calculated for this time span to increase the signal to noise ratio. All spectra from the GI spectrometer presented in this framework are averages over 10 ms intervals starting 15 ms after the LBO.

The deconvolution procedure mentioned in the introduction consists of 4 steps:

- obtaining the T_e -profile along the LOS
- correcting for the different strength of each LBO using the total W-VUV intensity
- correcting the GI-spectra for higher order diffraction
- deconvoluting the spectra with respect to temperature

The determination of the T_e -profiles along the different LOS is itself a multistep process. Since the position information of the T_e -data is given along a single line in real coordinates, a mapping on flux surfaces is necessary. It is therefore mapped on a ρ_{pol} -grid, assuming equal temperature on the individual flux surfaces. The LOS trajectory of the spectrometer is also first calculated in real coordinates and then mapped onto the same ρ_{pol} -grid. In the last step a temperature value is assigned

for each point along the LOS resulting in the profile. This mapping is performed for all time points in the investigated time interval after the tungsten injection. All calculated temperature profiles are then averaged to increase the signal to noise ratio. The result can be seen in the embedded plot in figure 3.8 and it is obvious that the profile is rather coarse. To reduce the coarseness an 8-point smoothing was applied. What is not visible in this plot is the effect of defective ECE channels. Some channels exhibit jumps in the detected temperature which results in useless profiles. Contributions from these channels are excluded from the evaluation, if their temperature value deviates more than 1σ from the average of the neighbouring 6 channels. The refined profiles are shown on the left hand side of figure 3.16.

The planned deconvolution of the spectra called for a method to normalize the measured intensity. A normalization is necessary, because every tungsten injection is slightly different, depending on plasma position, heating scheme, *etc.*. First attempts utilizing the total radiated power failed because of the aforementioned varying heating power and a dependence of the normalization factor on this quantity. The normalization factor demanded a quantity that was specifically tied to the radiation from tungsten. The best solution was found by considering the SPRED spectra. The spectra are always integrated along the same LOS and any changes to the W-intensity are clearly seen. A normalizing factor was defined from the integral over the wavelength interval $\lambda = [20, 25]$ nm giving the integrated intensity $\tilde{I} = \int_{\lambda_0}^{\lambda_1} I(\lambda) d\lambda$. The average of \tilde{I} was calculated on two time intervals, pre- and post-LBO. The normalizing factor was then calculated for each injection as $f_j = a/(\tilde{I}_{j,post} - \tilde{I}_{j,pre})$, with $a = 1/N \cdot \sum_{i=0}^N (\tilde{I}_{i,post} - \tilde{I}_{i,pre})$, N being the total number of tungsten ablations used for evaluation. The average of f_j is by definition 1.0 and the standard deviation is 0.2. The SPRED spectrometer then provided a useful normalization factor which made it possible to account for the slight differences of each laser ablation.

The most difficult and sensitive step was the assessment of the influence of contributions from higher order diffraction in the studied spectral range. Schwand has shown that for a flat-field GI spectrometer incident light with $\lambda < 6$ nm is still considerably diffracted in 4th and even 5th order [45]. It is known that tungsten in AUG plasmas radiates about 90% of its light in the quasicontinuum at $\lambda \approx 5$ nm [34]. Therefore, the higher order contributions can not be neglected in this evaluation. As for the normalization, the SPRED spectrometer provided the suitable reference measurement. Its sensitivity for $\lambda < 10$ nm decays rapidly and it is blind for light from the W-quasicontinuum at $\lambda = 5$ nm due to the strongly decreasing reflectivity of the grating. Intensity from $\lambda = 13$ nm which is diffracted into second order has been determined to be a factor of 27 lower than the first order intensity and can therefore be neglected for most plasma conditions.

For the investigation of the higher order influence on the GI spectra it should be recalled that the GI spectrometer is equipped with two MCPs. Each MCP can be moved along the Rowland circle independently to observe different spectral regions. One MCP is usually centered at the W-quasicontinuum at $\lambda = 5$ nm and used for tungsten concentration evaluation. The second MCP is free to observe other wavelengths. Discharges in which the LOS of GI and SPRED spectrometer are equal and the second MCP observes the same spectral region as the SPRED spectrometer allow for the determination of the higher order contribution to this spectral range. Figure 3.9 shows the discrepancy between the integrated intensities of GI and SPRED spectrometer at $\lambda = [20, 21]$ nm. It clearly depends on central temperature and is strongest for high T_e -values. In addition, this discrepancy is not only temperature dependent, but it also varies with wavelength. The case shown here is however the most extreme and for smaller wavelengths the effect is by a factor of 2 weaker.

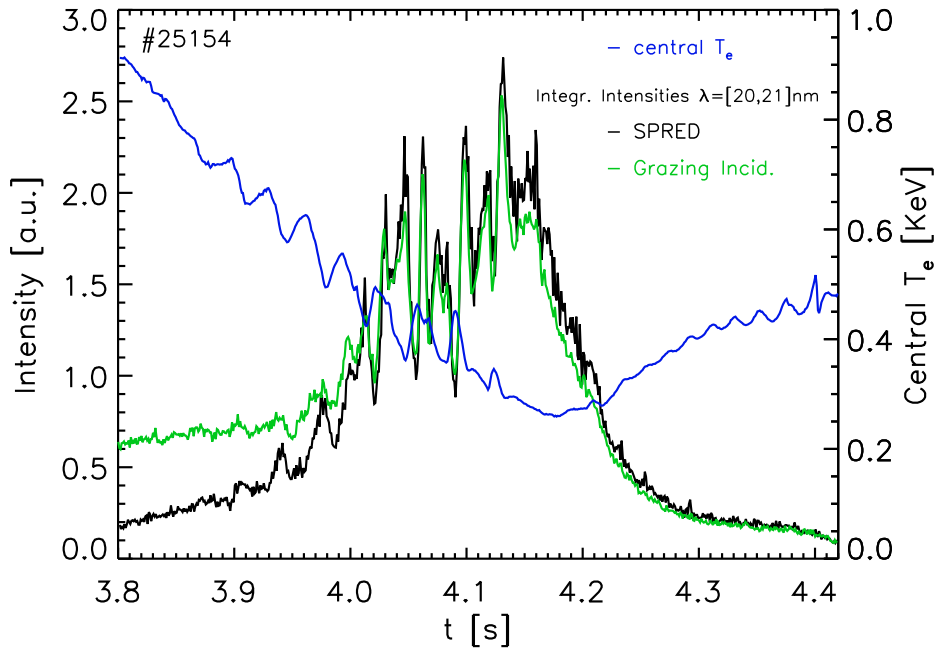


Figure 3.9: Comparison of spectral intensities as recorded by the SPRED and the GI at $\lambda = [20, 21]$ nm. Central T_e is plotted in blue.

The separation of the first order signal from the higher order intensity follows a regression ansatz. The linear regression model uses the intensities of the two GI-MCPs as independent variables and the intensity of the SPRED as dependent variable, *i.e.*

$$I_{SPRED,20} = I_{GI,20} \cdot k_0 - I_{GI,5} \cdot k_1, \quad (3.2)$$

k_i being the regression coefficients, $I_{GI,5}$ and $I_{GI,20}$ the intensities measured with the GI in the wavelength intervals at 5 nm and 20 nm. The assumption is that $I_{GI,20} = I_1 + I_{hi}$, with I_1 being the intensity in first order and I_{hi} the intensity from higher order diffraction, for this wavelength this means 4th order of the 5 nm W-quasicontinuum. It then follows that $I_{SPRED,20} = I_1 k_0$ and $I_{hi} = I_{GI,5} \cdot k_1 / k_0$. Finally the reconstruction of the first order intensity reads

$$I_1 = I_{GI,20} \cdot (1 - r_{hi}) \quad (3.3)$$

with $r_{hi} = (I_{GI,5} k_1) / (I_{GI,20} k_0)$ the ratio of higher order intensity to the total intensity measured at $\lambda = 20$ nm. The results of the regression and the first order intensity reconstruction are depicted in figure 3.10. The ratio of the two regression coefficients k_1/k_0 is a constant of the spectrometer. For the studied wavelength intervals it reaches values $0.02 < k_1/k_0 < 0.03$ and is therefore sufficiently small to not endanger the evaluation ansatz by introducing an high uncertainty into the correction factor r_{hi} . As aforementioned, the fit of k_1/k_0 was evaluated for a situation with approximately equal LOS for the GI and the SPRED spectrometer. It can be used to reconstruct first order intensities for discharges where the LOS are different.

The angle bisector drawn in red in Figure 3.10a depicts the ideal case for the regression result. The actual regression does not deviate very much from that ideal. This leads to the interpretation that the applied model fits the experiment and indeed most of the light not from first order is light

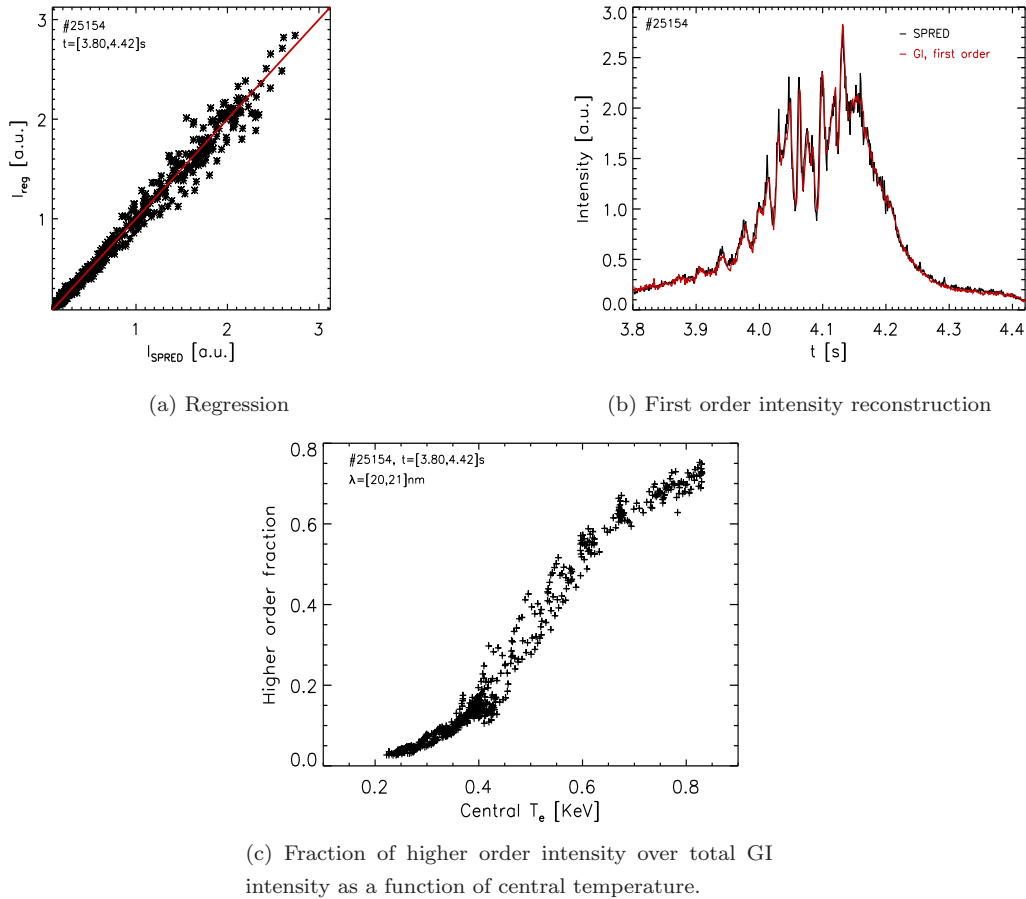


Figure 3.10: *Figure a)* shows the intensity obtained from the regression applied to the data of #25154 over the intensity of the SPRED spectrometer. In *figure b)* the final result of the first order reconstruction is printed in red. It should be noted how well it resembles the dynamics of the SPRED signal. *Figure c)* shows the intensity ratio as a function of the central T_e as observed with the GI spectrometer.

from fourth order emitted in the the 5 nm W-quascontinuum. Besides the fact that the regression resembles the bisector so well, also the reconstructed first order intensity for the GI in the wavelength interval $\lambda = [20, 21]$ nm allows for the conclusion that the regression was successful. The intensity of the GI spectra is, of course, multiplied by a constant in order to match the absolute values of the SPRED time trace. This has, however, no influence on the dynamic of the reconstructed GI signal. It resembles the SPRED signal closely and is shown in red in figure 3.10b.

The last step towards the successful evaluation of the GI spectra is the linkage of reconstructed first order intensity to the electron temperature. The factor r_{hi} presented before is the key to this link. The electron temperature used in this context is defined as the average temperature inside $\rho_{pol} \leq 0.6$ and its time trace was plotted in figure 3.9. Figure 3.10c shows the fraction of higher order intensity to total intensity as a function of central temperature. This fraction saturates to high as well as to low temperatures with a steep transition between the two regimes. At electron temperatures higher than 600 eV the studied wavelength interval is dominated by light from the 5 nm quascontinuum. Using the knowledge obtained in section 3.1 it is possible to explain the low flux of first order photons: The emitting shell for the first order light in this wavelength interval

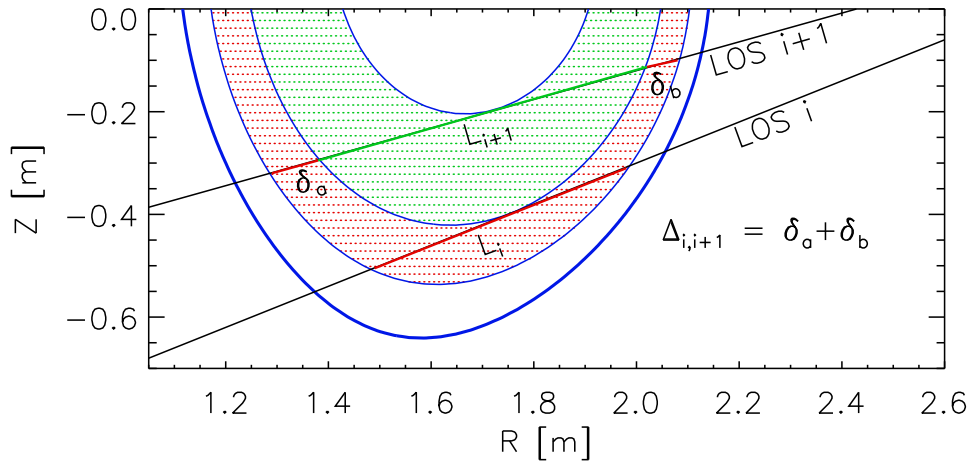


Figure 3.11: Schematic picture of the various segments used in the deconvolution

decreases with increasing temperature, while the intensity in the 5 nm regime grows. This leads to high order fractions of almost 80% for temperatures above 1 keV. Towards low temperatures the picture is reversed. The ionisation stages responsible for the quasicontinuum at 5 nm die out and at the same time the emitting shell for the first order light increases, reducing the fraction of higher order light to almost 0%.

This was the most extreme example for the influence of higher order light in the GI spectra. The temperature dependence of the higher order fraction was determined in the same way for three more wavelength intervals ($\lambda_1 = [14.5, 15.5]$ nm, $\lambda_2 = [16.0, 17.0]$ nm, $\lambda_3 = [18.0, 19.0]$ nm). However, the error induced by higher order diffraction is more modest in these wavelength intervals. Even for $T_e \approx 1$ keV the fraction of higher order intensity does not reach 50%. This is due to the strong first order light emission in these wavelength intervals. Furthermore, the temperature dependence is very similar for all three cases.

It is now possible to start the deconvolution process with the additional information framed in the paragraphs before. The deconvolution depends on the mapping of temperature profiles onto the LOS. A schematic view is shown in figure 3.11. The blue lines depict the borders of distinct temperature intervals for two adjacent LOS, while the shaded areas visualize the region of the characteristic temperature range for the two LOS. The characteristic temperature of LOS $i + 1$ is defined by two limits: $T_i^{max} \leq T_{i+1}^{char} < T_{i+1}^{max}$, where T_i is the electron temperature along LOS i . Each LOS i runs for a certain distance L_i inside its characteristic temperature T_i^{char} . The next LOS ($i + 1$) then runs through the characteristic temperature of LOS i , but for a shorter distance $\Delta_{i,i+1}$ (see figure 3.11) The measured intensity I_i along the different LOS can then be written in terms of emissivities E_i and distances $L_i, \Delta_{i,n}$:

$$\begin{aligned}
 I_1 &= E_1 \cdot L_1 \\
 I_2 &= E_1 \cdot \Delta_{1,2} + E_2 \cdot L_2 \\
 I_3 &= E_1 \cdot \Delta_{1,3} + E_2 \cdot \Delta_{2,3} + E_3 \cdot L_3 \\
 &\vdots
 \end{aligned}$$

After determining the L_i and $\Delta_{i,n}$ for all involved LOS, it is an easy step to perform the deconvolution on the measured intensities:

$$E_n = \frac{1}{L_n} \cdot \left(I_n - \sum_{i=0}^{n-1} E_i \cdot \Delta_{i,n} \right) \cdot (1 - r_n), \quad (3.4)$$

with $(1 - r_n)$ correcting the error from higher order diffraction. Equation 3.4 is recursive and this leads to an accumulation of the errors towards higher temperatures. The lowest temperature considered in the calculation of $\Delta_{i,n}$ and L_i is 40 eV. Figure 3.16 shows the emissivity of the deconvoluted intensities in red and of the non-deconvoluted ones in black. It should be mentioned that for the n th deconvoluted spectra L_n is the length running in its characteristic T_e -range, while for the non-deconvoluted spectra L_n corresponds to the full length of the LOS running at $T_e > 40$ eV. These 'raw' spectra are drawn in black. The advantage of using the tungsten injections facilitates the quantitative comparison of the contributions of the various temperature ranges to the final spectra. This is not possible with the accumulation approach, since the tungsten content is not controlled and not measureable at these low temperatures. The temperature dependence seen in the emissivities of the deconvoluted spectra confirm the qualitative findings of section 3.1. The emissivity peaks strongly for $270 < T_e < 400$ eV and falls off quickly for temperatures beyond 550 eV. The wavelength interval [21, 22] nm is dominated by light from tungsten at $250 < T_e < 500$ eV.

The advantage of the W-LBO method is obvious, when the deconvoluted emissivities shown in figure 3.16 (shown at the end of this chapter) are averaged over the studied wavelength interval ($\lambda_1 = [21, 22]$ nm) and plotted on a temperature grid: figure 3.12. Since this data was extracted from L-mode discharges it is legitimate to assume corona equilibrium for the fractional abundances of each ion stage and neglect effects of steep temperature gradients and transport. It is now possible to fit a simple model to the experimental data, assigning an weighting factor to each ionisation stage. This weighting factor is a primitive effective rate coefficient. It must be called primitive, since it has no temperature dependence. Equation 2.4 gives the emission rate for one certain emission line of one ionisation stage. Starting from this equation, the total emissivity of tungsten at a certain temperature can be written:

$$\epsilon_{tot}(T_e) = n_e n_W \cdot \sum_{z=0}^{74} f_z^c(T_e) \cdot X_{eff,z}, \quad (3.5)$$

where the coefficient $X_{eff,z}$ is the weighting factor of the simple model. It is assumed to have an gaussian shape centered at the dominating ionisation stage:

$$X_{eff,z} = e^{-\frac{(z-z_{max})^2}{\gamma^2}}, \quad (3.6)$$

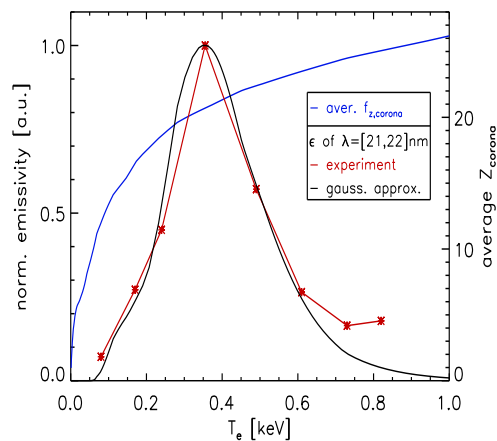


Figure 3.12: *Emissivity of W at $\lambda = [21, 22]$ nm as a function of electron temperature. Experimental data is plotted in red, emissivity from a simple model is plotted in black. The average ionisation stage $Z(T_e)$ in corona approximation is plotted in blue.*

with z_{max} and γ being the adjustable parameters. The temperature dependence is now solely carried by the coronal fractional abundances f_z^c . The results obtained with this model are reproducing the main part of the emissivity quite well. The by far most important ionisation stage is W^{21+} followed by W^{20+} and W^{22+} . In this model these three ionisation stages together already account for over 80% of the emissivity in this spectral range. However this model does not reproduce the low temperature dependence of the emissivity. A small correction to $X_{eff,z}$ has been applied to obtain better agreement with the experimental data at low temperatures: the values for $X_{eff,z}$ with $14 < z < 19$ have been raised to 4%-8% of the maximum value at z_{max} . The result of this model is plotted in figure 3.12 in black. The high discrepancy at temperature at $T_e > 700$ eV can be neglected easier, since for those two data points the errors are considerably higher than for the low temperature ones.

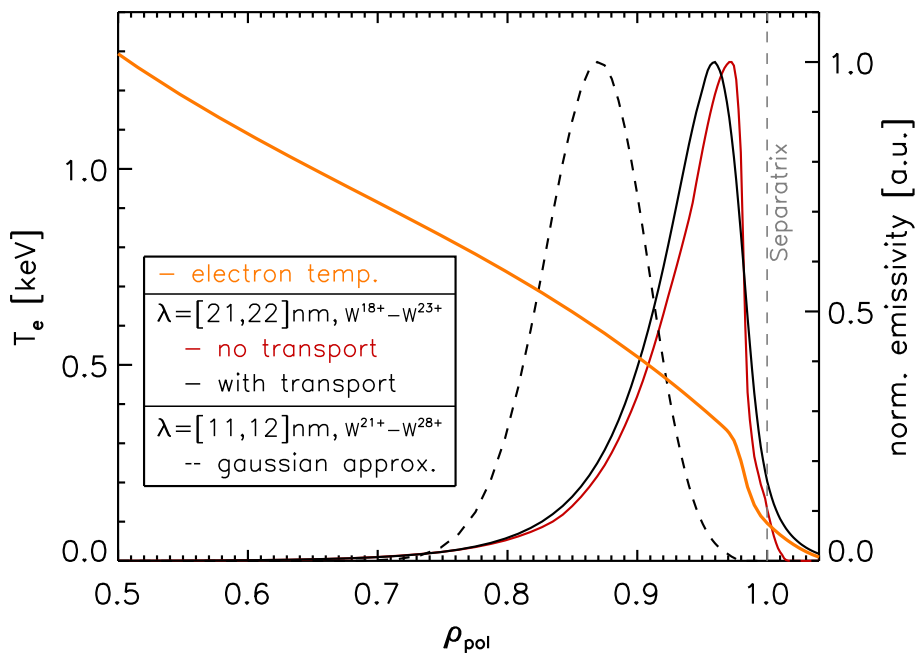


Figure 3.13: *Emitting plasma shells of spectral intervals $\lambda_1 = [21, 22]$ nm and $\lambda_2 = [11, 12]$ nm. Emissivities without transport are drawn in red. The shell of λ_2 (broken line) is an educated guess.*

The weighting factors determined from the corona equilibrium case allow for the calculation of an estimate for the radiating shell in the H-mode case. The emissivity in the H-mode case is calculated by exchanging in equation 3.5 the fractional abundances in coronal equilibrium with the fractional abundances obtained from transport calculations. Furthermore the density is not taken radially constant any more as for the coronal equilibrium case, but exhibits a steep gradient at the ETB. This emissivity obtained in this way is then plotted on the radial grid used in the transport calculations. The result of such a mapping is shown in figure 3.13 and is plotted in black. The radial grid is taken from #25658 ($t = [2.0, 2.7]$ s) and the position was mapped via the electron temperature shown in orange. The emitting shell plotted in red represents the case of coronal equilibrium fractional abundances and neglects transport effects. A comparison with the case including transport (in black) shows a slight shift inwards which is mainly due to the density gradient at the plasma edge.

The emissivity from experimental data for the lower wavelength intervals could not be calcu-

lated due to technical difficulties which will be explained in the next paragraph. Therefore, the second emitting shell in figure 3.13 is an educated guess, extrapolating knowledge obtained from the outer radiating shell. The first extrapolated information is, that in corona equilibrium the peak of emissivity of the outer shell coincides with the peak of the distribution of the contributing tungsten ionisation stages when plotted versus temperature. The contributing ionisation stages for $\lambda_1 = [21, 22]$ nm were determined already in equation 3.1, and are defined by the averaged fractional abundances in the temperature range of the emission. The radial distribution of the contributing tungsten is calculated as follows:

$$W_{contr}(r) = \sum_{i=0}^{74} f_{av,i} \cdot f_i(r) \quad (3.7)$$

The temperature range for the wavelength interval $\lambda_2 = [11, 12]$ nm is $450 < T_e < 1100$ eV. The upper temperature boundary is set by the emission characteristic of $W^{30+} - W^{33+}$ which radiates mainly at T_e around 1.1 keV and the lower boundary is extracted from the series of spectra shown in 3.3. For this temperature range the difference between fractional abundances from coronal equilibrium and transport calculations are almost nonexistent (see figure 3.4). Therefore the small shift found for the outer shell when going from corona to transport will not occur in this temperature interval. In this case, the distribution of the contributing ionisation stages has a maximum at 650 eV. This sets the center position of the gaussian. The width is then adjusted in such a way that the right wing of the normalized emissivity reaches half maximum at the same radial position where the left wing of the emissivity of λ_1 also reaches half maximum. This is justified since the time trace of λ_2 shows no ELM disturbances, while the one from λ_1 does. In section 5.2 it will be shown, that this guess is quite accurate after all. Using the gaussian approximation of the weighting factors the contributing ionisation stages were reevaluated. The outer shell (λ_1) is restricted to $W^{18+} - W^{23+}$ with small contributions from lower ionisation stages. The inner shell (λ_2) is emitted by $W^{21+} - W^{28+}$, after applying the gaussian shape for the weighting factors.

During the dedicated experiments both MCPs at the GI spectrometer were used to observe the spectral interval [13.8, 25.5] nm. Since each MCP detects only an interval of ≈ 4 nm, the MCP position had to be changed and the discharges had to be repeated with varying MCP positions. The lower two intervals, $\lambda_1 = [13.8, 17.8]$ nm and $\lambda_2 = [16.7, 21.0]$ nm were therefore studied with the MCP usually used for the tungsten concentration evaluation. In the analysis process it became clear that this MCP is no longer suitable for the investigations presented here. It suffers from an area of reduced sensitivity at the location where the W-quasicontinuum is usually positioned on the MCP. An experimental setup to quantify the damage was designed. It comprised the use of a He-glow discharge started in the spectrometer duct and a scan of the MCP with the light of the He^{1+} transition at $\lambda = 30.38$ nm. The weak light source, however, required a very long exposure setting (4s) at the camera. Spectra recorded with this setting were absolutely dominated by dark currents in parts of the MCP and were impossible to evaluate. The lack of a stronger steady light source, with which the exposure time and the influence of dark currents could have been reduced, terminated this investigation. The spectra obtained with this setup showed that about 20% of the MCP surface are affected strongly and about 30% weakly by dark currents. This damage might also have lead to the observed degradation of spectral resolution for this MCP. With these remarks in mind, figures 3.17 and 3.18 are only shown for the sake of completeness. It should be mentioned, that the MCP is still suitable for the W-concentration measurements, since the MCP signal is cross

calibrated with the bolometer data during each experimental campaign and the evaluation process does not rely on high spectral resolution.

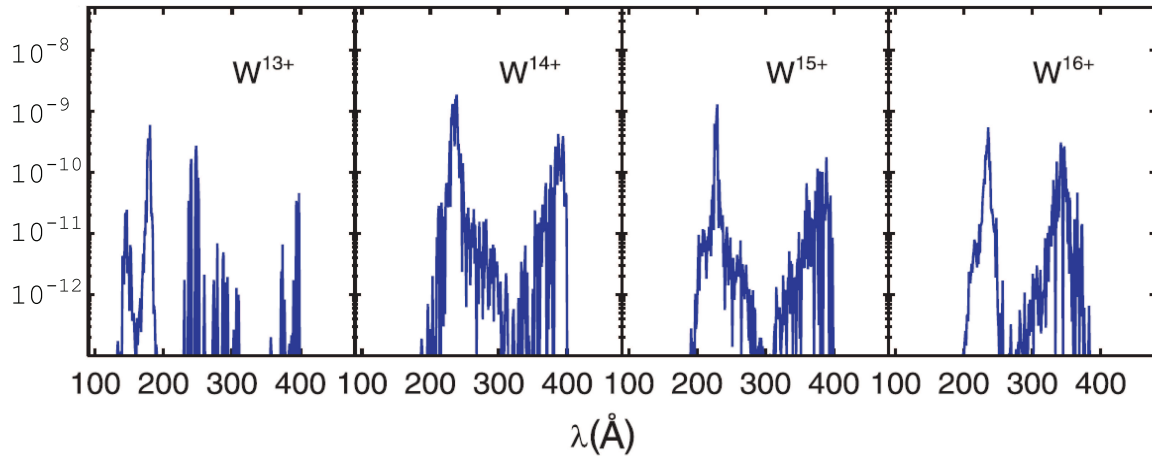


Figure 3.14: f -PEC of $W^{13+} - W^{16+}$ for plasma conditions as expected in the ITER divertor or edge plasma, $T_e = 50$ eV and $n_e = 10^{18} \text{ m}^{-3}$, taken from reference [41]

3.3 Comparison with other experiments and calculations

The radiation from highly ionised tungsten is a research topic since the late 1970s. There are numerous studies on the VUV-spectra of tungsten at ionisation stages W^{30+} and above [35, 46–49]. However, all these studies only consider the very powerful radiation window at $\lambda \approx 5$ nm. On the other hand the low ionisation stages (W^{16+} and below) have also gained some attention recently [41, 50–52]. The spectra of the ionisation stages between W^{16+} and W^{30+} in the wavelength interval $\lambda = [10, 25]$ nm have only been studied by few authors [40, 53]. The reason for this is the vast amount of calculation time needed to obtain synthetic spectra from the ionisation stages around W^{20+} . This high demand of computational power is the result of the open 4f shell of these ionisation stages. The number of electrons in this shell leads to a large number of transition possibilities which drive computational time to unfeasible values, if a useful spectral accuracy is demanded. In addition, previous experiments on tungsten at low T_e undertaken at AUG suffered from lower spectral resolution and slower cameras. Furthermore, they focused on temperatures around 1 keV and did not reach the low temperatures presented in this work.

Experiments on this topic performed at the Electron Beam Ion Trap (EBIT) in Berlin investigated the spectral range $\lambda = [13.2, 17.2]$ nm. During these experiments the electron beam energy was scanned from $329 < E_b < 951$ eV which translates to the maximum ionisation stages W^{15+} to W^{28+} . The recorded spectra show several intense line transitions which exhibit a strong beam energy dependence. Since the temperature range evaluated in the present work encloses the beam energies applied in the EBIT experiments, it was expected to identify the lines also in the AUG spectra. Indeed, two transitions at $\lambda_1 = 14.81$ nm and $\lambda_2 = 14.99$ nm appeared in the AUG spectra which coincided with the wavelength of two transitions found in the EBIT spectra. In the EBIT spectra these transitions originated from W^{25+} for λ_1 and W^{15+} for λ_2 . Since this light was emitted at very different beam energies, ≈ 800 eV and ≈ 400 eV respectively, a significant temperature dependence

of the line intensity should be visible in the AUG plasma. However, a thorough investigation of the temperature dependence of the AUG line intensities revealed a behaviour that does not match the ionisation stages identified from the EBIT data and it must be concluded, that the lines in the AUG spectra must have an origin other than tungsten. Furthermore, identification of the EBIT transitions from the SPRED spectra is impeded by the rather poor spectral resolution of the spectrometer. Many lines found in EBIT spectra are too close together to be resolved with the SPRED spectrometer and blend into the quasicontinuum. Looking at figure 3.3 only one transition at 15.00 nm is clearly visible. The transition at 13.28 nm coming up at the highest temperature is already the very powerful line from W^{44+} .

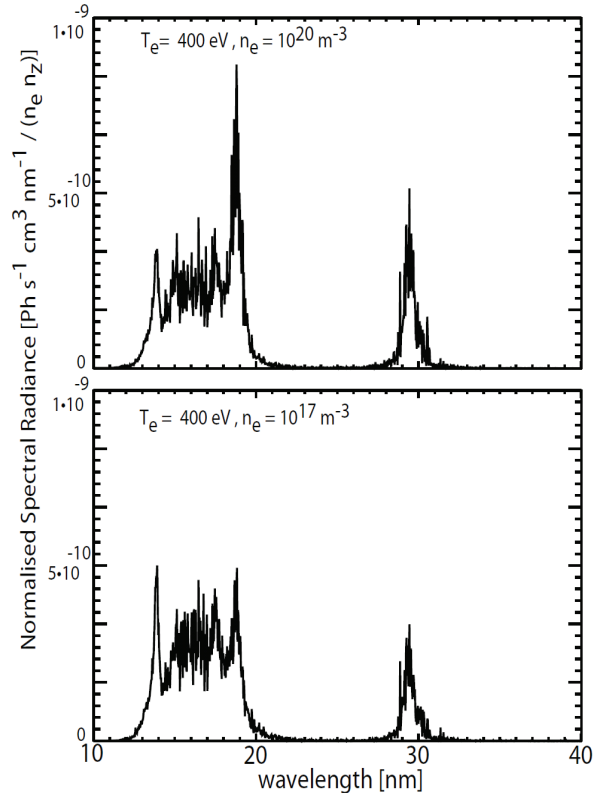


Figure 3.15: *Modelled spectrum for W^{23+} at two densities, 10^{17} and 10^{20} m^{-3} . Taken from reference [54]*

In the calculations performed by Peacock [41] the feature Photon Emissivity Coefficients (f-PEC) from W^{5+} up to W^{16+} in the spectral interval $\lambda = [10, 50] \text{ nm}$ were determined. The plasma conditions applied in their calculations mimic the values expected for plasmas in the ITER divertor or edge, $T_e = 50 \text{ eV}$ and $n_e = 10^{18} \text{ m}^{-3}$. Since the contributions from radiating shells of ionisation stages W^{12+} and below are negligible in AUG plasmas, only the findings for the remaining stages will be regarded. Their results are shown in figure 3.14. Even though the plasma parameters are not the same as in the discharges evaluated in section 3.1 the trend for a strong radiation peak at $\lambda \approx 22 \text{ nm}$ is obvious. This peak coincides rather well with the peak in intensity found in the spectrum at lowest temperature presented in figure 3.3. Under these plasma conditions the ionisation stages $W^{13+} - W^{16+}$ have a rather broad radiating shell and their contribution to the spectrum is most likely significant. Therefore there is good agreement between experiment and calculation for at least

the lowest temperatures observed in AUG.

The latest calculation efforts by Pütterich *et. al.* [54] tackled the radiative features of W^{23+} at electron temperatures below 1 keV. Their results for the wavelength range 10 – 40 nm are given in figure 3.15. With the plasma conditions applied during their calculations, the radiative contribution of this ionization stage to the radiation in the spectral range $\lambda = [21, 22]$ nm should be negligible. This finding agrees quite well with the results of this work. Figure 3.12 shows how the emissivity in this spectral range is dominated by radiation from ionization stages around W^{20+} with a steep drop of the contribution for higher ionisation stages. For a plasma where the average ionization stage of tungsten is W^{23+} , the contribution to the aforementioned spectral range is rather low as can be seen in the figure. Furthermore, the calculations manage to reproduce a radiative feature at $\lambda = 19$ nm seen in figure 3.3 (4th plot from top) and give a good qualitative agreement with the VUV spectrum measured in a plasma which is mainly at a electron temperature of 400 eV.

The result of this experimental investigation gives new insight on the temperature dependence of tungsten radiation in the VUV at temperatures $T_e < 1$ keV. Two distinct spectral ranges $\lambda_1 = [21, 22]$ nm and $\lambda_2 = [11, 12]$ nm have been identified. From W-injection experiments the temperature dependence of the emissivity in spectral range λ_1 was evaluated. This made it possible to determine the position and shape of the radiating shell for λ_1 in a H-mode plasma (see figure 3.13). This spectral range is emitted from tungsten at temperatures $100 < T_e < 500$ eV peaking at $T_e \approx 360$ eV. The contributing ionisation stages are $W^{18+} - W^{23+}$. The second spectral range (λ_2) could not be evaluated in such detail due to technical difficulties. The temperature range from which the spectra originate was restricted to $450 < T_e < 1100$. However, an educated guess on the position and the shape of the emissivity distribution allowed for the reduction the width of the distribution and delivered a central temperature of $T_e = 650$ eV for the peak of the emissivity. The ionisation stages $W^{21+} - W^{28+}$ were linked to this spectral and temperature range.

The next pages display the deconvolutions of the GI spectra obtained from the dedicated tungsten injection experiments described in section 3.2.

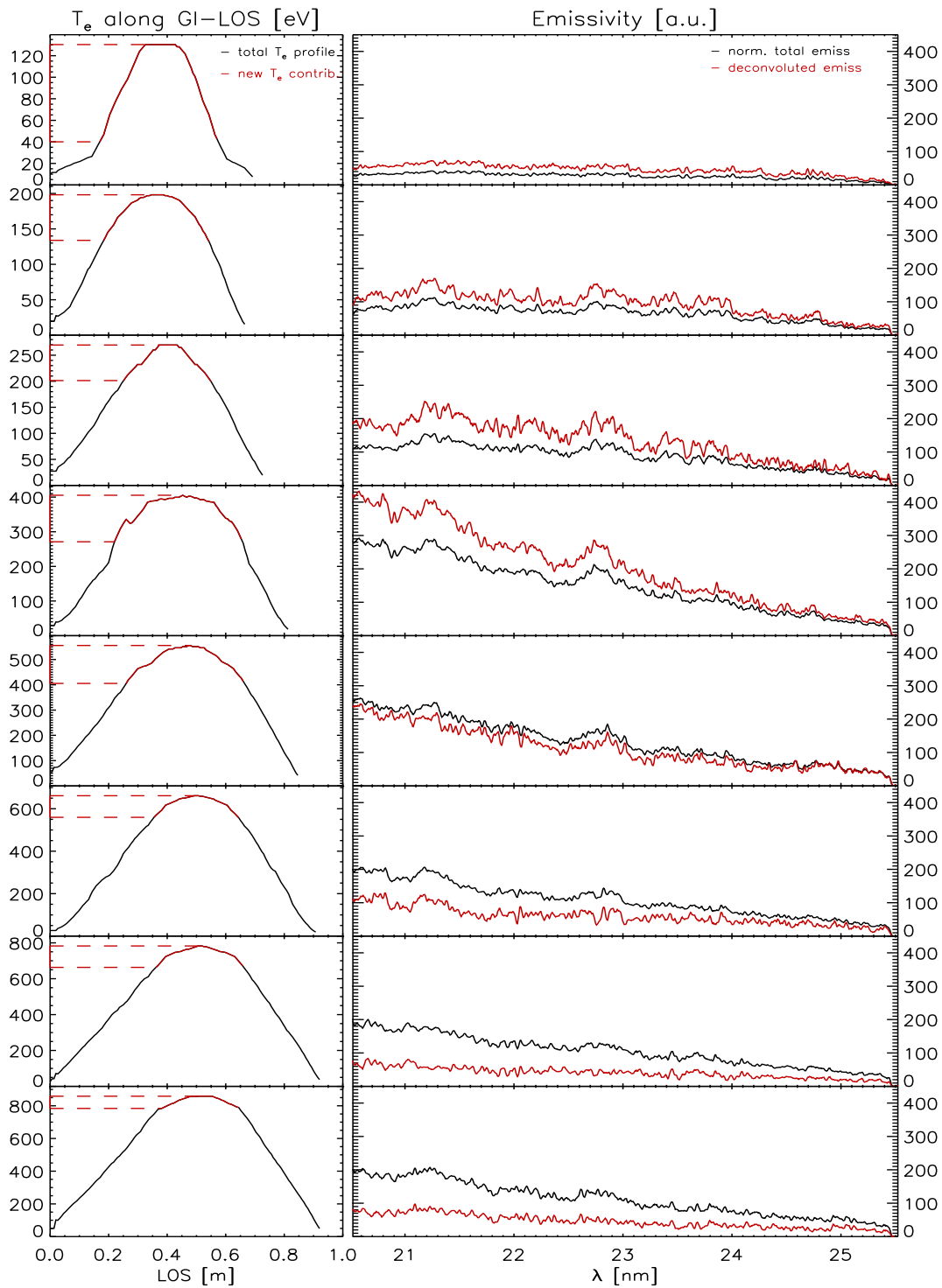


Figure 3.16: The right set of plots are W-spectra at different electron temperatures (GI spectrometer) and the corresponding T_e -profiles along the LOS are shown in the left set of plots. The spectra in black are normalized, but not further processed. The red spectra are the emissivities obtained from the deconvolution. The red sections in the T_e -profiles represent the temperature range in which the deconvoluted emission originates.

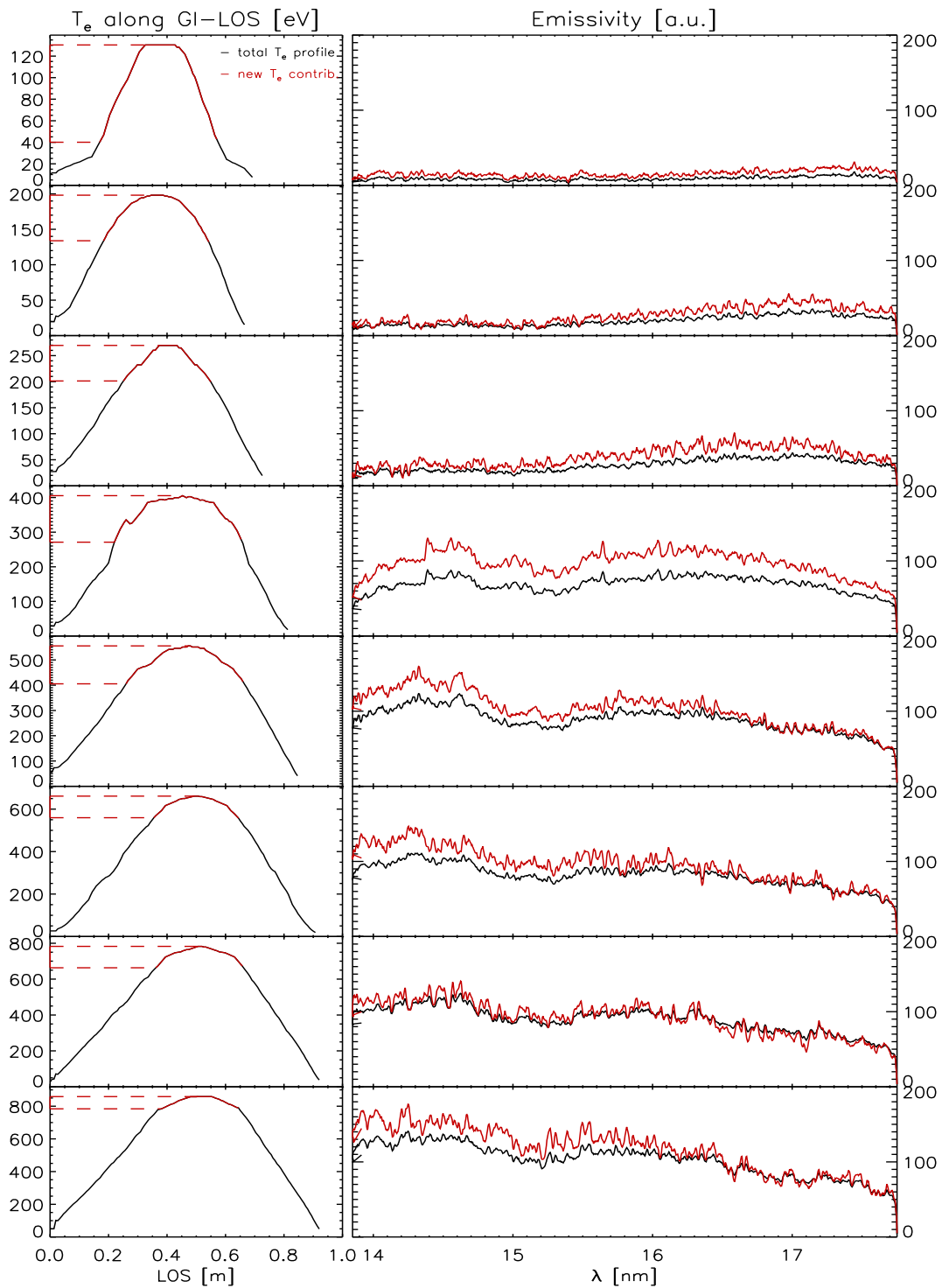


Figure 3.17: The right set of plots are W-spectra at different electron temperatures (GI spectrometer) and corresponding T_e -profiles. The MCP used for this measurement usually observes the W-quasicontinuum at 5 nm. This has clearly reduced the sensitivity locally around 15.1 nm

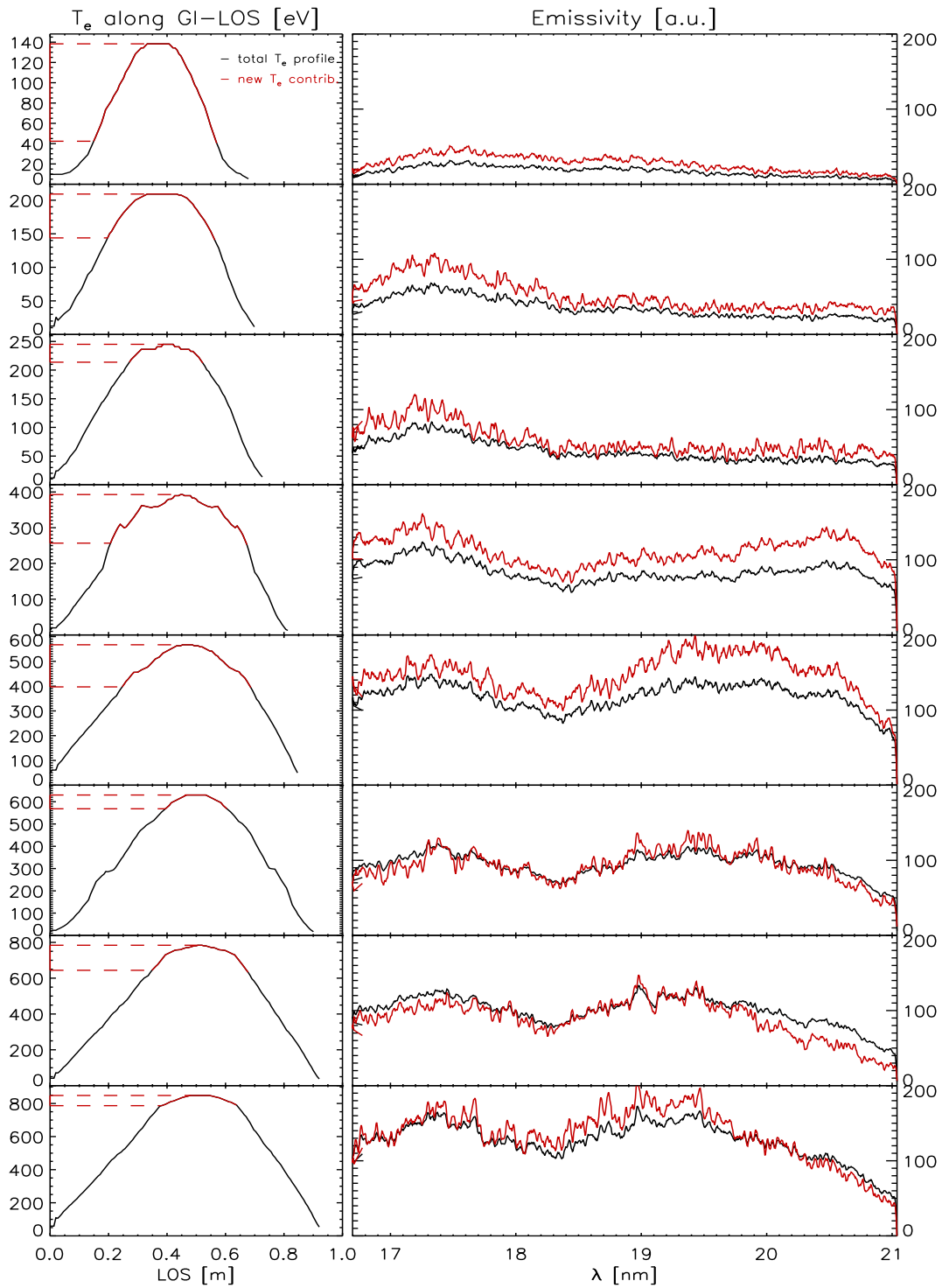


Figure 3.18: These spectra are measured with the same MCP as was used in figure 3.17. They suffer from the same reduced sensitivity. In this setup it is located at 18.2 nm.

Chapter 4

Probing of W-transport with a Modulated W-source

4.1 Using ICRH for the W-erosion modulation

Investigations on impurity transport in the H-mode ETB are usually performed with the charge exchange recombination spectroscopy (CXRS) system installed at AUG. This system provides the spatial (> 3 mm) as well as temporal (> 1.9 ms) resolution necessary to obtain impurity density profiles in the ETB. In combination with transport modelling these profiles allow for the determination of the transport parameters of the observed impurity [17]. This approach is very well suitable for light impurities, since a significant fraction is fully stripped of electrons even in the ETB (*e.g.* He, C, Ne) or are at least ionized to a He-like state (Ar). The database for the charge exchange and emissivity coefficients of these ions is accurate enough to deduct impurity densities from the measured line intensities. However, this method of transport investigation is not applicable to tungsten. There are two reasons responsible for this. First, tungsten radiates mainly in the VUV spectral range, as was shown in the previous chapter. This renders the use of visible spectroscopy impossible and one has to resort to VUV spectroscopy. VUV spectroscopy, however, can not provide the necessary spatial resolution to resolve the tungsten density gradient in the ETB. Second, the atomic data, especially of the emissivity coefficients of the interesting ionisation stages around W^{20+} is still not available with a high enough accuracy to compare experimentally obtained spectroscopic data to the synthetic one. A different method to probe the tungsten transport in the plasma edge had to be found.

In the case that impurity density profiles are unobtainable the transport can be probed by the application of a modulated impurity source. The modulation can be implemented as a short, delta like pulse or as a continuous, harmonic variation. The latter is an ansatz that has already been successfully used in previous experiments for lighter impurities [55]. The delta like impurity source is generated either by the injection of the impurity into the plasma via laser ablation or a short impurity gas puff. If the impurity propagation into the plasma of such a source is monitored at multiple plasma radii, the drift velocity as well as the diffusion coefficient of the impurity can be determined [11]. Recently the argon transport at radii $\rho_{pol} < 0.6$ has been studied by use of this method [56]. For tungsten, the delta like impurity source would be created by laser ablation. However, this injection technique accelerates the tungsten atoms to radial velocities $v_r \approx 1100$ m/s. With a fast camera system (frame rate 20 kHz) the time between ablation and crossing of separatrix

was observed to be $\approx 50 \mu\text{s}$ for the fastest tungsten atoms and $\approx 200 \mu\text{s}$ for the bulk of the accelerated tungsten. These time scales are still about three orders of magnitude larger than the time needed to ionize the tungsten atoms under SOL plasma conditions. Nevertheless, the camera images show that the tungsten particles cross the SOL as a narrow beam and are not deflected by the magnetic field which means that a large fraction of the ablated tungsten crosses the SOL as neutral particles. This leads to a very different transport behaviour, as compared to tungsten that is eroded from the PFCs and renders the tungsten injection technique useless for the investigation of edge transport.

The appropriate tungsten source was found in the ICRH antennae limiters. It was observed that the tungsten concentration in the main plasma increases, if ICRH power is coupled into the plasma. This issue was studied among others in [25] and [27]. It was shown that the increase of tungsten content is due to an increased erosion flux at the antennae limiters. The measurement of the tungsten erosion at the limiter structures was performed with the spectroscopic system described in section 2.1. The enhanced erosion is most probably due to an additional sheath potential $\Delta\Phi_{rf}$ induced in the limiter structure when the ICRH is switched on [25]. Due to the increased potential the ions impinging onto the PFC are accelerated and the sputtering of tungsten by these ions increases. However, the increased sputtering can not be explained by a clean deuterium plasma, but needs

a fraction of heavier and higher charged ions. In [25] a fraction of 1% C^{4+} was assumed as a substitute for all other light impurities usually present in the plasma. With this assumption the effective erosion yield $Y_{W,eff} = \Gamma_W/\Gamma_H$ is only weakly dependent on the edge temperature. The difference of the sputtering yield ΔY_{rf} between phases with and without ICRH can be used to determine the additional sheath potential $\Delta\Phi_{rf}$. The dependence of ΔY_{rf} on $\Delta\Phi_{rf}$ is roughly $\Delta Y_{rf} = 10^5 \cdot \Delta\Phi_{rf}$, for $1 < \Delta\Phi_{rf} < 1000V$. Figure 4.1 shows ΔY_{rf} and $\Delta\Phi_{rf}$ as functions of P_{ICRH}/Γ_H . This dependence was chosen due to the influence of the deuterium flux on the sheath potential. What is more important in the framework of this study is the approximately linear relation between applied ICRH power and the additional tungsten erosion flux $\Delta\Gamma_W = \Delta Y_{rf} \cdot \Gamma_H$, visible in the data set presented in figure 4.1. This linear dependence was also found in [57]. With this information it was possible to use the ICRH system to create a well controllable tungsten source.

The ICRH system allows to change the applied power on a time scale of 4 ms. This time constant is sufficiently small for the mode of tungsten erosion modulation envisaged in this study. The power was modulated sinusoidally with the total amplitude $A_P = 1.3 \text{ MW}$ and a modulation frequency of $f_P = 10 \text{ Hz}$ for most of the experiments carried out in this study. As an example of the applicability of this modulation technique some time traces of #25658 on the interval $t = [2.1, 2.7] \text{ s}$ are shown in figure 4.2. The power by ECRH, NBI and ohmic heating was about 8 MW. The total erosion rate at the ICRH limiters, shown in the middle plot, exhibits a sinusoidal modulation, as was expected

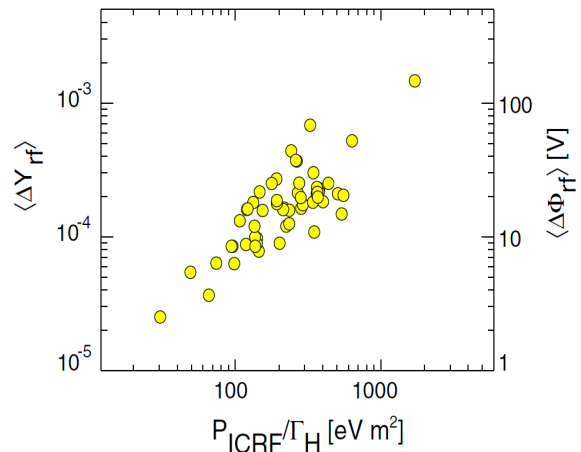


Figure 4.1: Mean tungsten erosion yields and estimated additional sheath potential due to applied ICRH power. The ratio of P_{ICRH}/Γ_H was chosen for the x-axis due to the effect of Γ_H on $\Delta\Phi_{rf}$. Taken from reference [25]

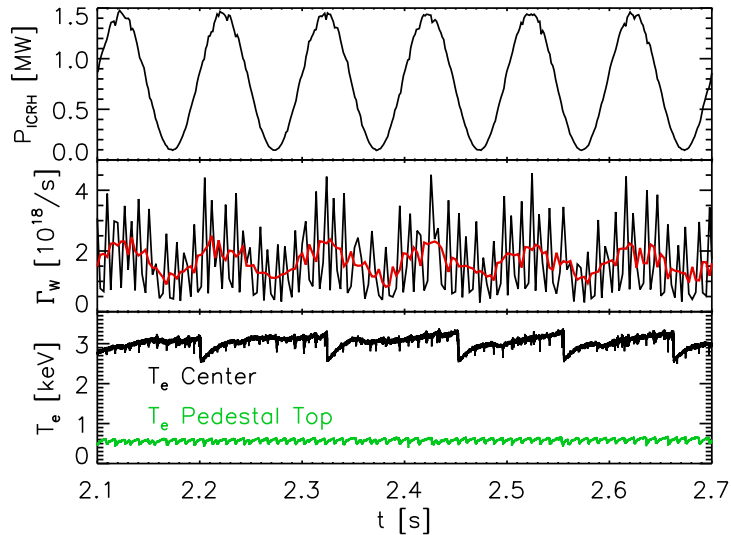


Figure 4.2: ICRH power modulation (top plot), its influence on the total W-erosion rate at the ICRH limiters (middle plot), and its impact on electron temperature (lowest plot). The “noisy” W-erosion rate signal is due to ELMs, and the red line is a 4point smooth.

from the above considerations. The rather “noisy” signal is due to the increased erosion rate during ELMs. The original time trace, recorded with a framing time of 3.4 ms, was smoothed with a 4 point boxcar average to better visualize the impact of the ICRH power on the erosion rate. The resulting time trace is plotted in red. It exhibits a very clear dependence on applied ICRH power, where the erosion rate varies by a factor of 2 between lowest and highest ICRH power. Furthermore, the linear dependence of the erosion rate on the ICRH power was confirmed during these investigations. This mode of probing the tungsten transport requires constant background plasma conditions over several modulation periods. In this context the lowest plot of figure 4.2 shows the electron temperature at the plasma center and at the pedestal top. Both time traces exhibit a periodic behaviour, but one is caused by sawteeth (central T_e), the other by ELMs (pedestal top T_e) and none by the 10 Hz ICRH power modulation. Also the electron density shows no variation that can be related to the modulated ICRH power. Therefore, it is justifiable to regard the injected ICRH power as a trace heating and the only effect that the ICRH has on the plasma is the periodic increase of the tungsten erosion rate.

4.2 Experimental Setup, Decoupling of Gas Puff and ELM frequency

The original focus of the investigations was aiming at the determination of the transport processes for tungsten in the ETB. Therefore, all experiments performed in the framework of the W-transport probing were run in lower single null H-mode. The plasma current was 1 MA. The ICRH power was modulated as described in the previous section to provide the modulated tungsten source. In order to keep the contribution of the ICRH heating on a relative low level, three NBI sources deployed a total of 7.5 MW heating power. The ECRH system delivered 0.8 MW and was set to central heating to avoid central tungsten accumulation. The toroidal magnetic field was set to -2.5 T.

The distance ΔR between separatrix and ICRH limiter in the midplane on the low field side was kept constant, since it is known from previous experiments, that ΔR has a major influence on the tungsten concentration in the core plasma. These are the parameters that were identical for all experiments that will be presented in this chapter.

Based on the experience from previous experiments [14, 19] the deuterium gas puffing rate in the main chamber and the upper triangularity were chosen to probe their influence on the tungsten edge transport. The motivation to vary these two parameters will be laid out curtly. In the experiments performed in [14] the deuterium gas puffing rate was used to control the ELM frequency. Those experiments were run at constant triangularity (upper triangularity $\delta_u = 0.12$, average triangularity $\delta = 0.26$). With the change of ELM frequency the tungsten concentration in the main plasma changed, leading to an inverse relation between tungsten concentration and ELM frequency. The results from those experiments were interpreted as a manifestation of the impurity flushing effect by ELMs which has already been observed for carbon in DIII-D [18]. Furthermore, the impurity flushing effect by ELMs is thought to be of high importance for the control of the impurity content of the plasma. Therefore, it was natural to choose the gas puffing as one mechanism to control the ELM frequency and observe its possible impact on the edge transport. It was also of interest to decouple the effects of gas puff and ELM frequency to be able to assess the effect of the ELMs themselves on the impurity behaviour. The decoupling was achieved by the variation of the upper triangularity, a method which was not available due to technical difficulties during the time the experiments in [14] were performed. Earlier studies showed, that for a lower single null plasma configuration the increase of the upper triangularity leads to a decrease of ELM frequency [19]. This relation was successfully applied in the present experiments to control the ELM frequency over a wide range. The upper triangularity was varied in the range $0.08 < \delta_u < 0.23$ (low to medium average triangularity) which resulted in ELM frequencies $25 < \nu_{ELM} < 110$ Hz. At the same time the variation of triangularity led to a change in electron density, an effect on the order of $\approx 10\%$ for the triangularity regime explored during these experiments. The deuterium gas puffing rate, on the other hand which spanned the range $0.4 < \Phi_D < 2.0 \cdot 10^{22}/s$ only had a detectable influence on the ELM frequency in one set of discharges, while no effect was observed in another set. Additionally, it showed only a very limited fuelling effect in the flat top phase. At similar triangularity, the strongest observed increase of central n_e was 7%, with Φ_D increasing from $1.0 \cdot 10^{22}/s$ to $2.0 \cdot 10^{22}/s$. The density at the pedestal top varied between $5.0 < n_{e,ped} < 6.6 \cdot 10^{19} m^{-3}$ which relates to the Greenwald density as $0.58 < n_{e,ped}/n_{e,GW} < 0.76$. The energy contained in the plasma (W_{mhd}) is nearly identical when comparing discharges in the phase of low or medium upper triangularity but shows some variation in the case of high upper triangularity. At high upper triangularity it is found that the higher gas puffing leads to lower plasma stored energy. However, the difference in W_{mhd} is still small: at $\Phi_D = 1.0 \cdot 10^{22}/s$: $W_{mhd} = 0.63$ MJ, at $\Phi_D = 2.0 \cdot 10^{22}/s$: $W_{mhd} = 0.59$ MJ. When looking at the behavior of W_{mhd} at constant gas puffing ($\Phi_D = 1.0 \cdot 10^{22}/s$) but varying triangularity a continuous increase of W_{mhd} with triangularity can be observed: at $\delta_u = 0.08$: $W_{mhd} = 0.58$ MJ, $\delta_u = 0.11$: $W_{mhd} = 0.60$ MJ, $\delta_u = 0.17$: $W_{mhd} = 0.63$ MJ.

Each discharge has 3 stages, each with a duration of at least 0.7 s during which the plasma conditions are kept constant. This allows for the observation of minimum 7 periods of the modulated tungsten source for each stage with the various combinations of gas puffing rate and triangularity. Besides the tungsten source at the ICRH limiters, also the tungsten erosion at the outboard divertor was monitored. The tungsten source at the inner heat shield on the inner column was not measured,

since from the 3 tungsten sources, ICRH limiters, heat shield on inner column and outboard divertor, this source has the weakest influence on the tungsten content of the core plasma [14].

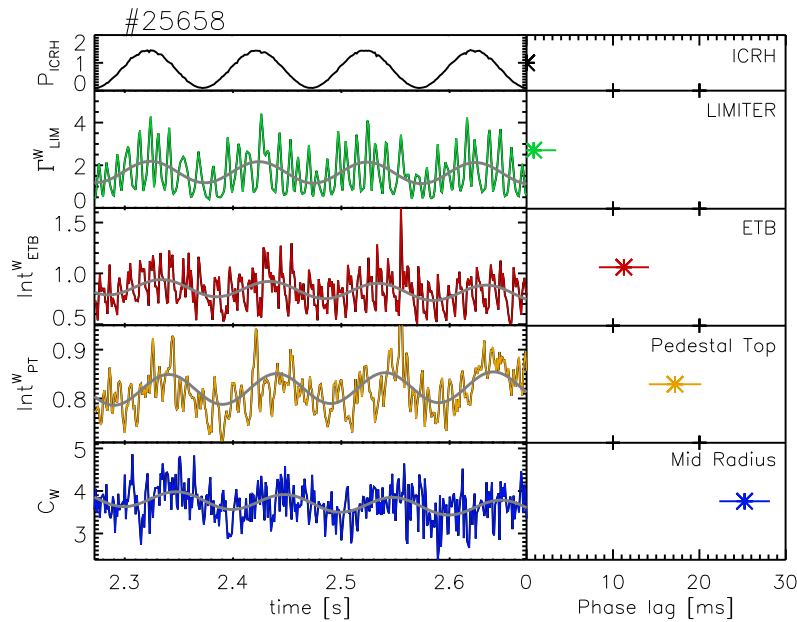


Figure 4.3: Observation of the inward propagating tungsten wave. The top plot shows the applied ICRH power [MW], while the following plots depict the observed tungsten signals, starting at the erosion site (ICRH limiters) and tracking the wave up to about mid radius. The gray sinusoidal line is a fit to the data. The plots on the right show the phase lag obtained from the fit.

While propagating into the plasma, the tungsten wave is observed with the SPRED and the GI spectrometers. These spectrometers deliver the phase in the ETB ($T_e \approx 350$ eV), at the pedestal top ($T_e \approx 650$ eV) and at about mid-radius ($T_e \approx 1000$ eV). It should be noted, that the determination of the observation position depends on the temperature profile and the observation locations will shift with a changing temperature profile. The central tungsten concentration is also evaluated from the GI spectra, however, it was found that the modulation of the tungsten concentration is attenuated below the detection limit this far into the plasma. The amplitude of the tungsten wave is determined at mid-radius as a change in concentration, while the observation points further out provide the amplitude in terms of the intensity of the tungsten radiation. The resulting tungsten signals at the various radial positions and the phase lag at each of these positions are depicted exemplary in figure 4.3.

4.3 STRAHL Predictions

The observation of the phase lag and impurity amplitude with such a rough spatial resolution does not allow for the application of an analytic solution to obtain information on the transport parameters. Therefore, such an investigation has to resort to a modeling ansatz. The modeling was performed once neglecting ELMs and once including a rough ELM model to mimic the effect of ELMs on erosion and particle exhaust from the main plasma. The following section will deal with the former case.

4.3.1 ELM-free Transport Calculations

The transport model used in this work is the 1-D transport code STRAHL. This code solves the radial transport equation for each ionisation stage using an ansatz that combines diffusive and convective transport processes. The radial transport equation for the impurity I with ionisation stage Z is derived from the continuity equation:

$$\frac{\partial n_{I,Z}}{\partial t} = -\nabla \vec{\Gamma}_{I,Z} + Q_{I,Z}, \quad (4.1)$$

where $\vec{\Gamma}_{I,Z}$ is the particle flux density of the impurity and $Q_{I,Z}$ are the sources and sinks of the specific ionisation stage due to ionisation, recombination and charge exchange processes. The term $Q_{I,Z}$ connects only the neighbouring ionisation stages. The radial flux density $\Gamma_{I,Z}^r$ is expressed in terms of a diffusive and a convective term:

$$\Gamma_{I,Z}^r = -D \cdot \frac{\partial n_{I,Z}}{\partial r} + v \cdot n_{I,Z}, \quad (4.2)$$

with D and v the flux surface averaged diffusion and convection coefficients. In the case of classical and neoclassical transport the flux average of the transport coefficients can be calculated for each ion species separately [58]. For anomalous transport the coefficients are assumed to change weakly with Z such that at one radius, where only a few charge stages exist, they can be taken as independent on Z . In cylindrical coordinates the radial transport equation then reads:

$$\frac{\partial n_{I,Z}}{\partial t} = \frac{1}{r} \frac{\partial}{\partial r} r \left(D \cdot \frac{\partial n_{I,Z}}{\partial r} - v \cdot n_{I,Z} \right) + Q_{I,Z}. \quad (4.3)$$

This equation applies to the volume inside the last closed flux surface (LCFS) and is part of a set of Z coupled differential equations [59]. Outside the LCFS the assumption of constant $n_{I,Z}$ on the flux surface does no longer hold and a different treatment of the impurity in this plasma volume is necessary. For this reason the code allows the implementation of a parallel loss as a volumetric loss term $-n_I/\tau_{\parallel}$ depending on a characteristic parallel loss time. This is a rough simulation of the parallel transport processes and impurity losses in the SOL. The transport calculations are performed on predefined temperature and density profiles. The code also takes into account the difference in the connection length for the volume in the limiter shadow and the rest of the SOL which is connected to the divertor.

The main task in the investigations performed with STRAHL was to obtain a prediction for the dependence of phase lag and amplitude dampening on transport parameters. Hence, a scan of the parameters defining the radial profiles of the diffusion and drift velocity coefficients was carried out. In the ELM-free investigations presented here the W-source prescribed to the model was modulated as to resemble the measured erosion rate at the ICRH limiters. The runs were mainly performed on the temperature and density profile of #25658 in the time interval $t = [2.0, 2.7]$ s. Following the results presented in [17] the transport of tungsten was assumed to be mainly neoclassical in the ETB and turbulent in the rest of the plasma. This leads to a strong inward drift in the ETB and a reduced diffusion coefficient in this volume of the plasma. Subsequently, these restrictions already predefine the overall shape of the profiles and therefore only few parameters had to be scanned.

The shape of the profiles used in the runs without ELMs are shown in figure 4.4. For the diffusion coefficient, the profile is described as a gaussian with two different decay lengths inside the LCFS

scanned par.	D_{SOL} [m^2/s]	D_{max} [m^2/s]	v_D [m/s]	$\tau_{ }$ [ms]
D_{SOL}	-	3.0	-80.0	3.5
D_{max}	1.0	-	-80.0	3.5
v_D	1.0	3.0	-	3.5
$\tau_{ }$	1.0	3.0	-80.0	-

Table 4.1: Values of the fixed parameters for the various scans

and as a constant in the SOL:

$$D(r) = \begin{cases} D_0 + (D_{max} - D_0) \cdot \exp\left(\frac{-(r-r_p)^2}{\sigma_0^2}\right) & \text{for } r < r_p \\ D_{SOL} + (D_{max} - D_{SOL}) \cdot \exp\left(\frac{-(r-r_p)^2}{\sigma_1^2}\right) & \text{for } r_p < r < r_{LCFS} \\ D_{SOL} & r > r_{LCFS} \end{cases} \quad (4.4)$$

The two different decay lengths σ_0 , σ_1 together with the variable joint location r_p give rise to a wide variety of possible diffusion profiles. However, as aforementioned, based on information from previous studies it was possible to keep some of the parameters at fixed values and scan only few of the quantities defining the profile. In the calculations presented here the joint location was fixed to the pedestal top, right next to the ETB, the diffusion coefficient in the center of the plasma D_0 was set to a very low value, mimicking neoclassical transport and the decay lengths were chosen according to the information found in [11, 17]. Regarding the diffusive radial transport, only the SOL diffusion coefficient and the value of the maximum diffusion at the pedestal top D_{max} were scanned. The drift velocity profile was represented with a simple gaussian, whose center was fixed at the radius of the LCFS. The width of the gaussian was set in such a way, that the drift velocity approaches zero at the pedestal top ($\rho_{pol} \approx 0.95$). In the case of the drift velocity profile, the scanned parameter is the maximum velocity at the LCFS. The fourth varied parameter is the parallel loss time in the SOL, since that value is expected to exhibit a strong influence on the impurity density in the main plasma.

The scan for each parameter was performed with the other parameters fixed. The overview over the whole scanned parameter range is given in table 4.1. The resulting behaviour of the inward propagating impurity density wave was evaluated at the radial positions corresponding to the experimental observation locations. For the determination of the phase lag, it makes no difference, whether the phase is evaluated from a spatially averaged signal (this resembles the experimentally obtained signal) or from the signal extracted at the center of the averaging interval. A short calculation will prove the statement. Assuming that the impurity wave propagates as a plane wave, $n_I(x, t) = A \cdot \sin(\omega t - kx)$

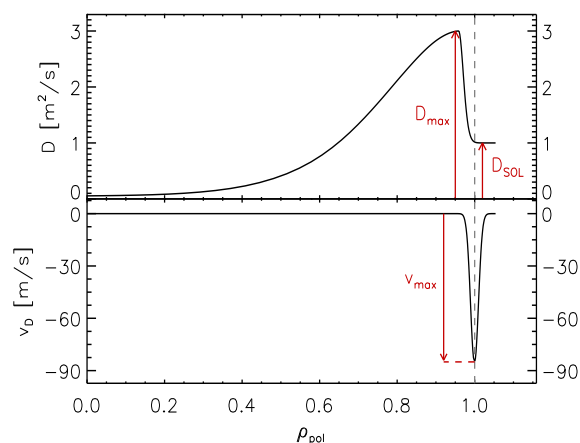


Figure 4.4: Profiles of drift velocity v_D and diffusion coefficient as a function of normalized radius. The red arrows visualize the scanned parameters.

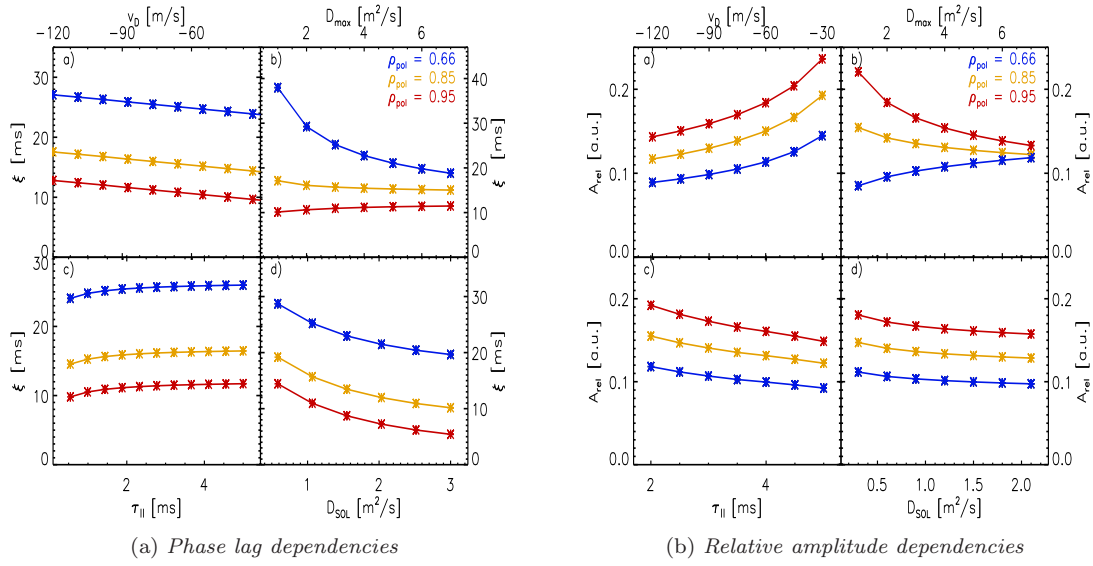


Figure 4.5: Phase lag and relative impurity density modulation amplitude as functions of various transport parameters for the case disregarding ELMs.

the signal spatially averaged on the interval $x_0 - \Delta x < x < x_0 + \Delta x$ is calculated as:

$$\langle n_I(x_0, t) \rangle = \frac{1}{2\Delta x} \int_{x_0 - \Delta x}^{x_0 + \Delta x} A \cdot \sin(\omega t - kx) dx, \quad (4.5)$$

with ω the angular frequency and k the wave number of the wave. Performing the integration gives:

$$\langle n_I(x_0, t) \rangle = \frac{A}{2k\Delta x} [\cos(\omega t - kx_0 - k\Delta x) - \cos(\omega t - kx_0 + k\Delta x)]. \quad (4.6)$$

Defining $y = \omega t - kx_0$ and applying a trigonometric identity this equation transforms into:

$$\langle n_I(x_0, t) \rangle = \frac{A}{2k\Delta x} [\cos(y)\cos(k\Delta x) + \sin(y)\sin(k\Delta x) - \cos(y)\cos(k\Delta x) + \sin(y)\sin(k\Delta x)]. \quad (4.7)$$

The cosine terms cancel out and the resulting expression can be splitted in a time independent factor $A' = \sin(k\Delta x)/(k\Delta x)$ and a term carrying the temporal behaviour at position x_0 :

$$\langle n_I(x_0, t) \rangle = \frac{\sin(k\Delta x)}{k\Delta x} \cdot A \cdot \sin(\omega t - kx_0) = A' \cdot n_I(x_0, t). \quad (4.8)$$

Of course, there is a restriction to the procedure. This calculation holds only for intervals Δx which allow for the assumption of a radially constant impurity amplitude which is true for the signals from the pedestal top and mid-radius, but not for the signal from inside the ETB. The phase of the impurity wave inside the ETB was therefore evaluated from the spatially averaged signal.

Results of the ELM-free STRAHL calculations

The results of the parameter scans in terms of phase lag behaviour are shown in figure 4.5a. The evaluation reveals a strong dependence of the phase lag on the diffusion coefficients, and only a weak influence of the drift velocity and parallel loss time. Following these calculations a change of the anomalous transport at the pedestal top should have a significant impact on the phase at mid-radius. Furthermore, the variation of the SOL diffusion coefficient is expected to apply a shift to all three tungsten signals. A change in one of these parameters would therefore lead to a measurable change

in the observed phase lag pattern. Since the influence of drift velocity and parallel loss time on the phase lag is only marginal the evaluation of the phase lag is insensitive to these two parameters and possible variations would go unnoticed, if only the phase lags would be evaluated.

In this context the second set of plots, figure 4.5b, shows the dependence of the relative amplitude on the scanned parameters. The relative amplitude is defined as $A_{rel} = A_W/b_W$, where A_W is the amplitude of the variation of some tungsten related quantity and b_W is the background value of that quantity. It was already mentioned before, that only at the tungsten source and at about mid radius absolute tungsten particle numbers can be determined experimentally. At the important positions in the ETB and on the pedestal top these absolute tungsten numbers are not obtainable, but only the radiation from tungsten can be used for transport investigations. This implies a transition from absolute tungsten numbers to relative amplitudes, where relative means the amplitude with respect to the tungsten background at each position. This is a natural choice, since a change in temperature or electron density affects the tungsten background radiation as well as the amplitude of the radiation from the modulated tungsten density wave. Therefore any changes in background plasma parameters leading to changes in the tungsten radiation are cancelled out. Thus, the relative amplitude defined this way is a good quantity for transport observations.

Coming back to the STRAHL calculations, all relative amplitudes were calculated on base of tungsten densities, since they are easily available from the code. Considering the graphs depicted in figure 4.5b it is easy to determine the parameters, that are expected to have a strong influence on the behaviour of the amplitude and the ones who will have a low impact. The inward drift is definitely a parameter with a strong impact on the amplitude. A faster inward drift velocity causes a reduction of the relative amplitude as can be seen in the top left plot of figure 4.5b). In the simulation this is due to an increase of the background tungsten density. Another parameter with a strong influence is the maximum diffusivity. For the innermost observation position a higher D_{max} causes a reduced damping which was expected. The behaviour at the ETB is reversed. Here the density wave propagates into a plasma volume, that already exhibits a steep tungsten density gradient. Adding tungsten into this plasma volume leads to an increased expulsion of tungsten from the plasma, thus causing a damping of the modulation amplitude. The strength of the diffusive outflux depends on the diffusion coefficient, in this case D_{max} . Therefore, an increase of D_{max} leads to a stronger amplitude damping at the ETB, while it reduces amplitude damping further inside the plasma, where the tungsten density profile is rather flat. The parallel loss time and the SOL diffusion coefficient are the parameters that do not have such a strong influence on A_{rel} . Actually D_{SOL} shows almost no effect on A_{rel} which makes this method blind for changes in this parameter. Also the parallel loss time $\tau_{||}$ is only weakly influencing the evaluated A_{rel} . Changes in this parameter will be hard to detect by means of evaluating the relative amplitude. This holds regardless of the observation position.

Summarizing the results from the STRAHL calculations without ELMs, the probing method is useful to detect changes in some parameters, while it is insensitive to changes in others. The phase lag ξ can provide information on changes in D_{max} and D_{SOL} , but is not adequate to detect changes in v_D and $\tau_{||}$. The relative amplitude A_{rel} is clearly sensitive to changes in D_{max} and v_D and shows some dependence on $\tau_{||}$, but almost none on D_{SOL} . Thus, following these calculations, it should be possible to detect changes in D_{max} , D_{SOL} , v_D with the diagnostic means available at AUG.

4.3.2 Transport Calculations regarding ELMs

The investigations including an ELM model were undergone with more degrees of freedom, where the influence of the ELM characteristics were the focus of these calculations. These calculations were also performed in order to determine whether taking into account ELMs in the model changes the relations found for the case without ELMs presented in the previous paragraph. Besides the ELM model, the treatment of impurities in the SOL and the implementation of the impurity source is very different as compared to the version of STRAHL presented before. The impurity source is calculated from first principles and includes a sputtering model. Furthermore, the parallel transport of impurities is no longer defined by a parallel loss time but by a Mach number.

The implementation of the W source will be presented curtly. It incorporates a sputtering model which calculates the erosion rates due to the physical sputtering of the ions impinging on the surfaces of the limiters. Since physical sputtering of W by deuterons is very low at the temperatures found in the SOL, heavier and higher charged ions, as for example carbon, have to be considered to obtain sputtering rates close to the ones measured. Therefore, this version of STRAHL also offers the possibility to calculate the transport of two or more impurity species at the same time. The flux of these low Z impurities impinging onto the limiter surface creates the W erosion rate using a sputtering yield $Y_W(E, m)$, that is dependent on the energy as well as the mass of the impinging ions [60]. The energy of the ions hitting the surface is given by

$$E = 2k_B T_i + 3Zk_B T_e , \quad (4.9)$$

which is an approximation deduced from the energy of the ions in a collisionless deuterium plasma [61]. It was assumed that $T_i = 2T_e$. The first term in equation 4.9 represents the average energy of the ions before entering the sheath and the second term stands for the additional kinetic energy gained in the sheath potential. Knowing the fluxes of the different ions onto the limiter surfaces, the W erosion flux can be easily calculated:

$$\Phi_W = \sum_{Z,i} Y_W^{Z,i} \cdot \Phi_{Z,i} , \quad (4.10)$$

where $\Phi_{Z,i}$ is the flux of ions i with charge Z and $Y_W^{Z,i}$ is the corresponding erosion yield for this ion species. The effect of prompt redeposition is also considered in this sputtering model. Hence, the sputtered atoms are assigned a Thomson velocity distribution and their sputtering angles are distributed cosine angular. A fraction of these sputtered atoms is ionized close enough to the wall, so that their first gyration leads them back to the wall where they reattach to it and therefore do not contribute to the total tungsten source. The fraction of promptly redeposited ions for the aforementioned velocity and angular distribution is given by [61]:

$$f_{reddep} = \frac{1}{1 + (\Delta t_{ion} \omega_c)^2} , \quad (4.11)$$

with Δt_{ion} being the time span needed for the first ionisation and $\omega_c = eB/m_W$ the cyclotron frequency of singly ionised tungsten. This fraction of particles is immediately subtracted from the reservoir of the neutral W atoms. Furthermore, the code allows to apply an additional sheath potential, simulating the effect of the increased sheath potential created by ICRH operation. With this additional tool it is possible to create a W source that reproduces the modulation of W erosion experimentally achieved by ICRH power modulation.

After ionisation, the sputtered impurities are subject to transport processes perpendicular and parallel to the magnetic flux surfaces. The perpendicular transport is treated by a diffusive and convective ansatz, as mentioned in the previous section. The parallel losses of impurities to the divertor are considered as volumetric losses which are described by the loss frequency $\nu_{||}$ times the number of impurity ions contained in the SOL $n_{SOL,I}$. The term $\nu_{||} \cdot n_{SOL,I}$ is then subtracted from the transport equation. The loss frequency is defined as:

$$\nu_{||} = \frac{v_{||,I}}{L_{||}}, \quad (4.12)$$

where $L_{||}$ is the parallel connection length between surface elements and $v_{||,I}$ is the parallel velocity of the impurities in the SOL. While the value of the connection length is easily determined (50 m between the divertor plates and 1 m between the limiters) the value of the parallel flow velocity is poorly known. As an estimate of $v_{||,I}$ it can be assumed that $v_{||,I} \approx v_{||,D}$, with $v_{||,D}$ being the mean flow velocity of the deuterons. It is expressed by the adiabatic acoustic speed sound times an average Mach number M :

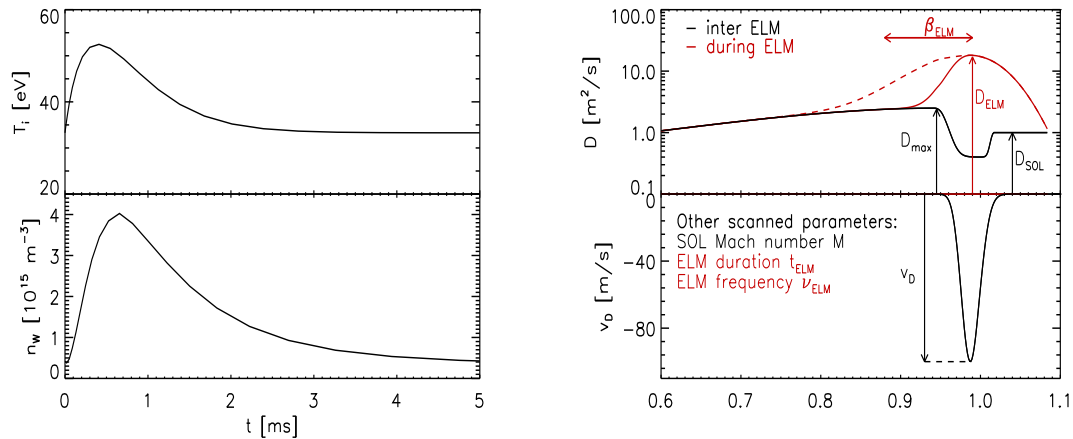
$$v_{||,D} = M \sqrt{\frac{k_B(3T_i + T_e)}{m_D}}. \quad (4.13)$$

The assumption that $v_{||,I} \approx v_{||,D}$ is justified, since the ion collision frequency is much higher than the loss frequency and therefore the impurities move with the same parallel velocity as the background ions [61]. The Mach number M is assumed to be constant throughout the SOL and is one of the scanned parameters in this investigation.

The ELM model in STRAHL

The ELMs in STRAHL are modeled on two levels. First, the influence of the ELM on the background plasma is simulated by an increase of electron and ion temperature in the SOL, whereas the background plasma conditions are constant during the simulation for the ELM-free case. The temperature increase is set to be short (0.4 ms) and decays over the time span of ≈ 1.5 ms (see figure 4.6a, top plot). This increase in temperature leads to an increased sputtering yield, mimicking part of the measured increase of W erosion during an ELM.

Second, the transport coefficients in the plasma edge are strongly altered for the duration of the ELM. The inward drift in the ETB is set to zero and the diffusion coefficient outside $\rho_{pol} \approx 0.90$ is increased to multiples of the inter-ELM value as shown in figure 4.6b. An interpolation between inter-ELM and ELM profiles is carried out over the user defined time span of an ELM and achieves a smooth transition between the two transport regimes. In the simulation, the effect of a vanishing inward drift combined with an increased diffusivity in the ETB region leads to an expulsion of impurity ions during the ELM caused by the strong impurity density gradient in the ETB. The time traces of the ion temperature and the tungsten density in front of the limiters are shown in figure 4.6a. The increased tungsten density in front of the limiters during an ELM is the result of ejected tungsten from the main plasma and an increased sputtering rate at the limiters. Besides tungsten, also carbon gets ejected into the SOL plasma. This additional low Z ion flux onto the limiter surface together with the elevated temperature leads to an increase of the W source as can be seen from equation 4.10. The slight time lag between the peak of temperature and W density is due to the time needed for the carbon to reach the limiters and enhance the sputtering rate.



(a) Ion temperature and W density during one ELM cycle

(b) Diffusion and drift profiles

Figure 4.6: Left plot: time traces of T_i and n_W in front of the limiters as calculated with STRAHL. Right plot: profiles of diffusivity and drift used in the STRAHL calculations for inter ELM periods in black and during ELMs in red. The parameters that are pointed out were scanned.

The raw data emerging from this ELM-model

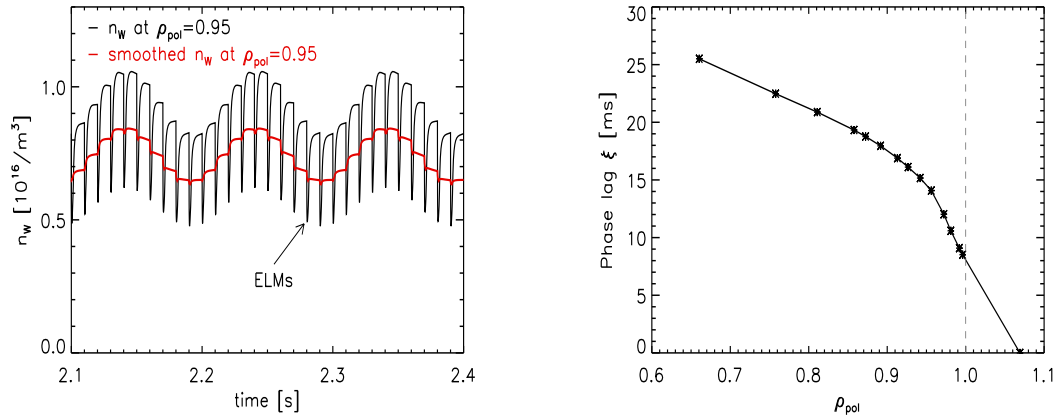
The assumed diffusion and drift velocity profiles look similar to the ones shown in the previous section, however they exhibit more features in the ETB region. This region is now assigned an own diffusion coefficient which is not equal to D_{SOL} , but is in the range of the expected neoclassical value of D , as figure 4.6b shows. This figure also contains the information on the parameters that were scanned during this investigation. As in the previous section, the inter-ELM values of the maximum diffusivity, SOL diffusivity, and inward drift were altered. Since the parallel transport toward the divertor is no longer expressed by the parallel loss time $\tau_{||}$, the influence of the parallel transport in the SOL was probed by changing the Mach number M of the flow.

The effect of the ELM activity on the observed quantities phase lag and amplitude was investigated by scanning the parameters that are thought to have the strongest impact on the aforementioned quantities. These parameters are the ELM frequency ν_{ELM} , the width of the ELM affected region defined by β_{ELM} , *i.e.* the region in which the diffusivity is increased for the time of the ELM duration, the ELM duration itself t_{ELM} and the maximum diffusivity during an ELM D_{ELM} .

v_D [m/s]	-50	-80	-110	-150
D_{max} [m^2/s]	1.2	2.5	3.8	5.5
D_{SOL} [m^2/s]	0.1	0.3	0.6	0.9
$M_{ }$	0.07	0.1	0.15	0.21

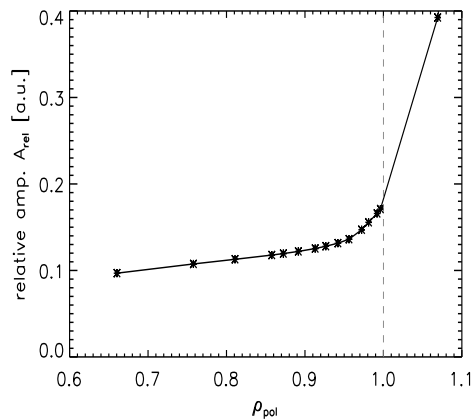
Table 4.2: Values of the independent inter-ELM variables.

Before presenting the results regarding the evaluation of the parameter scans (tables 4.2 and 4.3), the raw data will be shown. All STRAHL runs were performed in such a way that the background tungsten density reached a steady state. Figure 4.7 depicts the time trace of the modeled tungsten density at $\rho_{pol} = 0.95$, the phase lag profile and the profile of the relative amplitude obtained



(a) Time trace of the tungsten density

(b) Profile of the phase lag wrt. the phase at source



(c) Profile of the relative amplitude

Figure 4.7: An overview of the raw data used to evaluate the dependencies of phase and amplitude on the scanned parameters.

with one particular parameter configuration. The effect of the ELMs on the tungsten time trace is instantly visible in figure 4.7a as a high frequency modulation ($\nu_{ELM} = 100$ Hz) on top of the sinusoidally varying tungsten density ($\nu_{mod} = 10$ Hz). It also shows that the background tungsten density is constant. However, the ELM activity does not hamper the evaluation of the phase and amplitude of the sinusoidal background. This evaluation then provides radial profiles of the phase lag with respect to the phase at the source and profiles of the relative amplitude shown in figures 4.7b and 4.7c.

Inter-ELM parameter scan

Since the investigation of the influence of the inter-ELM parameters on the phase lag and relative amplitude delivered very similar results to the case without ELMs, these results will - for the sake of brevity - not be presented here. Thus, the model predicts that even in the presence of ELMs the probing method with a modulated tungsten source should be sufficiently sensitive to detect changes in the transport parameters.

ν_{ELM} [Hz]	50	100	150	200
t_{ELM} [ms]	0.6	0.9	1.3	2.0
D_{ELM} [m ² /s]	15	18	22	35
β	3.5	4.0	6.0	8.0

Table 4.3: Values of the independent ELM-variables.

ELM-related parameter scan

The ELM-related parameters were scanned to check for possible influences of these independent variables on the observables phase lag and relative amplitude. In total there were four parameters, which were altered: the ELM frequency ν_{ELM} , the duration of one ELM t_{ELM} , the elevated diffusivity during an ELM and the volume which is affected by the ELM diffusivity, here represented by β . The meaning of ELM frequency, ELM duration and elevated diffusivity are easy to grasp, but the effect of β on the diffusivity profile is rather hard to picture. In order to bring some meaning to this parameter a threshold is defined. This threshold relates to the change of the diffusivity profile during an ELM. If somewhere along the radial coordinate ρ_{pol} the increase of diffusivity is greater than 5% as compared to the inter-ELM value, then the area is regarded as affected by the ELM. Thus, the range of beta used in this investigation then translates to an inner boundary. For the two extremes $\beta = [3.5, 8.0]$ this means an affected region outside $\rho_{pol} > [0.95, 0.80]$. For a better understanding figure 4.6b shows the diffusion profile for these two cases.

The full range of the values to which the parameters were set within this modelling effort is listed in table 4.3. The calculations performed with STRAHL covered all 256 possible combinations of the ELM parameters. Since the aim is to distinguish between the effects of the various parameters on the observables, only parameter scans of one variable with all other variables fixed will be presented.

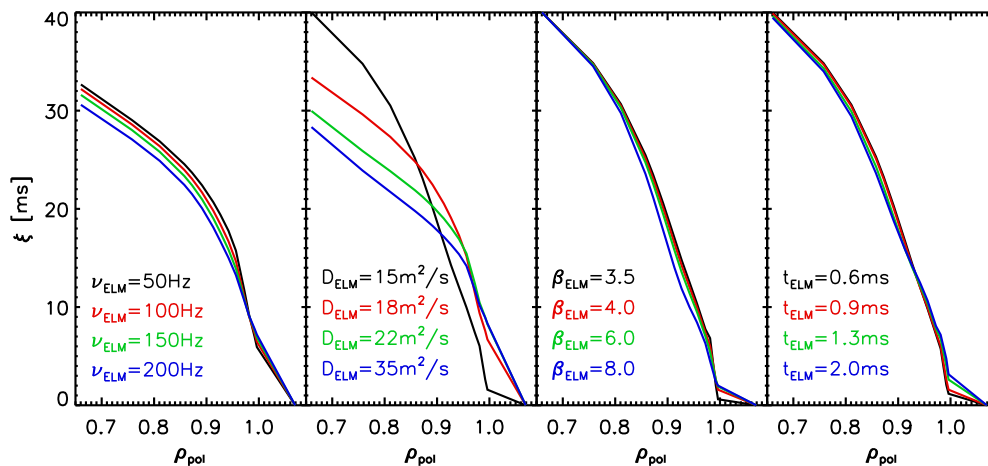


Figure 4.8: Effects of the parameter scans on the phase profiles

In the case of the phase lag profiles, it is very clear from picture 4.8 that a change of the ELM diffusivity, D_{ELM} , should lead to a measurable phase shift at the observational positions in the experiment. On the contrary, any variation of the ELM duration, t_{ELM} , and width of the ELM affected region, β_{ELM} , would go unnoticed due to the measurement uncertainties of the diagnostic system. The effects of the various ELM frequencies, ν_{ELM} , on the phase profiles are rather subtle

and are close to the sensitivity limits of the spectrometers. In each scan, the fixed variables were kept at the values in the second column of table 4.3, *e.g.* the ELM frequency scan was performed at $D_{ELM} = 18 \text{ m}^2/\text{s}$, $\beta_{ELM} = 4.0$ and $t_{ELM} = 0.9 \text{ ms}$.

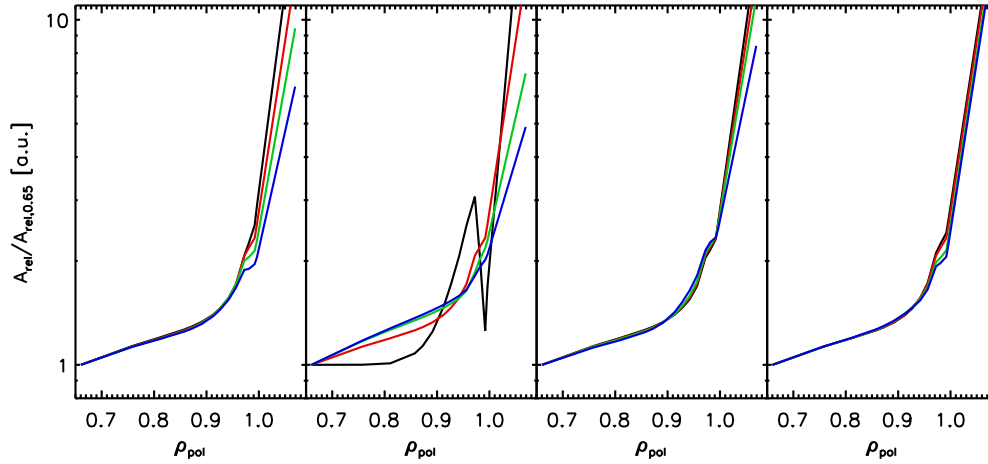


Figure 4.9: Effects of the parameter scans on the relative amplitude. The color coding is identical to the one from figure 4.8. For a better comparison, the profiles have been normalized to the value at $\rho_{pol} = 0.65$.

Looking at figure 4.9, the probing ability of the experimental setup for any of the ELM parameters studied here is nearly nonexistent. Only in the case of the ELM diffusivity one might be able to detect some changes in the profiles of the relative amplitude. Seen in this light, the experimental method applied here would be blind for anything but a change of the ELM diffusivity and perhaps ELM frequency.

The GI spectrometer also gives information on the tungsten content of the plasma. Thus, it would be interesting to investigate the effect of a variation of the ELM parameters on the tungsten density profiles.

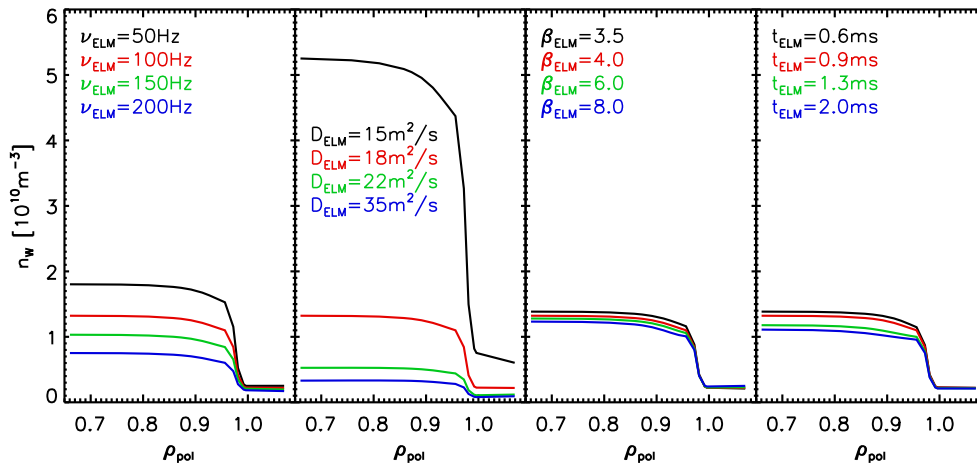


Figure 4.10: Effect of the ELM parameter scans on the tungsten density profile. The color coding is identical to the one in the ELM frequency scan from figure 4.8.

The message of figure 4.10 is quite positive: the two ELM parameters whose effects on ξ and A_{rel} are below the detection limits have at the same time only a very limited impact on the tungsten

content of the plasma. On the other side, the ELM parameter with the strongest impact on the tungsten behaviour, D_{ELM} , would leave a clear signature in the phase shift profiles and a change of this parameter should therefore be easily detectable. Last, the ELM frequency shows a distinct influence on the tungsten density, which was to be expected from the nature of this model. And even though the ELM frequency would not leave a distinct footprint in the ξ and A_{rel} profiles, it is the one parameter which is controlled actively and measured directly in the experiments to follow.

There are three statements arising from the modeling efforts. First, applying a modulated tungsten source and measuring the phase lag and relative amplitude at the experimentally available radial locations should allow to detect major changes of the radial transport coefficients. Second, within this diffusive ELM model, changes of the two ELM parameters with the strongest impact on the tungsten density, ν_{ELM} and D_{ELM} , should be detectable in the experiments. Third, the method would be insensitive to changes of the parallel transport parameters, *e.g.* the parallel flow velocity in the SOL. However, this quantity strongly influences the tungsten influx to the plasma and should therefore not be neglected.

Chapter 5

Experimental Results

This chapter will present the experimental observations and their interpretation. The experimentally observed tungsten behaviour does not agree with the predictions from the STRAHL calculations. Especially the predicted influence of the ELM-frequency on the tungsten concentration is in disagreement with the experimental data gathered in this work. The interpretation of the data leads to the rejection of the ELM model as it is used in STRAHL and introduces the parallel flow in the SOL as a major parameter to control the tungsten concentration in the main plasma.

5.1 Dependence of W-concentration on Gas Puff and Triangularity

As mentioned in the previous chapter, the experiments aimed at observing changes of the tungsten transport in the ETB region. In order to probe the radial transport, a modulated tungsten source was created at the ICRH limiters by applying the ICRH power as a sinusoidal function. STRAHL calculations predicted the sensitivity of this method for nearly all relevant transport parameters. An important point of these experiments was the decoupling of the D-injection rate and the ELM frequency, by change of the upper triangularity. In previous works, where the D-injection rate and the ELM frequency are coupled, a clear inverse dependence of the tungsten concentration on the ELM frequency has been reported [14]. In this light, the results for the decoupled case presented here are rather unexpected and will be laid out in the following paragraphs.

Since only the main chamber gas puffing rate and the upper triangularity were varied, the discharges are well described by only few time traces. Figure 5.1 shows the determinant time traces of the first three discharges (#25658, #25660, #25661), during which a decoupling of ELM-frequency from gas puffing was achieved. These discharges were identical but for the D-puffing ramps which are shown in the top plot of the figure. The gas puffing rate and the upper triangularity are the two actuators used in these experiments and define three distinct phases in the discharges. It should be noted, that experiments #25658 and #25661 have a period in which all externally adjustable plasma parameters are equal. This period was inserted to ensure that the overall machine conditions did not change between discharges. The second plot shows the upper triangularity for all three discharges. In the next plot the ELM-frequencies show a clear dependence on the triangularity. Starting at about 110 Hz, ν_{ELM} declines with every triangularity step by about 30 Hz, first down to 80 Hz and then in the final stage of the discharges to 50 Hz. The gas puffing has only a marginal influence on the ELM

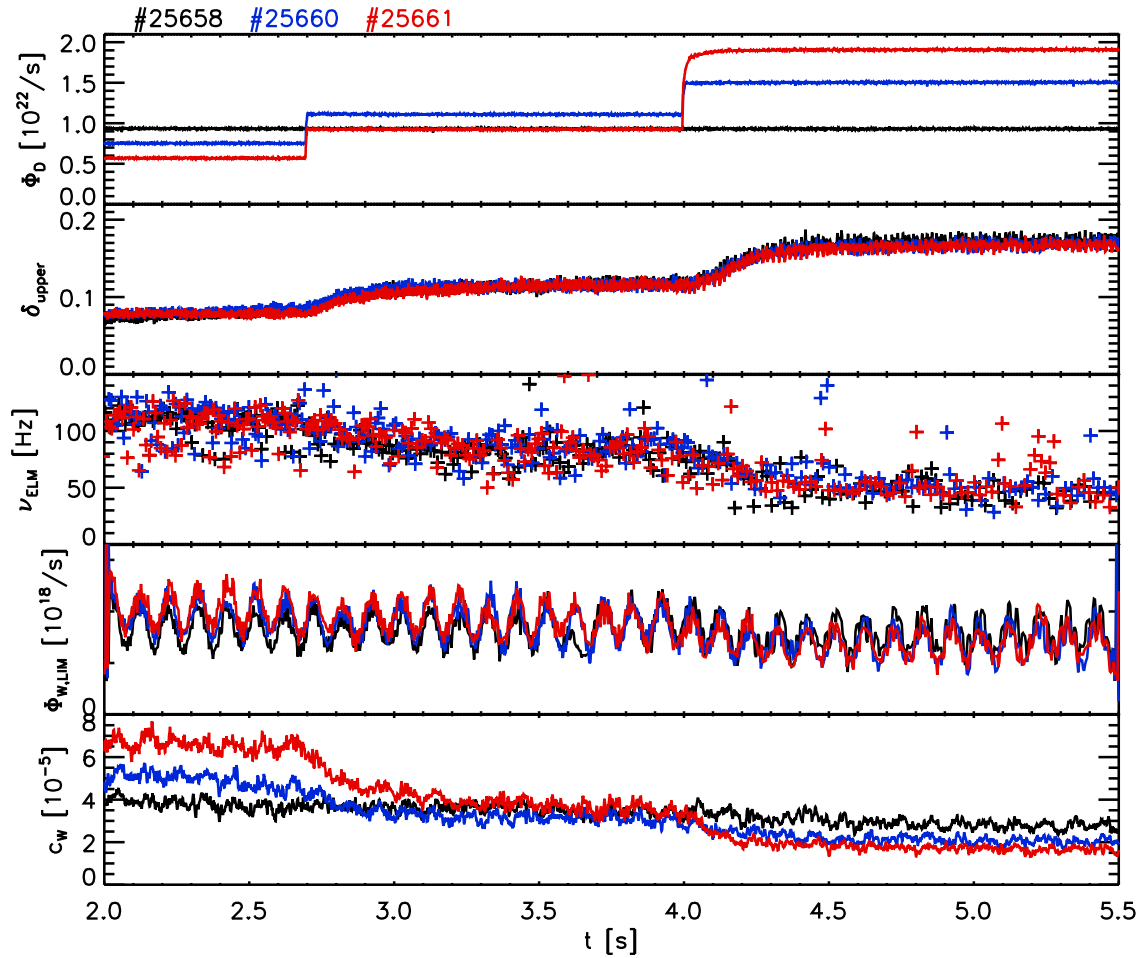


Figure 5.1: *Several time traces of three discharges with decoupling of ELM frequency and gas puffing rate.*

frequency in these discharges. The decoupling of ELM-frequency and gas puffing rate is obvious in these time traces. The ELMs have been analyzed from the divertor thermo currents which provide a very good ELM signature. However, for the sake of clarity this time signal has not been included in the figure. The tungsten erosion flux from the ICRH antenna limiters is plotted in the second to last plot. It has been obtained from the spectroscopic measurements laid out in chapter 2. This data has been gathered with a 3.4 ms time resolution. A 10-point boxcar smooth removes the "noisy" ELM signature and reveals the sinusoidal modulation imprinted by the ICRH power. It should be noticed, that the tungsten source at the limiter is nearly constant aside from the intended modulation. It shows a slight decline at the transition to the last phase of the discharges which is due to the shaping of the plasma. Even though the distance of separatrix to wall is kept constant in the midplane, the stronger shaping of the plasma moves the plasma away from the upper section of the ICRH limiters. This results in a slight reduction of the particle flux onto the wall, therefore decreasing the erosion flux. The term 'constant' applies not only to the behaviour during one discharge, but also to the erosion rate when comparing the three discharges to each other. The gas puffing rate does not alter the erosion rate at the limiters beyond the measuring uncertainty. This is an important point when

interpreting the last time trace in figure 5.1: the tungsten concentration at mid radius.

The tungsten concentration can be either studied from the 3 phases of one single discharge, or from one phase of all three discharges. Regardless of the approach, the result is the same: the gas puffing rate has the only detectable influence on the tungsten concentration. This is, of course, besides the sinusoidal modulation which is generated by the modulated tungsten erosion rate at the ICRH limiters. Taking for example the tungsten concentration of #25658 which is plotted in black in figure 5.1. This discharge was run with a constant gas puffing rate. The tungsten concentration is approximately constant throughout the flat top phase. There is a slight negative slope, but it is caused by the slow increase of electron density which is a reaction of the plasma to the increase in triangularity. If the tungsten density is considered, it is constant. This is an astonishing measurement in the light of a strongly varying ELM-frequency which changes by a factor of 2 in the observed time interval. Coming now to the comparison of the tungsten levels of different discharges. Always looking at time intervals with the same triangularity values, the measurements provide even more proof of the importance of gas puffing rate to the tungsten concentration. In the first phase from 2.0s to 2.7s the gas puffing rates are $0.6 \cdot 10^{22}/s$ for #25661, $0.8 \cdot 10^{22}/s$ for #25660 and $1.0 \cdot 10^{22}/s$ for #25658. The ELM-frequency is 110 Hz for all three discharges. However, the discharge with the highest gas injection rate shows the smallest tungsten concentration, while the lowest gas puff coincides with the highest c_W . The second phase in which #25658 and #25661 have the same gas puff level has been inserted to check via the tungsten concentration that the machine conditions did not change between discharges. Since c_W is indeed the same it allows for the comparison of the 3 discharges.

The last phase exhibits the same dependence between gas puffing and tungsten concentration. Since the ELM-frequency in each phase is the same for all three discharges it must be deduced, that it has no detectable influence on the tungsten concentration in the main plasma. From the findings of previous works, the expected tungsten concentrations would have had to follow the

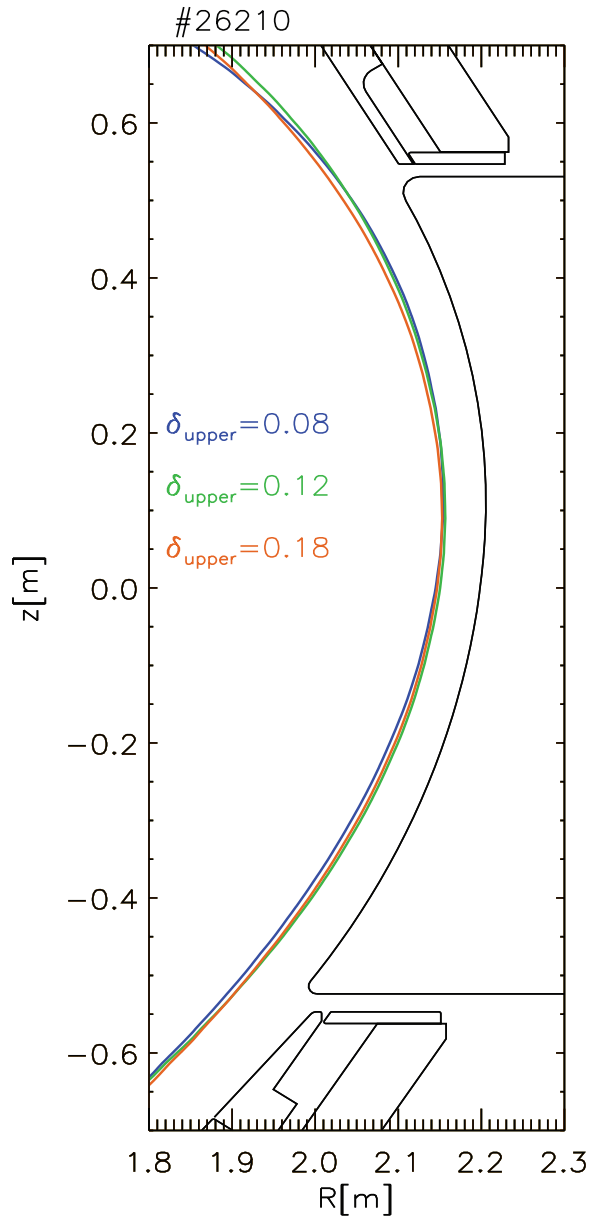


Figure 5.2: *Separatrix positions on the LFS for the 3 triangularities used in the optimized discharge design. The shape follows the ICRH limiter as closely as possible for all three cases.*

inverse of the ELM-frequency. This is absolutely not the case for the data presented here. The highest tungsten concentrations are measured at the highest ELM-frequencies, while the lowest tungsten concentrations coincide with the lowest ELM-frequencies. At first sight, ELMs seem to be unnecessary for the control of the tungsten concentration. This is of course not the case. There are numerous publications that report experimental evidence for the impurity flushing by ELMs, *e.g.* [18, 28, 62]. The new aspect of the data presented here is, that the ELM-frequency itself has no influence on the tungsten concentration. This was put in numbers by regarding the decay time of the tungsten concentration of #25661 between phase one and two and between phase two and three. The decay times are virtually identical: 75 ± 10 ms and 77 ± 8 ms, evaluated by fitting an exponential decay function on a 300 ms time interval starting 30 ms after the change from one phase to the other. This leads to further implications regarding the impurity exhaust mechanism by ELMs which will be laid out in detail in section 5.3.

More data will be presented to show the strong link between the gas injection rate and the tungsten concentration. In order to rule out coincidence effects - the low gas puffing is applied at low triangularity and high gas puffing at high triangularity (see figure 5.1)- the discharge program was reviewed and reshuffled. Since these experiments were also preparational discharges for measurements in the SOL with Langmuir probes, the NBI heating was reduced to 5 MW in order to reduce the heat load on the probe head. Furthermore, the shaping of the plasma was optimized to follow the shape of the ICRH limiters as closely as possible for all three triangularity values. Adjusting the shape is necessary to exclude effects that might arise from the varying distance between wall and plasma. As aforementioned, this was actually the case for the experiments presented above. Even though the distance between wall and separatrix in the midplane was kept constant during the discharges, a thorough examination of the separatrix position over the full range of the ICRH limiter revealed that the distance increases at the other positions along the ICRH limiter with increasing upper triangularity. For the new discharge design this is not the case any more as figure 5.2 shows. Distance effects can therefore be excluded as an explanation of the behaviour of the tungsten concentration in this new discharge setup.

Furthermore, the gas puffing scheme was reversed for the second discharge (#26211) presented in red in figure 5.3. For this discharge, the low gas puffing coincides with the high triangularity and vice versa. Unfortunately, the ECRH system shut down during the second phase at roughly 3.6 s due to technical difficulties. The discharge then suffered from central tungsten accumulation which renders the third phase of #26211 useless for evaluation. Independent of this partial failure of the discharge, it still provides valuable information about the tungsten behaviour.

Regarding the first phase of #26211 and the last phase of #26210, both discharges exhibit an approximately equal tungsten concentration. This is astonishing, since the two phases differ in many aspects: triangularity ($\delta_{upper} = 0.08$ vs $\delta_{upper} = 0.18$), ELM-frequency ($\nu_{ELM} = 135$ Hz vs. $\nu_{ELM} = 55$ Hz), even the tungsten erosion source at the outer divertor ($\Phi_{W,DIV} = 3.2 \cdot 10^{18} \text{ s}^{-1}$ vs. $\Phi_{W,DIV} = 1.8 \cdot 10^{18} \text{ s}^{-1}$). The only factors that are the same are the gas puffing and the tungsten erosion at the ICRH-limiter. Only this finding by itself already points strongly towards the high influence of the gas puffing on the tungsten concentration and rules out any influence of ELM-frequency on the tungsten behaviour. It is also easy to deduce a qualitative evaluation of the importance of the divertor tungsten source: This source does not exert a major influence on c_W . This is better visualized in the time trace of $\Phi_{W,DIV}$ of #26210, phase one and two. The divertor source remains approximately constant during both phases (phase one: $\Phi_{W,DIV} = 4.4 \cdot 10^{18} \text{ s}^{-1}$,

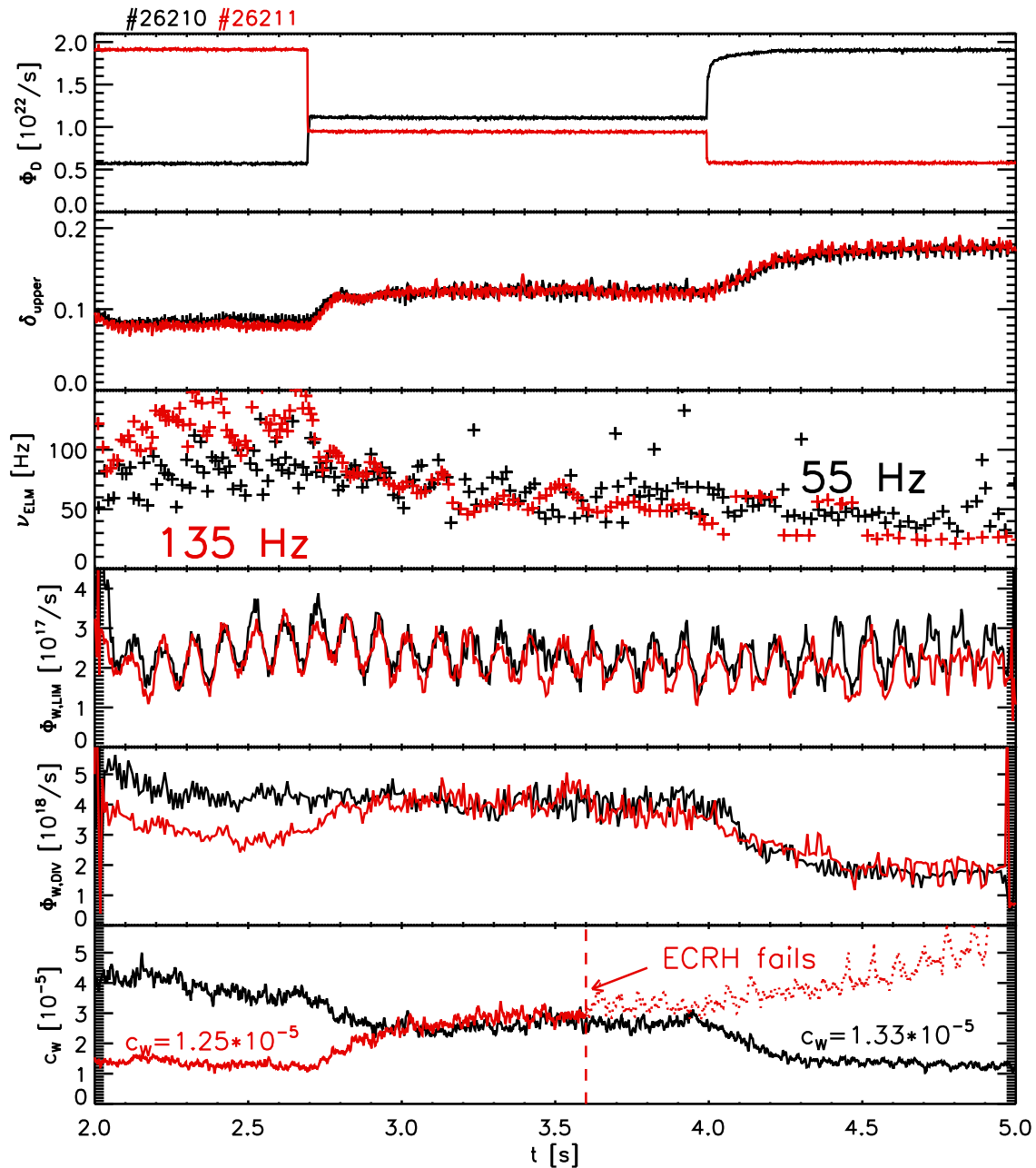


Figure 5.3: Several time traces of two discharges with optimized shaping and reversed gas puffing schemes. The tungsten erosion signals have been smoothed to eliminate the distracting influence of the ELMs

phase two: $\Phi_{W,DIV} = 4.0 \cdot 10^{18} \text{ s}^{-1}$), but the tungsten concentration changes drastically: phase one: $c_W = 3.9 \cdot 10^{-5}$ and phase two: $c_W = 2.6 \cdot 10^{-5}$. A change of 10% of the tungsten divertor source faces a change of 33% in tungsten concentration. These numbers already show the good separation of the divertor source from the main plasma which, of course, is the main task of a divertor. The main part of the change in the tungsten concentration must be caused by other mechanisms than a change of the tungsten erosion source. There is more evidence for the low impact of the divertor tungsten source on the tungsten concentration. Comparing now the divertor source during the first

phase of both discharges, a well known effect becomes visible: the reduction of tungsten erosion by increased gas puffing. This affects, however, only the divertor source. The explanation for this was given by [14], and relates the lower erosion to a reduced temperature of the divertor in the inter-ELM phases. This reduction of the divertor source is by far not enough to explain the big difference in the two tungsten concentrations in phase one of both discharges. Regarding the ratio of the two divertor sources $R_{DIV} = \Phi_{W,DIV}^{\#26210} / \Phi_{W,DIV}^{\#26211} = 1.41$, it is much smaller than the ratio of the tungsten concentrations $R_{cW} = c_W^{\#26210} / c_W^{\#25211} = 2.68$. The ELM frequency in this phase differs between both discharges due to the applied gas puffing rates: $\nu_{ELM}^{\#26210} = 85$ Hz, $\nu_{ELM}^{\#26211} = 130$ Hz. Even though this could be interpreted as the reason for the difference in the tungsten concentrations, it should not in the light of the much higher difference in ELM frequencies of the first phase of #26211 and the last phase of #26210 and nearly identical tungsten concentrations of these phases. There must be a second powerful mechanism connected with the gas puffing, causing this strong reduction of tungsten content in the main plasma.

As a last word to the tungsten erosion at the divertor, the steep drop in the last phase will be commented. This might well be a measurement artefact. The discharges were not run with a controlled strike point position of the separatrix on the outer divertor. Therefore, increase in δ_{upper} leads to a downward movement of the strike point. It should be mentioned that the highest tungsten erosion rates are usually measured close to the strike point. While the strike point still hits the divertor in a well diagnosed area during phase one and two, it moves to the lower edge of the divertor in phase three. There, the tungsten erosion diagnostic can not observe the full extent of the strike point site which results in the observation of a reduced tungsten divertor source.

All discharges were performed with a marginal ICRH heating. It might now be argued, that the ICRH heating could somehow have caused this strong influence of gas puffing on tungsten concentration. Therefore, discharge #25658 was repeated without applying ICRH power. The discharge without ICRH heating (#25686) showed, of course, a reduced erosion source at the ICRH limiters, but exhibited in all other parameters a similar behaviour as #25658. Especially the ELM-frequency in both discharges is very much the same. Also the main focus of this discharge, the behaviour of the tungsten concentration, was not influenced by the ELM-frequency, just like for the case with ICRH heating. Thus, the ICRH heating was ruled out as a cause for the observed influence of Φ_D and the lack of impact of ν_{ELM} .

Before addressing the possible cause for this unprecedented behaviour of tungsten concentration and ELM-frequency, an overview plot will be shown. This plot (figure 5.4) is set up from the data of several discharges run in the 2009 experimental campaign. All discharges were run with the modulated ICRH heating described in chapter 4 and a constant distance of the separatrix from the wall in the midplane. The legend in the right box of figure 5.4 shows the discharge numbers and the respective time intervals, in seconds, chosen for evaluation. Time intervals were chosen mainly by two criteria: first, the tungsten concentration had to be equilibrated and second, the time interval had to be long enough to allow for the evaluation of the tungsten modulation parameters, *i.e.* phase lag and relative amplitude. The symbols relate to the discharge, while the color coding relates to the time intervals of the discharge. Discharges, where only one time interval was selected for evaluation are color coded in black. Otherwise, the blue relates to low δ_{upper} , green to medium δ_{upper} and red to the highest δ_{upper} . With the decoupling of ELM-frequency and gas puffing which is inherent to all the discharges presented here, an approximately exponential dependence of c_W on Φ_D becomes visible in the left hand plot of figure 5.4. As a contrast, the graph showing c_W over ν_{ELM} exhibits

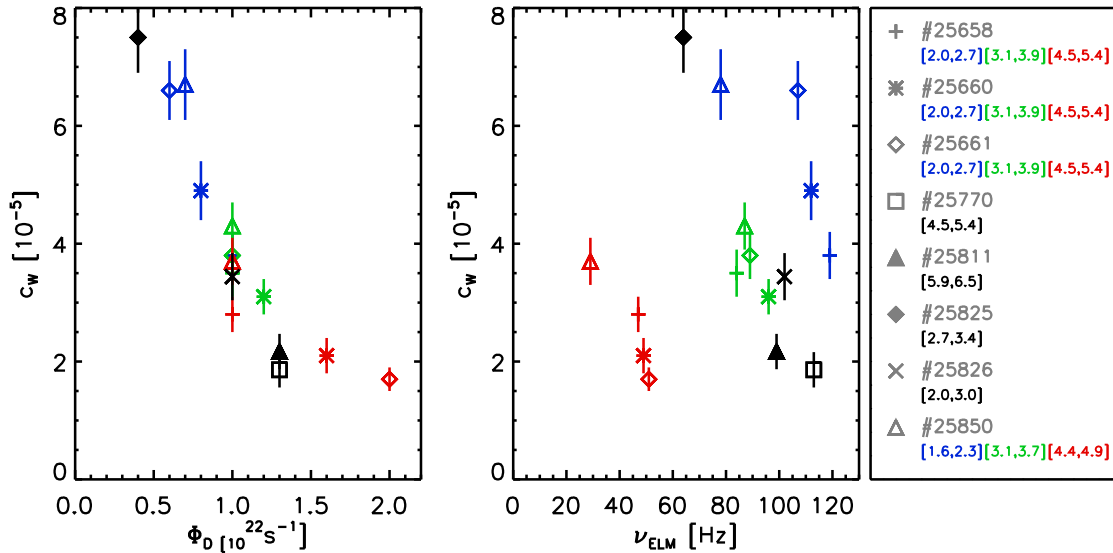


Figure 5.4: Overview over the tungsten concentration plotted against gas injection rate and ELM frequency. The discharges agree in most plasma parameters, but Φ_D and δ_{upper} . The symbols relate to the individual discharge, while the color coding refers to the evaluated time intervals (in seconds).

no clear relation between the two quantities.

The question might arise whether this is a tungsten behaviour inherent only to the discharges performed in the framework of this study. As can be seen from figure 5.5, it is not. The plot shows the same data points presented in figure 5.4, plus an additional set of data points from discharges performed in the 2008 campaign. Those discharges were run at constant triangularity ($\delta_u = 0.12$, right in the center of the triangularity range used for the 2009 campaign), while the ELM-frequency was controlled by the deuterium gas puffing rate. What made the discharges valuable for this study is that in the evaluated time intervals the distance from separatrix to wall and the heating power are constant. The ICRH was not used. A detailed description of the discharge parameters is given in reference [14]. For these discharges, just as for the discharges presented before, the time intervals chosen for evaluation had to exhibit an equilibrated tungsten concentration. This time the y-axis is shown in logarithmic scale and an exponential function was fitted to each data set to guide the eye.

However, guiding the eye is not the sole purpose of the fit. It allows to compare the two data sets on a mathematical basis. The function used for the exponential is defined as follows:

$$f_{cW}(\Phi_D) = A_0 + A_1 * e^{(-A_2 \cdot \Phi_D)} \quad (5.1)$$

Table 5.1 lists all fit parameters and their uncertainties. The fit parameters A_0 and A_1 express the asymptotic behaviour of the tungsten concentration at the two extremes of no gas puffing and infinite gas puffing. Of course, this asymptotic behaviour is only an extrapolation based on the rather restricted set of data pairs of $c_W(\Phi_D)$. A_0 and A_1 are not related to the gas puffing, but to other factors, that also have an impact on the tungsten concentration, two of them being the distance from separatrix to wall, the other the total heating power. Their influence is observable in figure 5.5, where the discharges from the 2008 campaign have an overall strongly reduced tungsten concentration. Compared to the discharges from 2009, these discharges were run with a reduced NBI heating (5.0 MW vs. 7.5 MW) and in addition the distance between separatrix and wall in the midplane is 1.5 cm larger.

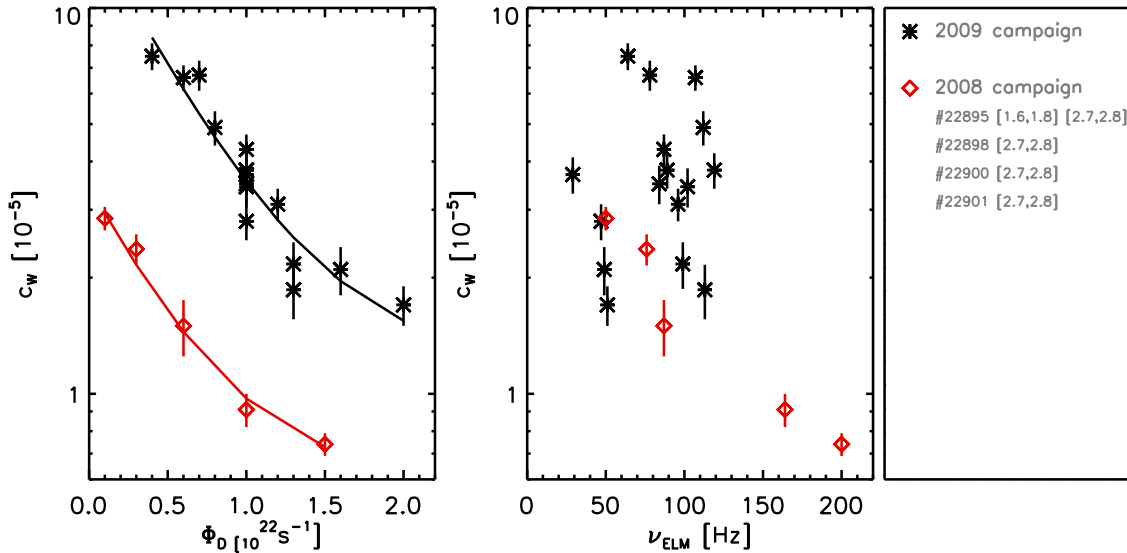


Figure 5.5: Comparison between discharges with ELM frequency control by δ_{upper} (in black) or by Φ_D (in red). The lines in the left plot are fits to the data.

	A_0	A_1	A_2 [s]
2009 campaign	1.2 ± 0.3	15.1 ± 2.0	1.8 ± 0.3
2008 campaign	0.6 ± 0.1	2.9 ± 0.3	2.0 ± 0.5

Table 5.1: Fit parameters for the exponential fit used to parametrize the two data sets from 2008 and 2009. For the fit c_W was used in $[10^{-5}]$ and Φ_D in $[10^{22} \text{ s}^{-1}]$.

However, these plasma parameters are not under investigation here. The fit parameter of interest is A_2 . It provides the means to compare the two data sets with respect to the gas puffing. Looking at the actual values of A_2 for the two cases presented here, the congruence is astonishing. Two sets of discharges which differ in almost all aspects, except for being ELMy H-mode and running in the lower single null configuration, show the same dependence of the tungsten concentration on the gas puffing rate. It must be deduced, that the effect observed here must be global and is not restricted to a special plasma configuration. One more aspect is pointed out very clearly in figure 5.5: the ELM-frequency is not influencing the tungsten concentration in any way (2009 campaign). The red dots from the 2008 campaign apparently line up to resemble a strong dependence between ELM-frequency and tungsten concentration, but it should be kept in mind, that the ELM-frequency was controlled via the gas puffing rate in these discharges. The gas puffing rate, however, was found to exhibit exactly the same impact on the tungsten concentration in both campaigns. Therefore, there is no more room for the impact of other parameters *e.g.* ELM-frequency, and the correlation between ν_{ELM} and c_W might have been a coincidence caused by the control mechanism for the ELM-frequency. Thus, the only relation that is found in both data sets, is the one between gas puffing and tungsten concentration.

Before closing this section, a look will be taken on the ELMs themselves. It will be shown that the ELM behaviour is not in any way different to the ELMs observed in other type one ELMy H-mode. To illustrate this statement figure 5.6a plots the ELM size (ΔN_{ELM}) which is the number of expelled particles per ELM, over the ELM frequency. A red line represents the fit with a model $\Delta N_{ELM} \propto$

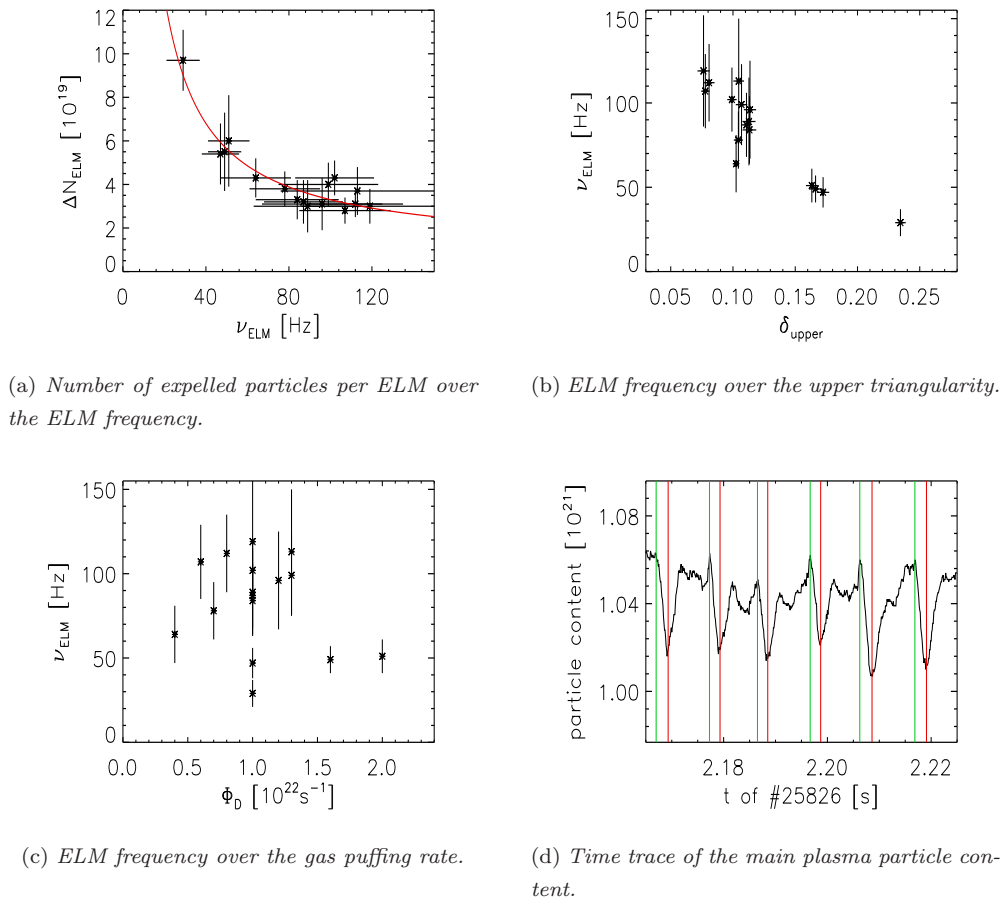
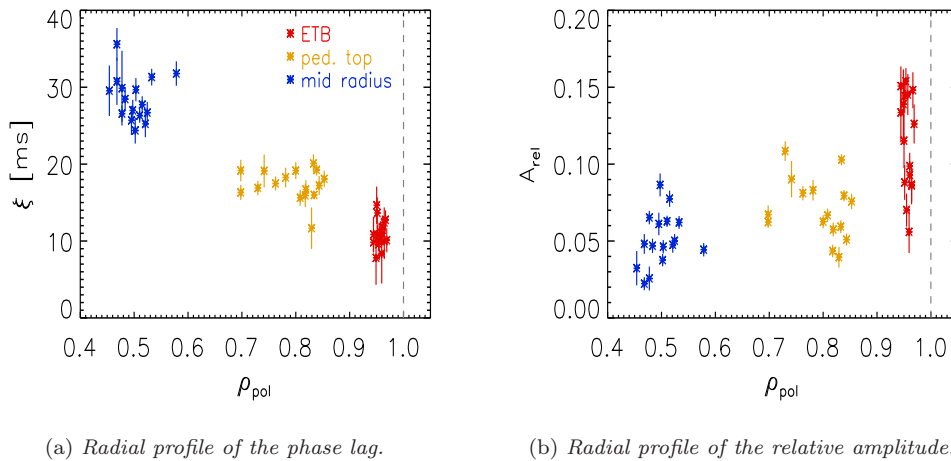


Figure 5.6: Some ELM quantities measured during the time intervals of the experiments listed in figure 5.4. The data in figure 5.6a was fitted by a model $\Delta N_{ELM} \propto 1/\nu_{ELM}$, represented by the red line.

$1/\nu_{ELM}$. The model agrees with the data gathered in the experiments. This proportionality between ELM size and ELM frequency was already shown before in [19]. The ELM size was evaluated by the same method as presented in [19]. The method employs the total plasma particle number derived from the deconvoluted interferometry signals and calculates the difference of pre- to post-ELM particle content in the plasma. A visualization of the method is shown in figure 5.6d, with green lines indicating the start of an ELM and red lines its end.

The other two graphs depict the influence of the independent variables, gas puffing and upper triangularity, on the ELM frequency. It is clearly visible from figure 5.6b, that the upper triangularity plays the major role in adjusting the ELM frequency. The influence of the gas puffing on the ELM frequency is rather small compared to the upper triangularity. However, it is detectable in the scatter of ELM frequencies present in figure 5.6b and provides another evidence, that the ELMs do not show any abnormal behaviour.

Figure 5.6c can be interpreted as the good separation of gas puffing and ELM-frequency. Unlike for the experiments from the 2008 campaign, which are showing a linear dependence of the ELM-frequency on the gas puffing rate, there is no connection between both for the experiments performed in the course of this study.



(a) Radial profile of the phase lag.

(b) Radial profile of the relative amplitude.

Figure 5.7: Phase lag and relative amplitude plotted on a radial grid. The broken grey line depicts the separatrix location

In this section experimental evidence was provided which stresses the strong impact of the gas puffing on the tungsten concentration. A minor part of this relation is due to a reduction of the divertor source. The main contributing mechanism, however, is a question that will be addressed in the following sections. By decoupling the gas puffing rate and ELM-frequency it was shown, that the ELM-frequency has no influence on the equilibrium tungsten concentration for the triangularity range covered in these experiments (low to medium average triangularity). The following sections cover the cause for this strong dependence of c_W on Φ_D and will provide an explanation for the lack of influence of ν_{ELM} .

5.2 Evaluation of Phase Lag and Relative Amplitude

With the application of a modulated tungsten source a method for probing the tungsten transport in the outer regions of the plasma was implemented. From the modelling presented in chapter 4.3.1, this method should be sensitive to changes of the radial transport parameters, *i.e.* the SOL diffusivity D_{SOL} , the radial drift velocity in the ETB v_D , and the maximum diffusivity right at the pedestal top D_{max} . The evaluation of the phase lag and relative amplitude follows the steps laid out in section 4.2. It was performed on all time intervals of the discharges presented in figure 5.4 and the results are laid out in figure 5.8.

In order to become confident with this probing method figure 5.7 shows the radial "profiles" of phase lag and relative amplitude for the time intervals mentioned in the previous paragraph. Of course, one can hardly speak of a profile with only three radial observation locations. Nevertheless, this approach is helpful to get a feeling for the spatial separation of the measurement positions and the possibilities of this method to distinguish between different radial positions. It should be recalled that the data presented in this section is derived from spectroscopic measurements. It was shown in chapter 3 that certain spectral features are linked to a certain electron temperature range. This knowledge was now used to locate the spectral features on the radial grid by using the electron temperature profile as a mapping device. The radial scatter of the data for each measurement

location is therefore linked to differences in the electron temperature profiles of the evaluated time intervals.

Figure 5.7a shows that the phase lags at the three measurement positions are clearly distinguishable. There is nearly no overlap between the phase lags evaluated at the different measurement locations, proving the validity of the method. The picture for the relative amplitude profile shown in figure 5.7b looks somewhat different. The relative amplitude was defined in section 4.3.1 by $A_{rel} = A_W/b_W$, with A_W being the amplitude of some tungsten related quantity and b_W being the background value of that quantity. The tungsten related quantities used in this work are the tungsten concentration and the radiation intensity emitted by tungsten. The radial profile of the relative amplitude does not show such a distinct separation between the three measurement locations. It shows a trend of higher values when approaching the ETB, but the overlap between the observational locations is still considerable. Especially the relative amplitudes at the pedestal top and at mid-radius positions are nearly indistinguishable. However, the aim is not to compare the data at the various positions to each other. Quite on the contrary, the aim of this investigation is to compare the influence of the independent variables gas puff and upper triangularity on the evaluated quantity at each position separately. An influence of the independent variables should show in trends which would be visible in the data set gathered at each measurement position. The search for these trends is performed in the following sections.

Looking at figures 5.8a and 5.8b which show the relation between the phase lag and the two independent variables gas puffing and δ_{upper} , it is astonishing to find none. The phase lags at the three different observation locations are clearly distinct from each other, with the phase lag at the ETB being somewhere around 10 ms, at the pedestal top around 17 ms and at mid-radius being approximately 26 ms. This gives confidence in the accuracy of the measurement and the evaluation. However, none of the phase lag data sets, irrespective of its observation location, show any relation between phase lag and the independent parameters gas puffing and upper triangularity. Taking into account the results from the STRAHL modeling, it must be deduced that, if there should be any changes in the radial transport parameters, they must be so small, that they are not detectable with this experimental method. And the accuracy of the method is, especially for the observation position at the pedestal top, high, being in the range of ≈ 2 ms. This high accuracy at the pedestal top position is owing on the one hand to the lack of ELM-signatures in this signal and on the other hand to the still high modulation amplitude which has not been damped so strongly as compared to the signal at mid radius. But not even this signal exhibits a clear trend which could be interpreted as a change of the radial transport parameters. It should be kept in mind that the evaluation of the phase lag shows only a very low sensitivity to changes in parallel transport in the SOL.

Coming now to the interpretation of the relative amplitude data shown in figures 5.8c and 5.8d. The scatter of A_{rel} is much higher than of the phase lag discussed in the previous paragraph. However, it is still possible to distinguish between the observation position in the ETB and the locations at the pedestal top and at mid-radius. The latter are very close to each other since most of the amplitude damping occurs in the ETB with its reduced diffusivity. Beyond the pedestal top the background tungsten concentration is nearly flat. Even though, also these data sets show no correlation to the independent variables. The STRAHL predictions proposed a strong influence of the inward pinch, v_D , and the pedestal top diffusivity, D_{max} , on the relative amplitude. Despite the strong scatter of the data a change of these two quantities can be negated. It is especially astonishing that the upper triangularity shows no detectable signs of interference with the relative

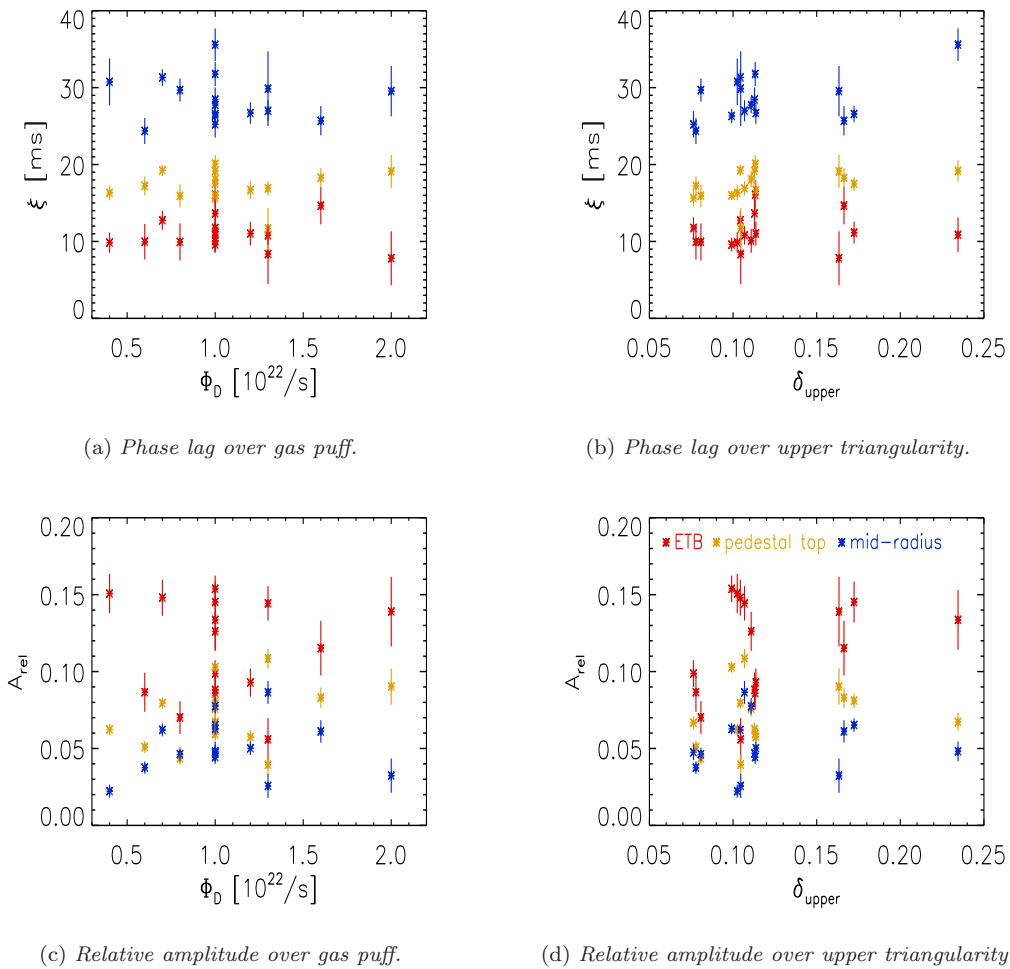


Figure 5.8: Phase lag and relative amplitude as functions of the parameters gas puffing and upper triangularity. The color coding refers to the different positions inside the plasma, at which the data was gathered. Red: ETB, orange: pedestal top, blue: mid-radius

amplitude, even though it does slightly increase the particle confinement for deuterium (n_e rises by 10-15% between low and high δ_{upper} at constant gas puffing).

The data from the phase lag as well as from the relative amplitude both point in the direction of constant radial transport parameters. On the other hand, both observables are rather insensitive to changes in parallel transport in the SOL. Even drastic changes of this transport parameter would remain undetected by this observational method.

5.2.1 Edge Profiles and their dependence on Gas Puff and Triangularity

The data presented in previous studies [17,40] suggests that the radial impurity transport in the ETB is governed mainly by neoclassical transport phenomena. The impurity fluxes caused by classical and neoclassical transport are mainly functions of the spatial derivatives of the ion temperature and density profiles as was laid out in section 1.3.1. Unfortunately, none of the experiments performed in this study has a complete data set of ion temperature and density profiles in the edge region. The edge charge exchange spectroscopic diagnostic was defective during the 2009 campaign, leading

to the lack of edge ion temperature profiles. The experiments from the 2011 campaign lack the edge electron density information, since the lithium beam diagnostic was not functional, when the experiments presented in this study were performed. Nevertheless, the little data there is will be presented in this section.

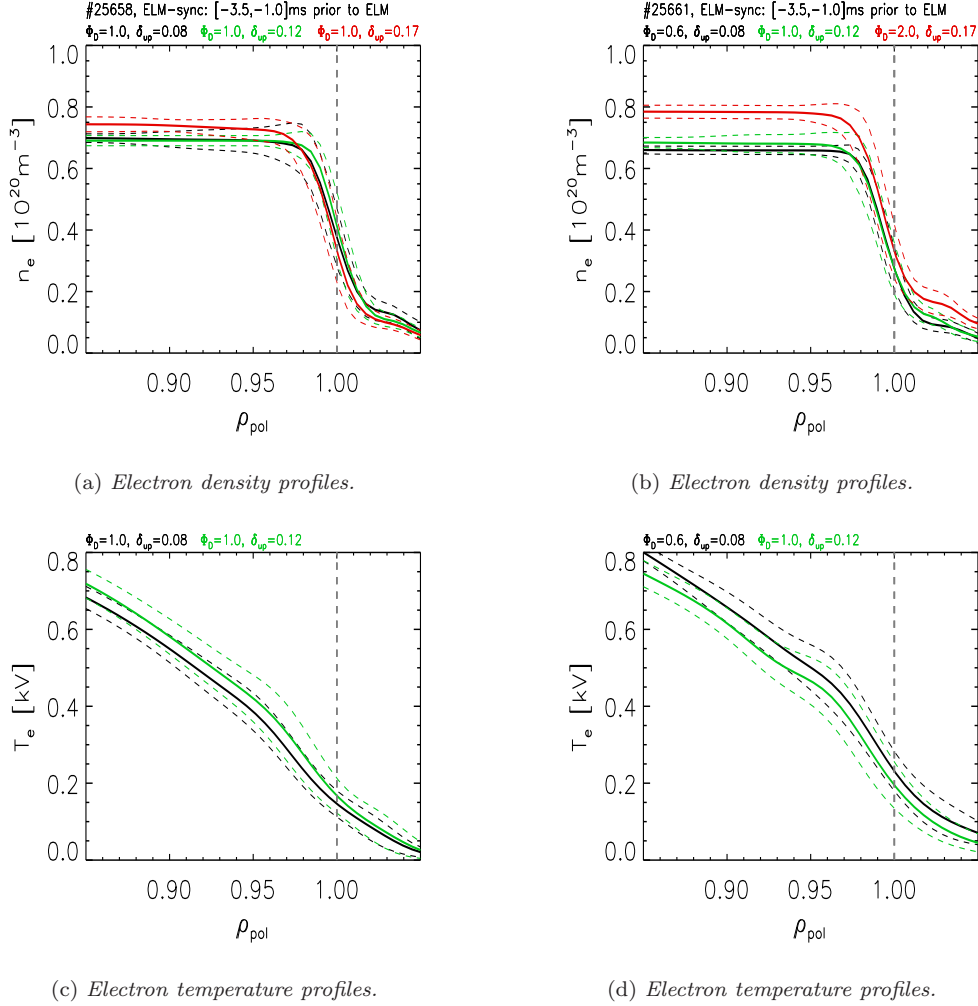


Figure 5.9: Electron density and temperature profile at the plasma edge. The data presented here is taken from the Integrated Data Analysis (IDA) diagnostic. The electron temperature profile is not plotted for the highest δ_u , since the ECE-diagnostic suffers from high density cut-off. The W_{mhd} (energy stored in the plasma) is practically identical in both discharges for the low and medium triangularity cases and differs slightly for the high triangularity configuration: #25658: 0.63 MJ, #25661: 0.59 MJ. The gas puffing rates are given in $10^{22}/s$.

The focus is on the two discharges #25658 and #25661. These two discharges cover the main part of the parameter space scanned in this work (please refer to figure 5.1). As mentioned above, there is no ion temperature information available for these discharges, so only the electron temperature is shown. Before going into the interpretation of the plots some explanations are necessary. The edge profiles shown in figure 5.9 are ELM-synchronized. This means that they are the average over several tens of single profiles found in a certain time interval with regard to the ELM onset. The ELM-synchronization is inevitable in order to be able to compare the edge profiles of different plasma configurations. The time interval which was used to perform the ELM-synchronization is

$[-3.5, -1.0]$ ms prior to the ELM onset. For this time interval both quantities, temperature and density, have equilibrated for all tested plasma configurations. It should be noted that there is no temperature profile for the highest triangularity configuration. This is due to the increase in electron density at the edge, leading to the so called high density cutoff for the ECE diagnostic [63]. Nevertheless, the remaining data is sufficient to assess the influence of the gas puffing rate and the triangularity settings on the edge temperature profile.

The graphs on the left hand side of figure 5.9 show the profiles of discharge #25658. This discharge was performed with constant gas puffing rate and 3 triangularity settings. The triangularity has a slight impact on the density at the pedestal top and further inside, with the higher density values for the higher triangularity setting. Regarding neoclassical drifts (see eq. 1.19), the absolute value of the density is not so important, but its gradients. There, in the steep gradient region, the triangularity has nearly no effect on the density profiles. All 3 density profiles are well within the 1σ scatter of the data, visualized by the broken lines. The picture for the electron temperature profile looks pretty much the same. At constant gas puff, an increase in triangularity leads to a slightly increased temperature, but the profiles located are within the 1σ scatter of one another. Overall, the triangularity scan does not cause major changes in the edge temperature and density profiles. This must lead to unchanged neoclassical diffusive and convective radial fluxes for the tungsten ions. This interpretation would fit the observation of a virtually constant tungsten concentration throughout the discharge.

Figure 5.9b shows the density profiles of discharge #25661. This discharge was run with 3 different gas puffing levels besides the varying triangularity. The edge profiles are almost identical in the steep gradient region in the case of low Φ_D / low δ_u and medium Φ_D / medium δ_u (black and green curves). The high gas puffing in combination with the high triangularity leads to an increase of the density (red curve). However, even though the density is shifted upwards, its profile's shape is still very similar to the other two. This will become obvious when looking at the maximum gradients (figure 5.10b). With nearly matching density profiles in the steep gradient region for all three cases, there is no room for drastic changes of the neoclassical impurity transport.

To further this point, figure 5.10 shows the time traces of the maximum gradients found in the density and temperature profiles. The time traces are ELM synchronized with the ELM onset at 0 ms. Since the divertor thermo-current was used as the signal for ELM detection, the ELM onset is slightly delayed when compared to the signals of $max \nabla n_e$ and $max \nabla T_e$. This delay does not hamper the evaluation of these time traces in any way. The main statement of this figure is found in the plots on the right hand side (traces of #25661). It supports the findings of the previous paragraph: The maximum gradients of the electron density and temperature are nearly identical in the time span before the ELM, regardless of gas puffing or triangularity. Therefore, significant differences of the radial impurity fluxes due to neoclassical transport in the various plasma configurations tested here are not to be expected.

The data presented so far points strongly towards constant neoclassical impurity fluxes in the ETB, irrespective of the plasma configuration. The expression "constant" in this context refers to the transport parameters found in the period before the ELM onset, in which turbulence is strongly suppressed. Yet, contrary to this finding, the main plasma tungsten concentration shows a strong change between the two plasma conditions low gas puffing / medium gas puffing (#25661 [2.0, 2.7] s and #25658 [2.0, 2.7] s in figure 5.1). The case of high gas puffing must be neglected in this examination due to the lack of electron temperature data. Since the altered tungsten concentration

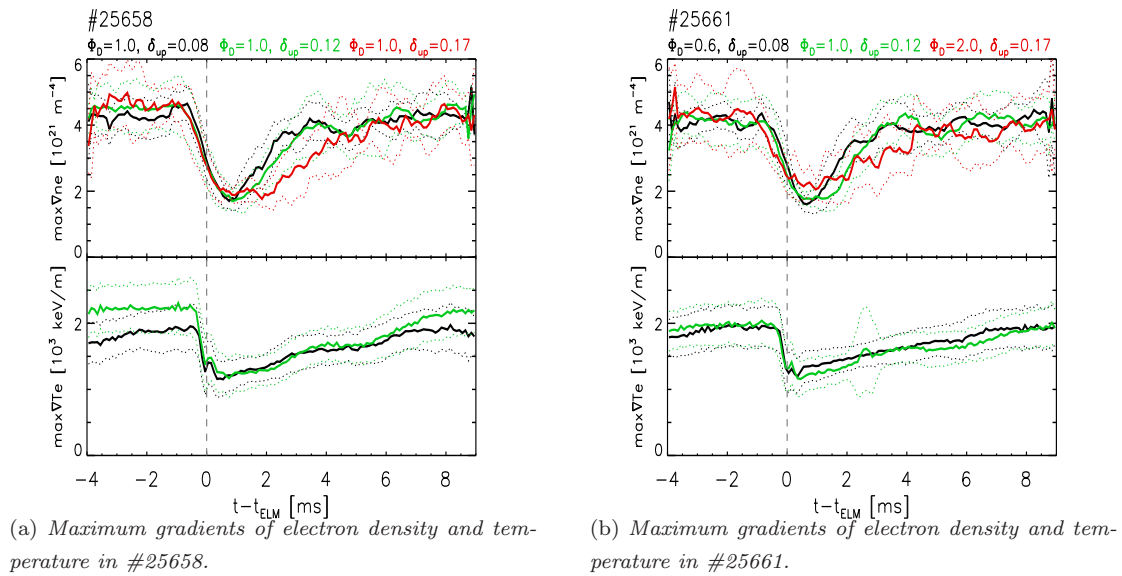


Figure 5.10: *ELM synchronized time traces of the maximum gradients of electron temperature and density. The dotted line shows the 1σ -scatter of the data. A 7-point smooth ($70\ \mu\text{s}$) was applied for better visualization.*

is obviously not due to a change in the neoclassical transport in the ETB, the alteration must have its cause somewhere further outside the main plasma.

Before addressing this question a short summary will be given. At otherwise constant plasma parameters two quantities were altered actively: the upper triangularity and the main chamber deuterium puffing rate. The results of these scans is summed up as following:

- the triangularity has a strong impact on the ELM frequency, allowing for the control of this parameter
- the gas puffing rate has a strong impact on the main plasma tungsten concentration, with the lowest concentrations at the highest puffing rates
- the dependence of the tungsten concentration on the gas puffing is not linked to a certain triangularity configuration
- the same dependence was found in a different set of discharges and it is only partially due to a reduction of the tungsten source
- the ELM frequency does not influence the tungsten concentration
- the result from the observation of the phase and relative amplitude of a modulated tungsten signal suggests constant radial transport parameters for tungsten in the scanned parameter space
- the edge temperature and density profiles do not allow for drastic changes of the radial tungsten transport in the ETB region

These findings lead inevitably to the formulation of a new hypothesis about the cause of this tungsten behaviour. This hypothesis is framed in the following section.

5.3 Simple 0-D Model for W-transport

It was shown in the sections above, that the strong impact of the gas puffing on the tungsten concentration is neither due to changes in the ELM frequency nor to changes in the radial tungsten fluxes of the main plasma. The implications hereof are twofold and lead to the following hypothesis:

- the impurity exhaust by ELMs must not be regarded as diffusive, but turbulent in form of filaments
- the main chamber gas puffing changes the parallel flows in the SOL and with them the parallel loss time of tungsten particles. Shorter parallel loss times lead to lower tungsten concentrations, since more tungsten ions are carried into the divertor sink before they can reach the separatrix.

The first statement of this hypothesis is easily verified. In section 4.3.2 the results of a diffusive ELM model (STRAHL) have been presented. A clear dependence between ELM frequency and main plasma tungsten density emerged from that model. This dependency was not found in the experimental data. Furthermore, the model predicted that the strongest impact on the tungsten density should arise from changes in the ELM diffusivity. However, these changes of D_{ELM} should also leave their footprints in the phase lag profiles. Since there is no evidence for such a change of D_{ELM} in the measured data, it must be regarded as constant. These two points together already contradict a diffusive impurity exhaust by ELMs. Yet, these are not the main reasons to discard the diffusive ELM model. The experimental evidence on the structure of ELMs does not leave any room for doubts about the filamentous nature of these events [64–67]. It was even possible to observe the filaments directly with a new two dimensional electron cyclotron emission imaging diagnostic [68].

Effectively, ELMs can be regarded as small plasma volumes that are being expelled from the main plasma. These volumes carry away not only the main ions but also the impurities. The amount of particles expelled with each ELM, N_{ELM} is related to the ELM frequency by $N_{ELM} \propto 1/\nu_{ELM}$, as has been shown in this study and previous works [19]. Under the assumption that the tungsten concentration in the ELM filaments is equal to the concentration at their originating site, it is now possible to write down a prediction about the tungsten outflux from the plasma due to ELMs:

$$\Phi_W^{out} = c_W \cdot N_{ELM} \cdot \nu_{ELM} \quad (5.2)$$

With the knowledge about the relation between N_{ELM} and ν_{ELM} equation 5.2 reduces to:

$$\Phi_W^{out} = c_W \cdot p_{ELM} , \quad (5.3)$$

with p_{ELM} being the proportionality factor linking N_{ELM} and ν_{ELM} . This means that the tungsten outflux is constant, if its concentration is constant. The proportionality factor also seems to be unaltered by the two parameters, gas puffing and upper triangularity, from which the latter was used to control the ELM frequency.

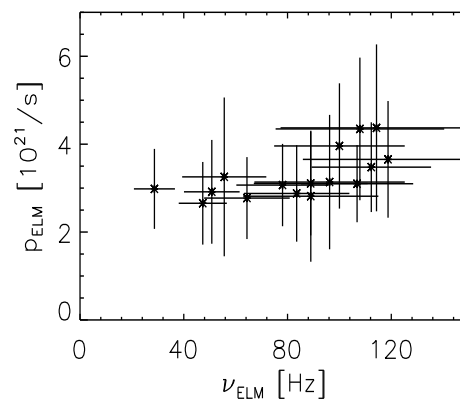


Figure 5.11: *Electron outflux due to ELMs. Same data set as in figure 5.4*

This is visible in figure 5.11 which shows p_{ELM} as a function of ELM frequency for the data set used in figure 5.4. The data points show a slight trend towards higher values in the range above 100 Hz ELM frequency. Yet, taking into account the uncertainty intervals, even the highest values do not deviate from the bulk of the data points. With this said, equation 5.3 leads to the implication, that the type-I ELMs present only a very limited means to control the tungsten outflux. They are, of course, necessary to have a non-diffusive outflux mechanism. Because the lack of such an outflux, would result in much higher equilibrium tungsten concentrations. However, they are not the mechanism which one can use to actively control the tungsten content of the main plasma.

The active control mechanism is found, when the influx of tungsten into the main plasma is considered. For this purpose a simple model of the SOL is presented. Figure 5.12 pictures this model. The model contains the first walls which function as tungsten sources, the divertor which acts as a sink, the SOL itself, and the main plasma. It is aligned along the field lines connecting the outer and the inner divertor. The SOL in this model is divided in two regions for simplicity. One region with zero parallel flow, $v_{||} = 0$ and one region with constant parallel flow, $v_{||} > 0$. The flow pattern in an actual device is, of course, more sophisticated than that. But in general it also has a stagnation point, a region with small parallel flow velocity around that stagnation point and a region with constant, high flow velocity in the rest of the SOL [69]. The stagnation point at AUG is located slightly below the midplane on the LFS. The driving mechanism for the flows is the pressure gradient between the stagnation point and the divertor sink. The origin of the pressure maximum at the stagnation point can be a localized inter-ELM particle loss from the main plasma by blobs [70] or an externally applied gas injection. However, these considerations are far from the scope of this SOL-model.

The main functionality of the SOL is the separation of the main plasma from the wall. Particles eroded from the wall have to cross the SOL of width d in order to enter the main plasma. In this model the eroded particles are assumed to have, at the moment of erosion, only a velocity component $v_{\perp} > 0$ which is perpendicular to the field lines of the SOL. This is of course another simplification, since the velocity of the eroded particles is a distribution over a wide range of angles and velocities. The main assumption of the model is, that the velocity vector of the eroded particles will change from strictly perpendicular ($\vec{v}_i = (v_{\perp}, 0)$) in the absence of parallel flows to a superposition of \vec{v}_i with the parallel velocity of the SOL plasma ($\vec{v}_f = (v_{\perp}, v_{||})$). It should be noted that v_{\perp} does not stand for the initial velocity of the neutral tungsten atoms, but for an averaged perpendicular velocity of the tungsten particles. The aforementioned superposition must happen on time scales smaller than the time needed to cross the SOL.

To check the feasibility of this assumption some calculations have been performed [71]. The calculations included a model for the ionization/recombination of the tungsten atoms and ions and a Coulomb-collision model to investigate the behaviour of the tungsten atoms embedded in a background plasma. The plasma parameters in these calculations were tuned to typical values found in the AUG SOL: $T_e = 10 \text{ eV}$, $n_e = 0.8 \cdot 10^{19} \text{ m}^{-3}$. Also a small amount of light impurities was added. The whole background plasma, including the light impurities was then given a certain, directed bulk velocity, while the tungsten atoms were started with an isotropical velocity distribution. The calculations showed that the tungsten atoms were quickly ionized and then accelerated by ion-ion collisions to the velocity originally given to the background plasma. The time to reach the velocity of the background plasma was below 1 ms, a value which is much shorter than the $\approx 10 \text{ ms}$ the tungsten needs to cross the SOL to reach the main plasma. Therefore it was concluded, that

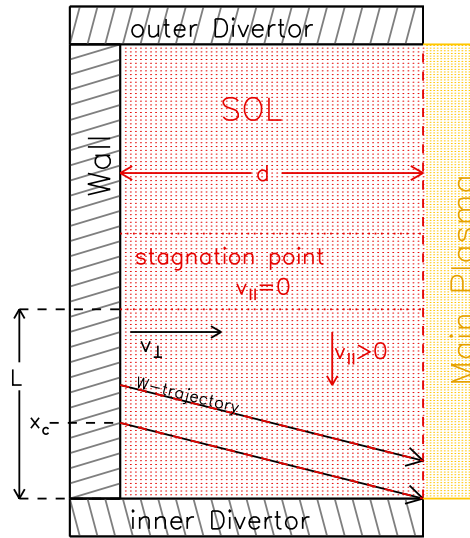


Figure 5.12: *SOL model with walls, divertor and main plasma. The model is aligned along the field lines of the SOL which connect the outer and the inner divertor. Two trajectories of sputtered tungsten atoms are also added.*

the tungsten ions would indeed be carried away by the flows in the SOL.

This SOL model allows now to write down the equation for the tungsten influx to the main plasma:

$$\Phi_W^{in} = \Phi_W^{sp} + \Gamma_W^{er} \cdot \frac{L - x_c}{L} . \quad (5.4)$$

In this equation Φ_W^{sp} stands for the influx of tungsten eroded at and around the stagnation point. Without a parallel flow to carry away the tungsten towards the divertor most of the particles eroded in this section of the wall reach the main plasma. In this equation Γ_W^{er} is the tungsten erosion rate from the part of the wall where the parallel velocity is not equal zero. However, the particles eroded outside the $v_{||} = 0$ area will only partially cross the separatrix, since particles eroded closer to the divertor will reach the divertor before reaching the main plasma. In this model it is easy to calculate the critical distance x_c to the divertor, below which the tungsten is flushed into the divertor:

$$x_c = t_c \cdot v_{||} = \frac{v_{||}}{v_{\perp}} \cdot d , \quad (5.5)$$

with $t_c = d/v_{\perp}$ being the time needed to cross the SOL. Replacing x_c in equation 5.4 Φ_W^{in} becomes a function of the parallel and perpendicular velocities of the eroded tungsten particles in the SOL:

$$\Phi_W^{in} = \Phi_W^{sp} + \Gamma_W^{er} \cdot \frac{L - \frac{v_{||}}{v_{\perp}} \cdot d}{L} . \quad (5.6)$$

In the case of an equilibrated plasma (on time scales $> 1/\nu_{ELM}$) the tungsten influx balances the tungsten outflux:

$$\Phi_W^{in} = \Phi_W^{out} . \quad (5.7)$$

With equations 5.3 and 5.6 it is now possible to derive a prediction for the tungsten concentration:

$$c_W = \frac{\Phi_W^{sp}}{p_{ELM}} + \frac{\Gamma_W^{er}}{p_{ELM}} \cdot \frac{L - \frac{v_{\parallel}}{v_{\perp}} \cdot d}{L}. \quad (5.8)$$

Several implications follow from 5.8. One is that, as long as there is tungsten erosion at the wall close to the stagnation point the tungsten concentration cannot be reduced to zero.

The important implication for this study is, however, the linear dependence of the tungsten concentration on the parallel flow velocity in the SOL. The simple model presented here is not able to directly treat the influence of the gas puff applied in the experiments. Nevertheless, the data gathered during this study points strongly towards a connection between gas puffing rate and parallel flows in the SOL. It was therefore only consequent to probe this hypothesis experimentally by measuring the parallel flows in the SOL.

5.4 Influence of gas puffing on SOL flows

The means to obtain information on the parallel flows in the SOL of AUG were rather restricted. At the time these experiments have been carried out only two devices were available:

- On the LFS a reciprocating manipulator equipped with Langmuir probes
- On the HFS a spectrometer which had LOS running through the SOL.

Figure 5.13 shows the position of these diagnostic tools. It also shows the plasma shaping during the 3 phases used in the experiments. The experiments resemble the discharges presented at the beginning of this chapter. Each discharge has three triangularity steps, each marking one phase. Besides the triangularity, the gas puff also varies for two discharges in each phase, while it is kept constant over the full time span of another discharge. The respective time traces are drawn in figure 5.14. The tungsten concentration shows the same dependency on the gas puff as in previous experiments. It should be noted, that between the experiments presented in figure 5.1 and these discharges, the ICRH antenna limiter shape was modified in order to reduce the tungsten erosion at the limiter. Seen in this light, the dependence of the tungsten concentration on the gas puff is so fundamental, that it is not disturbed by a mere change of wall shaping. However, the partially new wall setting seems to have an influence on the ELM behaviour. It so happens that the gas puff has a stronger impact on the ELM frequency in these

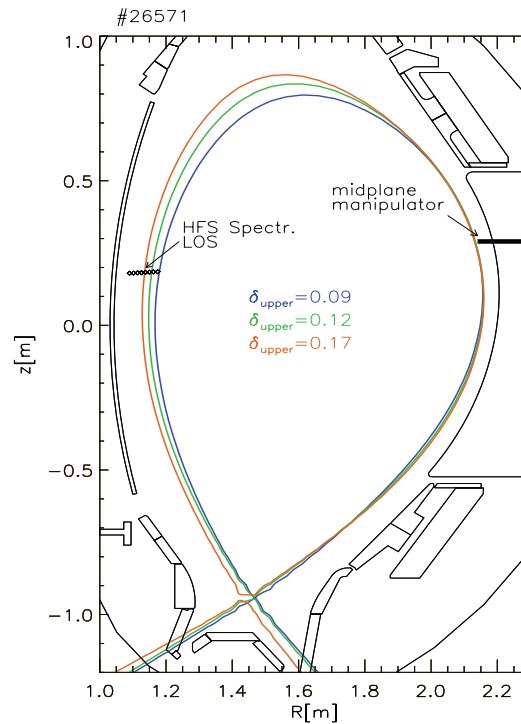


Figure 5.13: *The separatrix position for the 3 triangularity configurations. The diagnostics used to monitor the SOL flows are also drawn (HFS spectroscopy and midplane manipulator).*

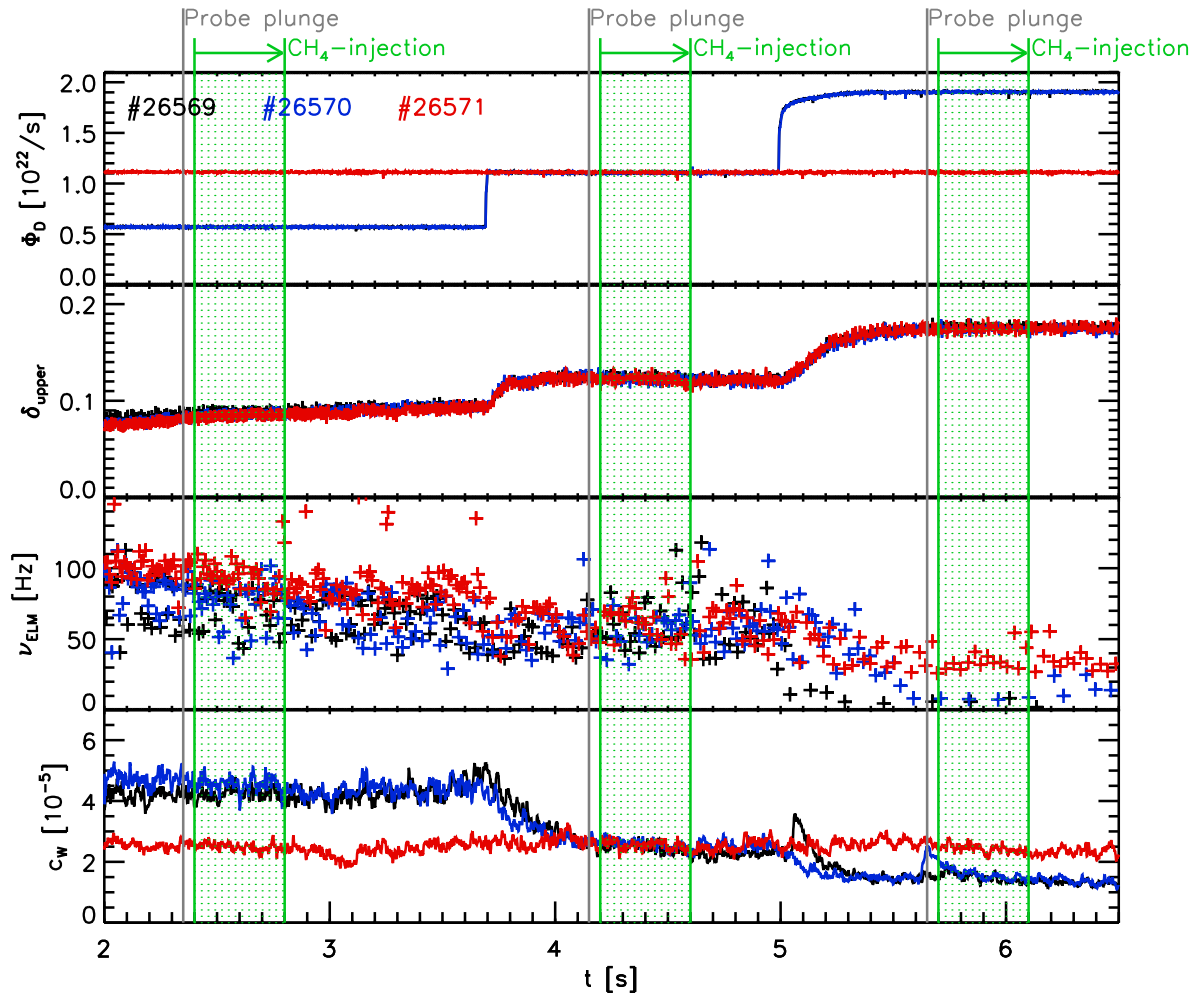


Figure 5.14: Time traces of various plasma parameters. The time points of the Langmuir probe plunges are represented by vertical grey lines, while the time spans of the CH_4 -injections are marked by the green shading. It should be noted that for #26569 and #26570 the automatic ELM detection fails for $t > 5.4$ s.

experiments than observed in the discharges presented before. The discharges #26569 and #26570 were run with a different gas puff level in each phase of the experiment. Since the gas puff and triangularity are both ramped up during these discharges, the ELM frequency is nearly equal for phase one and two of these discharges. That is due to the rather opposite impact of these two parameters on the ELM frequency - higher gas puff leads normally to higher ELM frequency, while higher upper triangularity reduces it. In discharge #26571 the gas puff was constant and the sole influence on the ELM frequency was exerted by the upper triangularity. Its impact on the ELM frequency is obvious. On the other hand, the impact of the various triangularity levels and therefore the different ELM frequencies on the tungsten concentration is nonexistent.

These discharges in combination with #26210 and #26211 draw an even clearer picture of the influence of the triangularity, ELM frequency and gas puffing rate on the tungsten concentration. They are also adequate to wipe out the last doubt about the universal validity of these relations, since in these discharges the ELM frequency does change with the gas puffing rate, just as in the discharges

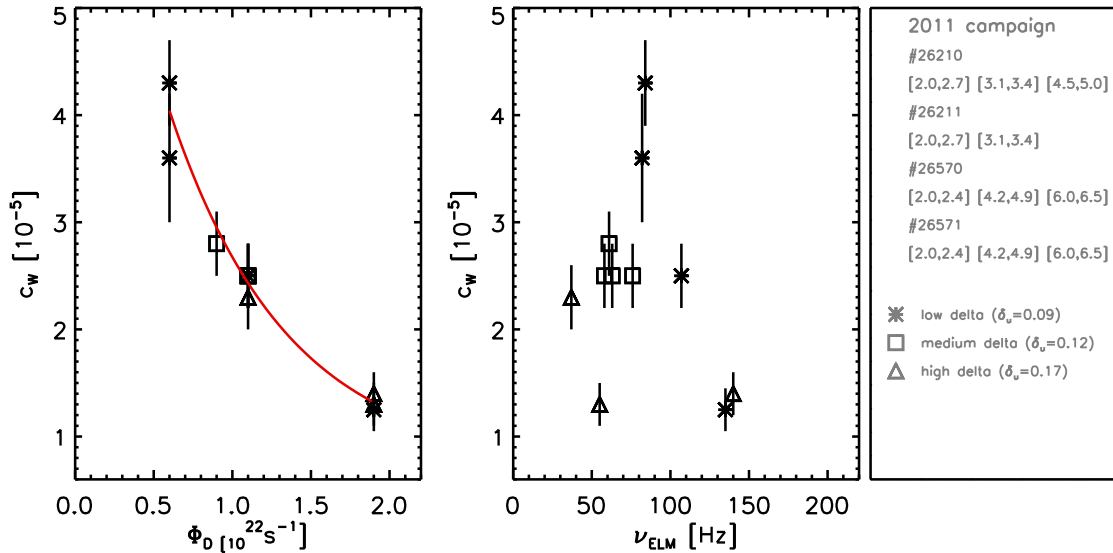


Figure 5.15: Tungsten concentration over gas puffing rate and ELM frequency for the shape optimized discharges. The dependence between the tungsten concentration and the gas puffing rate is obvious and is stressed by the red line which is an exponential fit to the data. The different triangularity values are coded by symbols.

presented in [14] where the ELM frequency was controlled via the gas puffing rate. Therefore, they answer the question, whether or not the discharges from the 2009 campaign were some strange aberration (no impact of the gas puffing rate on the ELM frequency) with a clear no, since the same dependence of the main plasma tungsten concentration on the gas puffing is found here. Figure 5.15 presents the essence of these discharges. While the tungsten concentration shows a very clear exponential dependence on the gas puffing rate, there is no such relation in the plot which shows the tungsten concentration over the ELM frequency. It also shows that the triangularity (symbol coded in this figure) has no impact on the tungsten concentration. From the two independent variables, gas puffing rate and triangularity, only the gas puffing rate has a relevant impact on the impurity content of the plasma. This graph confirms once more the notion, that the ELM frequency is not a significant control factor for the tungsten concentration in the main plasma. Therefore, the focus will now turn towards the SOL flow measurements.

5.4.1 Spectroscopic measurements of SOL flows on the HFS

As aforementioned there were two devices used to obtain information on the flow behavior in the SOL. The following sections will deal with the spectroscopic measurements performed on the HFS. It should be mentioned that the flow of the SOL plasma can not be observed directly spectroscopically. Therefore, a trace amount of CH₄ was injected on the HFS close to the position where the LOS of the spectrometer run through the SOL. The injected CH₄ dissociates and the atomic carbon is then quickly - on scales $\ll 1$ ms - ionized. As soon as the carbon reaches the first ionization stage, its effective cross-section increases drastically. The SOL then imprints its velocity distribution on the carbon ions by ion-ion collisions and the C-ions can be used as a probe for the velocity of the background plasma.

The spectroscopic measurements were carried out on either C¹⁺ or C²⁺. Two suitable spectral lines were chosen for this purpose at 514.1 nm for C¹⁺ and 465.0 nm for C²⁺ in accordance with

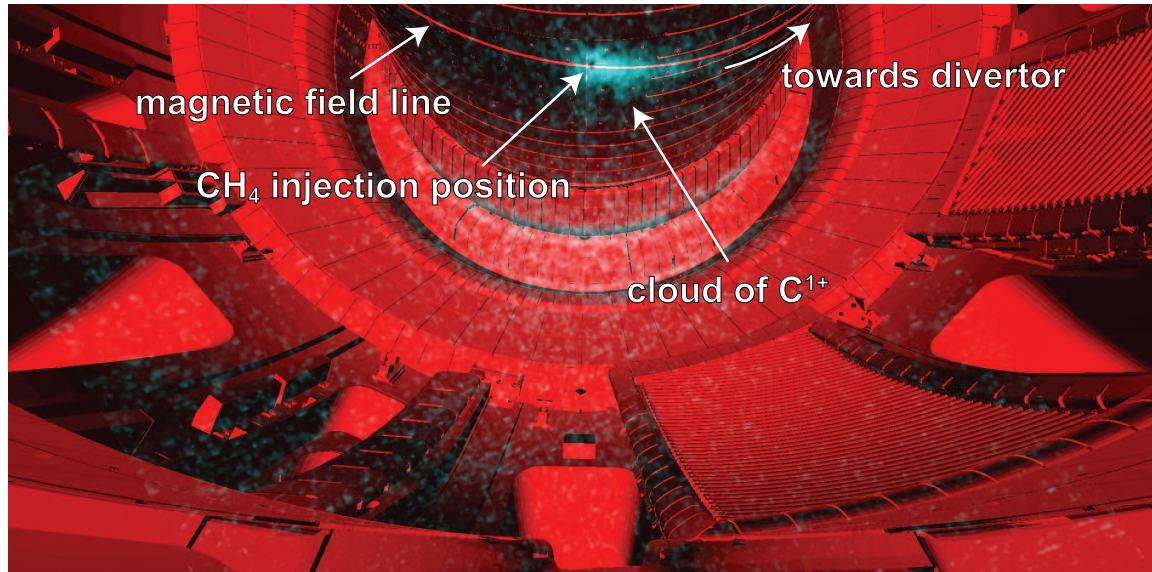


Figure 5.16: CH_4 injection as seen with the fast vertical camera equipped with a C^{1+} filter (514.1 nm). One magnetic field line crossing the nozzle position is drawn in red.

reference [72]. The velocity of these C-ions was then determined from the Doppler-shift of these spectral lines. Figure 5.14 shows not only the time traces of several quantities, but also the time slots during which CH_4 was injected in the plasma. The injection rate was roughly $10^{20}/s$. The low injection rate and the injection position kept its influence on the total carbon concentration in the main plasma below the measurement threshold. In order to better visualize the experimental setup figure 5.16 shows a picture taken with the fast vertical camera overlaid with a CAD drawing of the vacuum vessel. In addition to the vessel structure also one magnetic field line running through the detection volume of the spectrometer is drawn. The camera was equipped with a narrowband filter centered at 514.0 nm which corresponds to the wavelength position of the chosen emission line of C^{1+} . Equipped with this spectral filter, the camera delivers a perfect picture of the carbon plume. It is easily visible that the plume has an elongated shape aligned with the magnetic field lines. This elongated shape results from the collisions between the carbon ions and the background ions of the SOL. Unfortunately, as it turns out, C^{1+} is a very unfavorable ion to probe the SOL in AUG. Its life time in the SOL plasma with its electron temperatures well above 10 eV is way too short for the background plasma to fully imprint its velocity distribution anywhere but in the very far SOL. Therefore, all velocity profiles which will be presented in the following sections are derived from the spectra of C^{2+} -ions. These ions offer a good probing ability in the electron temperature range $10 \text{ eV} < T_e < 20 \text{ eV}$. Their probing abilities in the rest of the SOL plasma are, however, rather restricted. Nevertheless, as will be shown, the data gathered offers a good insight into the SOL behavior at various gas puffing rates.

The only discharge for which the spectrometer was set to the C^{2+} line is #26569. The camera connected to the spectrometer was run with a framing time of 7.5 ms which is too long to exclude ELMs from the evaluation. Surely, this introduces a slight uncertainty in the velocity profiles, but keeping in mind, that the first two phases of #26569 exhibit nearly identical ELM frequencies, it does not diminish the validity of the results. For each phase of the discharge a 200 ms time interval was used to determine the velocity profile from the spectra of the 8 LOS. The evaluated time intervals

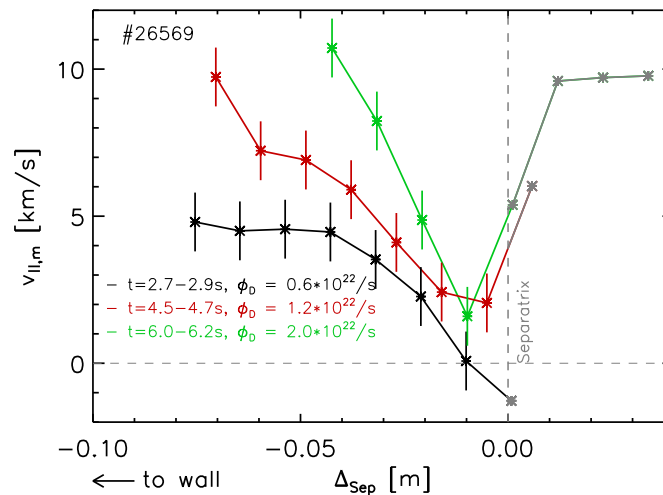


Figure 5.17: Measured parallel velocity at the HFS. Determined from the Doppler shift of a C^{2+} line emission at 465 nm. The plasma moves by ≈ 2 cm towards the wall in the last evaluated phase.

are centered at the end of each CH_4 injection. This guarantees the strongest spectral signals, since there is a considerable delay between the opening of the CH_4 -valve and the appearance of the CH_4 in the plasma. In order to ensure comparability of the velocity profiles for the three phases of the discharge, the separatrix position offers the best basis for a coordinate system.

Figure 5.17 shows the velocity profiles with the x-axis zero at the separatrix. The results are obvious. An increased gas puffing leads to a higher flow velocity in the SOL. The only region exempt from this effect is very close to the separatrix, but there the measured velocity is close to zero for all three gas puff levels anyway. The velocity profiles of the first two phases cover almost the entire SOL, only ≈ 3.5 cm of radial SOL eluding the measurement in the lowest gas puff phase. By experiment design the separatrix moves closer to the wall with increasing triangularity which is unfortunate because it reduces the observed region of the SOL by almost 50% for the highest gas puff phase. Nevertheless, the profiles leave no doubt about the influence of the gas puff on the SOL velocity.

Doubt might arise when the question of absolute numbers is raised. As aforementioned, the velocities are deduced from spectral lines emitted by C^{2+} ions. These ions have a certain velocity profile imprinted on them by the background plasma. However, the imprinting process takes a certain time and this time is in competition with the time needed to ionize C^{2+} to C^{3+} . As the following calculations will show, the time to fully imprint the velocity profile of the background plasma on the C^{2+} ions is longer than the ionization time of these ions. This holds for regions with $T_e > 20$ eV which is a large portion of the SOL. It means that the velocities deduced from the C^{2+} spectra are a lower boundary and the actual velocity of the background plasma is indeed higher.

A reconstruction of the original SOL velocity profile is attempted in the following. Before describing the reconstruction it is, however, helpful to investigate the process of velocity transfer from the SOL plasma to the carbon ions. This investigation is performed on the model already used to calculate the acceleration time of tungsten in a moving background plasma. In the model, the carbon starts as a population of neutral atoms with a quite low temperature ($T_C = 0.5$ eV) and no bulk velocity. This population then breaks up into the populations of the various ionization stages

which are accelerated by ion-ion collisions with the background plasma. For the case regarded here, of course, only the C^{2+} population is of interest. The background plasma has a predefined bulk velocity parallel to the magnetic field, contains some light impurities and is set to temperatures and densities usually found in the SOL of AUG ($10 < T_e < 100$ eV, $0.5 < n_e < 1.0 \cdot 10^{19} \text{ m}^{-3}$). With a certain set of these parameters the simulation is run until the velocity distribution of the C^{2+} ions shows no more development. This point is usually reached in well under 1 ms, but the simulations are carried on until 2 ms to pay tribute to the statistical nature of the model. The result is the parallel velocity distribution of the C^{2+} ions which is directly related to the Doppler shift measured in the experiment.

Figure 5.18 shows the influence that the temperature of the background plasma exerts on the velocity distribution of the C^{2+} ions. A temperature of 10 eV allows the C^{2+} population to fully equilibrate its temperature and bulk velocity with the background plasma which has given a bulk velocity of 11.2 km/s for these calculations. In the case of the $T_e = 40$ eV equilibration is not achieved. This is visible in the shape of the velocity distribution. While the velocity distribution of the C^{2+} ions at 10 eV is Gaussian with a shifted center - shifted by the amount of the parallel velocity -, the distribution at 40 eV shows a strong distortion from a Gaussian shape, a clear sign of a non-equilibrated population. Furthermore, the center of the distribution does no longer coincide with the parallel velocity, but is located at a smaller value. Both effects are due to the very short life time of the C^{2+} ions in this environment. It is the latter of the two effects which will be further investigated.

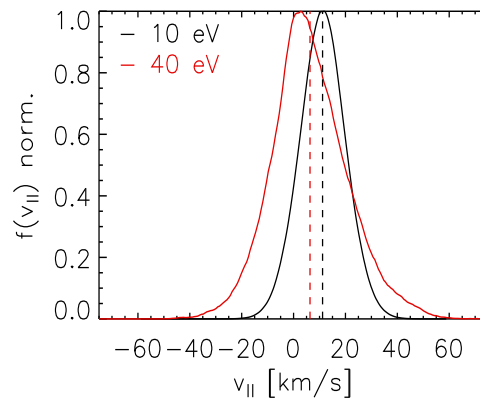


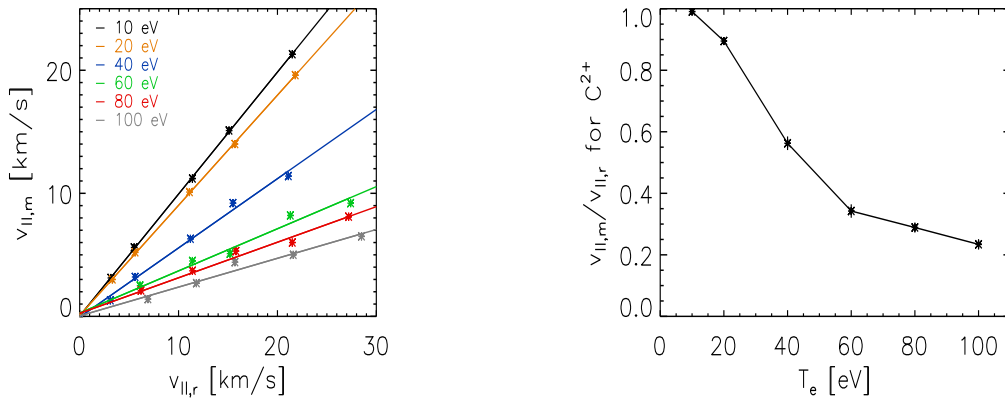
Figure 5.18: *Normalized velocity distributions of C^{2+} ions at 10 eV and 40 eV electron temperature. The distribution at $T_e = 40$ eV clearly diverges from a gaussian shape.*

In order to reconstruct the actual parallel velocity of the background plasma from the Doppler-shifted spectra of C^{2+} -ions at temperatures beyond 20 eV two relations have to be known:

- dependence of the measured velocity on the actual velocity at a given temperature
- dependence of the measured velocity on the temperature at a given actual velocity

For better understanding it should be mentioned that the measured velocity, $v_{||,m}$, was defined as the center of the velocity distribution of the C^{2+} ions. The aforementioned dependencies were worked out in a series of simulations with the model described above. They were always run at a fixed electron density ($0.8 \cdot 10^{19} \text{ m}^{-3}$), while temperature and bulk velocity were scanned.

Figures 5.19a and 5.19b present the results. The linear dependence of $v_{||,m}$ on $v_{||,r}$ at a fixed temperature, visible in figure 5.19a, is undeniable. The little scatter there is in the data points is due to the statistical nature of the model. Next, a linear fit was applied to each data set at a given temperature. Naturally, the linear fit gives error estimates which are all well below 10% for the ratio $v_{||,m}/v_{||,r}$. This shows the good agreement with the linear model. Actually, taking into account that we are dealing with non-relativistic velocities, any other relation between $v_{||,m}$ and $v_{||,r}$ at a fixed



(a) Relation between "real" and "measured" parallel velocity at several temperatures.

(b) Ratio of "measured" over "real" parallel velocity as a function of temperature.

Figure 5.19: Dependencies between "measured", $v_{||,m}$, and "real", $v_{||,r}$, parallel velocities. Since this is data from a simulation, "real" refers to the parallel velocity of the background plasma set in the simulation and "measured" to the center of the velocity distribution of the C^{2+} -ion population.

temperature would have been surprising. This linear dependence is quite fortunate, since it makes it very easy to deduct the influence of the temperature on the ratio $v_{||,m}/v_{||,r}$ - representing one of the last steps on the way to the reconstruction of the actual SOL velocity.

Figure 5.19b displays this influence. It was mentioned in the previous paragraph that each point in this figure is the result of a linear fit to the respective data set in figure 5.19a. Therefore, each data point is also afflicted with an error bar which is, however, smaller than the marker symbol for most of the data points. Including one last assumption, these data points allow now for the reconstruction of the original SOL flow velocity. The assumption concerns the electron temperature profile in the SOL. Lacking any measured data on that quantity at this HFS location, a very simple T_e -profile is assumed: linear increase from 10 eV at the wall to 100 eV at the separatrix. The value of 100 eV at the separatrix is justified by Thomson-scattering measurements and is in general the value expected in AUG at the separatrix of H-mode discharges. The temperature at the wall is an estimate based on Langmuir-probe data from the LFS. The T_e inbetween these two points is very badly diagnosed on the HFS and no measured data is available. Nevertheless, lacking more precise data, the assumed temperature profile will be used as a zeroth order assumption. This temperature profile allows now to assign a distinct electron temperature to each spectroscopic measurement location in the SOL. From there it is only a small step to multiply the spectroscopically determined parallel velocity of the C^{2+} ions with the according inverse of the ratio $v_{||,m}/v_{||,r}$ to obtain the original SOL parallel velocity. As the discharge features 3 different separatrix positions on the HFS, the reconstruction in each phase is assigned its own SOL temperature profile.

The results of this reconstruction are depicted in figure 5.20. The overall conclusion is unaltered. The higher the gas puffing rate the higher the parallel velocities become in the SOL. Of course, the shape of the velocity profiles changes slightly, showing a peaked profile instead of a flat one in the far SOL (see figure 5.17). But the profiles are well separated from each other and are even more consistent, since the outlier in the red profile is moved back in line.

It is understood that the author is aware of the many simplifications and assumptions that were

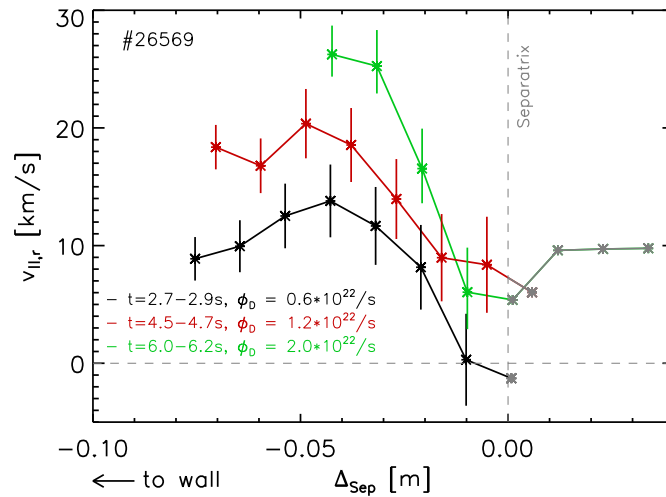


Figure 5.20: Reconstructed parallel velocity at the HFS. Due to the movement of the separatrix between the three phases of the discharge, each reconstructed velocity profile was calculated with its distinct electron temperature profile.

used during this reconstruction. For example, the model does not account for the perpendicular movement of the carbon atoms and ions in the SOL, or even for the dissociation process of the CH_4 molecules. The lack of perpendicular movement leads to calculations which were performed each at constant temperature and density. To check the validity of this assumption two time scales have to be compared. On the one hand there is the time needed for the C^{2+} -ion population to reach the final velocity distribution, $\tau_{v,f}$. On the other hand the particles do move perpendicularly in the experiment which leads to the time needed to cross the SOL, τ_x . If $\tau_{v,f} \ll \tau_x$ the assumption is valid. $\tau_{v,f}$ can be assessed from the the calculations themselves and is in the range of 0.2 – 0.3 ms. The time to cross the SOL is somewhat harder to estimate since this experimental data on carbon is lacking. It is necessary to bridge this gap by looking at tungsten, for which this number is available. This is possible since both elements show roughly the same charge to mass ratio in the SOL and should therefore behave quite similarly. For C^{1+} and C^{2+} this ratio is 0.08 and 0.17 respectively, while it ranges from 0.05 for W^{10+} to 0.11 for W^{20+} , this span representing the ionization stages of tungsten usually prevailing in the SOL. From the measurements with the modulated ICRH power it followed that $\tau_x \approx 10\text{ms}$ for tungsten and, following the above argumentation, also for C^{1+} and C^{2+} . The radial velocity of the carbon ions is then in the range of $\approx 10\text{m/s}$, a value in agreement with previous findings [73]. Thus, $\tau_{v,f} \ll \tau_x$, and therefore it is justified to perform the calculations at fixed plasma parameters assuming a stationary - in radial direction - carbon population.

The above statement implies, that neutral carbon has to be able to reach any part of the SOL. This immediately leads to the problem of the CH_4 dissociation process in the SOL plasma, a problem tackled by earlier studies ([73–76] and references therein.) Those studies present a very complex dissociation behaviour. The breakup of the CH_4 -molecule is not linear, in the way that, once ionized, it stays electrically charged until the naked carbon ion is exposed. It is more a process of frequent ionizations and recombinations of the CH_4 -remnant molecule, leading to neutral molecules even deep in the SOL. Hence, the aforementioned assumption is valid. It follows that the reconstructed

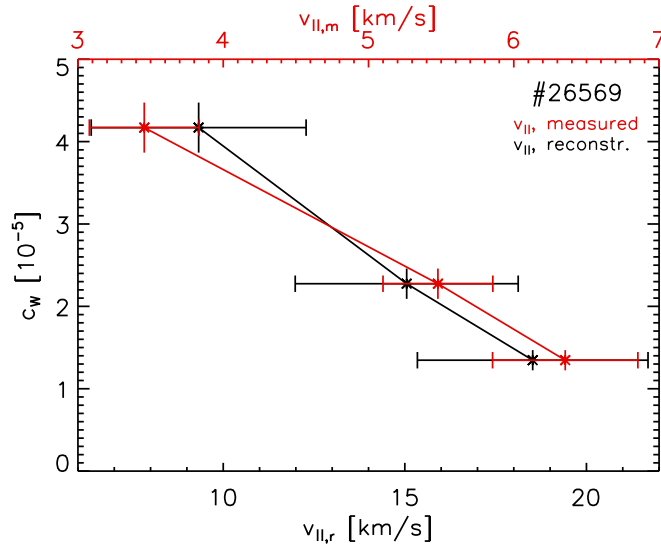


Figure 5.21: Tungsten concentration over the parallel velocity. The red data points are calculated from the measured velocity profiles, while the black curve is the result with the reconstructed velocities.

velocity profiles give a sufficiently accurate picture of the actual flows in the SOL on the HFS.

With this said, it is possible to deduct one last statement from these measurements. This statement refers to the relation between the tungsten concentration and the SOL flow velocity. The tungsten concentration is known and constant in each of the three phases of the discharge (see figure 5.14, #26569). The SOL flow velocity is not available over the full SOL profile for all three phases, so only that region will be evaluated, for which data is present for all three gas puffing levels. This part covers the last 5 cm in front of the separatrix which is about 50% of its full extent. In this area of the SOL the profiles are quite steep which makes it necessary to calculate an average parallel velocity for each phase. This is legitimate, since the parallel and perpendicular velocities can be superimposed and it therefore makes no difference if a tungsten particle crosses a SOL with a flat parallel velocity profile or a more sophisticated one.

The outcome of these considerations are visualized in figure 5.21 which shows the tungsten concentration as a function of the parallel velocity in the SOL. It features two evaluations: one with the measured velocities which must be seen as a lower threshold for the parallel SOL velocity, and one with the reconstructed velocity. With only three data points available for each evaluation - only three different gas puff levels were applied - the significance of this evaluation is rather restricted. Nevertheless, the alignment of these three data points strongly supports the hypothesis of a linear dependence between the SOL parallel flow velocity and the tungsten concentration in the main plasma. This linear dependence was one of the predictions derived from the simple SOL-model presented in section 5.3.

It was shown in this section, that it is possible to locally probe the SOL by the injection of methane. The evaluation of the spectroscopic data revealed a clear link between an increased gas puffing and higher flow velocities on the HFS. Even though the absolute numbers might be questionable, the overall trend is unambiguous. The experimental observations agree with a SOL model, in which tungsten is pushed towards the divertor sink by the parallel flows in the SOL. In the face of this data, it was reasoned that the SOL flows are indeed a major lever to control the

tungsten concentration in the main plasma.

5.4.2 Langmuir probe measurements of SOL flows on the LFS

In addition to the spectroscopical measurements at the HFS, the SOL was also observed by Langmuir probes at the LFS. The Langmuir probes are mounted on a reciprocating midplane manipulator which allowed for the direct measurement of the local SOL plasma parameters. To avoid too high heat loads for the equipment this measurement is usually carried out through strokes. One stroke was placed during each phase of the discharges. Figure 5.14 shows the exact timing of the strokes. The innermost point of measurement during each stroke was located about 1 cm in front of the separatrix (#26570, #26571).

The manipulator head was equipped with a Mach probe. This probe consists of several pins located on opposite sides of the probe head. One side is facing upstream, the other side downstream and the alignment is parallel to the magnetic field lines. During the presented experiments, a number of pins on both sides measured the saturation ion current by applying a constant bias voltage to these pins. Two more pins on each side were driven in the so-called swept mode which applies linear voltage ramps on the pins and is used for local electron temperature and density measurements. One full sweep covers the range from -140 V over $+15$ V back to -140 V and takes about 1 ms. However, only the up-sweep from -140 V to $+15$ V allows to determine the local T_e and n_e . Therefore, with one stroke taking about 200 ms, it is ideally possible to obtain 200 T_e and n_e measurements and a continuous Mach profile. Unfortunately, the number of useful T_e and n_e measurements is drastically lower, as will be seen in the following paragraph.

The evaluation of the data started with the exclusion of time segments which were affected by ELMs. Sparking at particular pins also distorts the measurement and the respective data was consequently also ignored during the evaluation. The remaining data allowed then for the determination of Mach-numbers, electron densities and temperatures. The latter quantity, T_e , is determined directly from the characteristic $I(U)$ relationship obtained from the swept pins. This relationship can be fitted by an exponential function, the usual assumption for a collisionless plasma [77]:

$$I(U) = I_{sat} \cdot \left(1 - e^{-\frac{e^-(U-U_f)}{k_b \cdot T_e}}\right), \quad (5.9)$$

where U is the applied voltage. The fitting parameters are the floating potential of the local plasma, U_f , the ion saturation current, I_{sat} and the electron temperature in eV, T_e . The factors e^- and k_b are the electron charge and the Boltzmann constant, respectively.

Figure 5.22 shows the $I(U)$ characteristics of two sweeps. It is obvious, that one sweep is strongly distorted. In order to minimize the uncertainty of the T_e profiles such distorted characteristics were exempt from the evaluation. The undisturbed sweep, on the other hand, is in good agreement with the applied fit model. It is now possible to construct the local T_e profile in the SOL from this data. This information allows now for the calculation of the speed of sound

$$c_s = \sqrt{k_b(T_i + T_e)/m_i}, \quad (5.10)$$

with $T_i = 3T_e$, m_i being the ion mass of deuterons. Combining now the information about the pin area, the ion saturation current and the speed of sound, the local electron density can be calculated:

$$n_e = \frac{(I_{s,u} + I_{s,d})/2}{c_s \cdot A_{pin} \cdot e^-}, \quad (5.11)$$

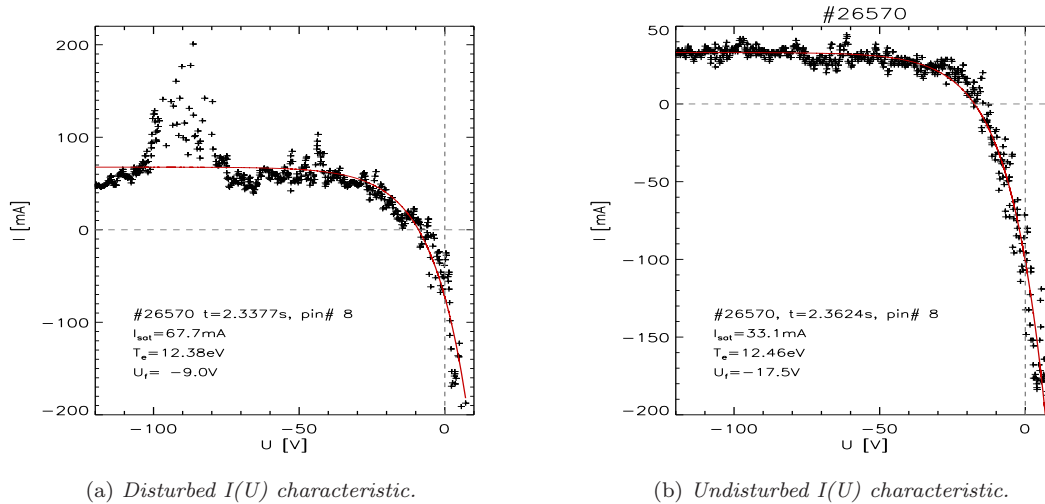


Figure 5.22: Example for the selection process applied to all sweeps. The red line shows the fit result. The fitted ion saturation current is obviously too high for the left sweep.

where $I_{s,u/d}$ are the ion saturation currents on the upstream and downstream side of the probe head and A_{pin} is the area of one pin. The quasineutrality of the plasma allows the calculation of the electron density from the ion saturation current.

After these preliminary considerations the focus turns now to the determination of the Mach-numbers in the SOL. This quantity results from the ratio of the upstream and downstream ion saturation currents by using Hutchinson's formula:

$$M = 0.43 \cdot \ln(I_{s,u}/I_{s,d}) . \quad (5.12)$$

The ion saturation currents were taken from the pins with constant bias voltage. In this respect, these pins yield a higher data output as compared to the swept pins, thus reducing the scatter of the data. This results from the refinement of the data with a moving median which eliminates the spikes from the I_s time traces. The smoothed signals were finally inserted in equation 5.12 and binned on a 2 mm radial grid - the measurements were performed with a radially moving probe head - giving rise to the radial Mach number profile. Having determined the Mach numbers, it is only a small step to obtaining the parallel drift velocity from the relation:

$$v_{||} = M \cdot c_s . \quad (5.13)$$

The determination of the various SOL profiles was carried out on two consecutive discharges (#26570, #26571). These two discharges were identical except for the gas puffing rate. Discharge #26571 had a constant gas puffing rate of $\Phi_D = 1.2 \cdot 10^{22}/s$, while #26570 was run with a certain gas puffing level for each phase of the discharge (see figure 5.14). Figure 5.23 summarizes the profiles resulting from the Langmuir probe measurements for the first and third phase of the discharges. The second phase is identical for both discharges and was therefore left out in this figure.

Figure 5.23 compares the SOL plasma parameters at a given triangularity. Hence, the left and right columns show the SOL profiles at low and high triangularity respectively. The reason for this representation will become obvious as the data is interpreted. The topmost graph shows the electron temperature and density profiles. For the case of the electron temperature, this profile is rather restricted with respect to its radial extent. It was therefore necessary to apply a linear fit to

the T_e -data in order to expand the region in which other plasma quantities could be evaluated, *e.g.* the calculation of n_e needs the input of T_e via the speed of sound. This linear fit is also drawn in the graph besides the data points and shows a very flat temperature profile for both gas puffing rates in the low triangularity case. The stronger gas puffing coincides with slightly higher temperatures for both triangularities, however the scatter in the data is considerable. Surprisingly, even close to the separatrix the temperatures are still well below 20 eV, independent of gas puffing rate or triangularity. This might be caused by a local cooling effect: the valve for the deuterium injection is in the immediate vicinity, toroidally as well as poloidally, of the measurement location.

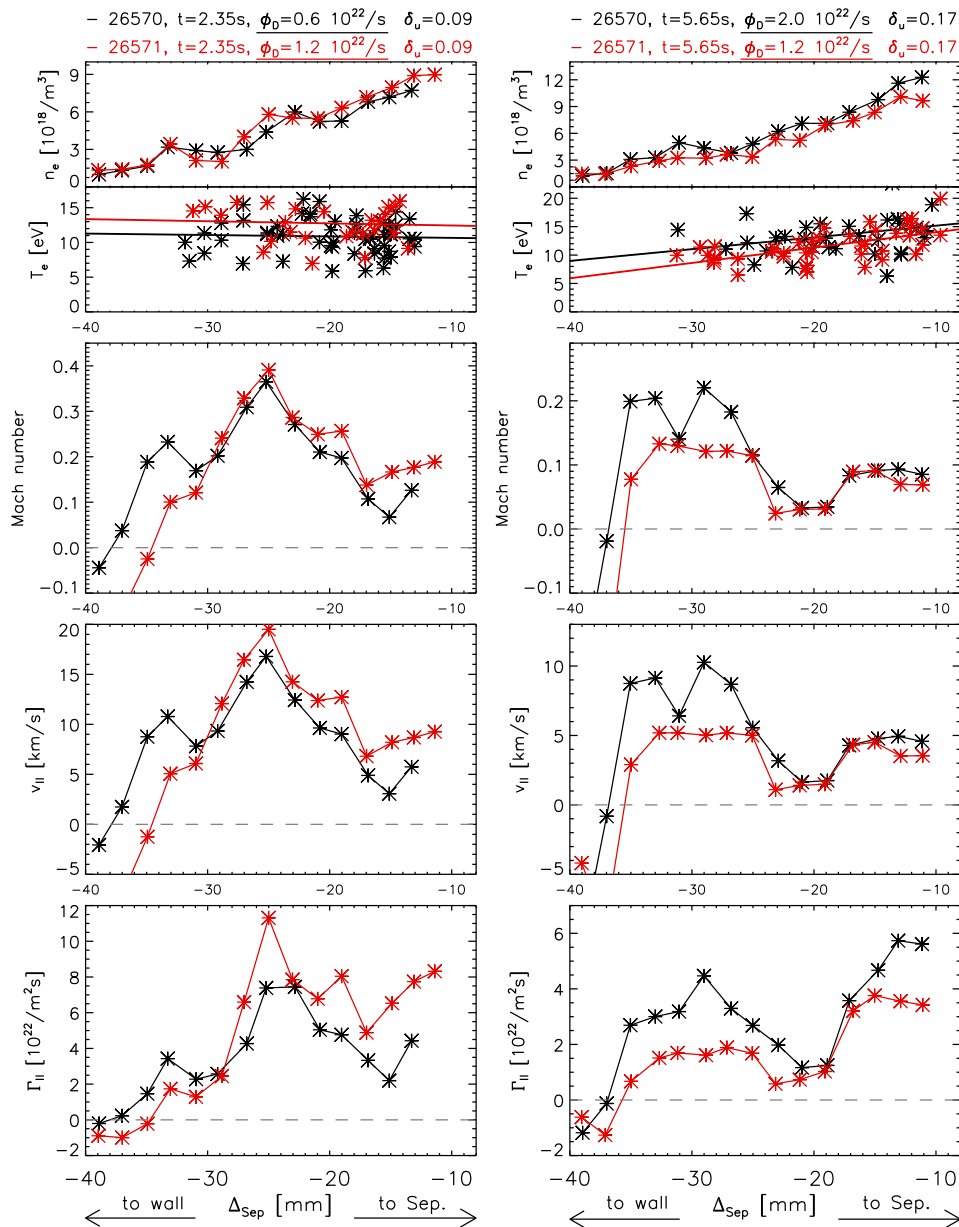


Figure 5.23: Various profiles of plasma parameters in the SOL. The graphs are sorted by triangularity: low triangularity on the left, high triangularity on the right. The interesting independent variable is the gas puffing rate.

The density profiles show a slight dependence on the gas puffing rate. The higher gas puff leads for both triangularities to higher electron densities over almost the entire profile. In the case of constant gas puffing, $\Phi_D = 1.2 \cdot 10^{22}/s$, the n_e -profiles are nearly congruent for the two triangularity cases. It means that this quantity is not affected by the triangularity value.

Coming now to the Mach numbers, this is totally different. Here the triangularity has a tremendous effect. While the Mach numbers for low triangularity are in the range of 0.4 at the maximum, they barely reach 0.2 in the high triangularity case. It is obvious that this effect is not linked to the gas puffing, as in the case of constant gas puffing the difference is even more pronounced. What plays the major role here is the location of the stagnation point. This point is located below the probe position for the low triangularity configuration. It can be thought, that with increasing triangularity this point moves upward, since the plasma is being stretched in z-direction to create the higher upper triangularity (see figure 5.13). If this were the case, this movement of the stagnation point would make it necessary to sort the profiles by triangularity in order to be able to compare the influence of the gas puffing rate on the SOL flows, as has been done here. And this influence is visible, but not very distinct. In the low triangularity case the profiles are almost identical from -30 mm inward with only slightly higher Mach numbers for the higher gas injection. The high triangularity configuration shows a more pronounced influence, but only in the outer half of the SOL. The profiles beyond -25 mm are very close to congruent, with only slightly higher values for the higher gas puffing.

Adding the information on the local speed of sound, it is possible to calculate the parallel velocity profiles. These are plotted in the third graph from top in figure 5.23 and offer some more insight than the Mach numbers alone. The parallel velocity profiles for high and low gas puffing rates are slightly better separated in the low triangularity case, while there is no relative change between high and low gas puffing in the high triangularity configuration. It is interesting to look at the absolute numbers, when comparing the low and high triangularity case. For low triangularity, where the stagnation point is thought to be far away from the probe head, the maximum of the profile reaches almost 20 km/s, a value, that is in the range of the reconstructed velocity profiles derived from the spectroscopic measurements on the HFS. Also the shape of the profile is similar to the one from the HFS, with smaller velocities closer to the separatrix. It is helpful for this consideration to change the x-axis from the metric radial to normalized poloidal flux coordinates. In this system, the peak of both profiles, on the LFS as well as on the HFS, is located at roughly $\rho_{pol} = 1.05$, showing the agreement of both measurements in this aspect. Coming now to the high triangularity case, the highest value for the parallel velocity is around 10 km/s, in spite of the much higher gas puffing. In addition, there is no resemblance between these velocity profiles and the ones determined on the HFS. As mentioned above, this must be interpreted as an effect caused by the upward movement of the stagnation point towards the probe position which was triggered by the increase of the upper triangularity.

The bottom graphs in 5.23 show the parallel particle fluxes for the various gas puffing and triangularity scenarios. Since this quantity results from the multiplication of the velocity and density profiles, it does not offer too much new insight. However, these graphs show a clear influence of the gas puffing levels on this quantity. Higher gas puffing leads to increased parallel particle flux in the SOL, therefore also increasing the drag on the impurities in this plasma region.

Some interpretation of the data presented in 5.23 was already given in the paragraphs above. This paragraph will discuss the open question arising from the Langmuir probe measurements. It

seems, the position of the stagnation point with respect to the probe head has a major influence on the measured parallel velocity. Nevertheless, the examined discharges allowed to compare solely the impact of the gas puffing on this quantity. It is this data, that is in contradiction with the spectroscopic findings on the HFS. A possible explanation is found, when considering the proximity of the gas injection valve and the probe head. The toroidal separation is roughly 25° or 0.9 m with the gas injection site located downstream from the probe position (see figure 5.24), while the poloidal separation is less than 0.3 m. Actually, the poloidal separation is nonexistent, since the injection valve is located deep inside the A-port, and the whole port area acts as a gas source.

With this geometrical setup in mind, the potential paths of the injected gas are traced in a hypothetical way, which unfortunately, is not covered by experimental evidence. The following explanation should be regarded as a gedankenexperiment. One path leads the gas into the main plasma, fuelling it. On the second path the gas does not reach the main plasma but is contributing, after its ionization, directly to the parallel SOL flows. However, in stable discharges the main plasma density reaches an equilibrated value in the end. Therefore, all the gas that enters the reactor vessel and is being ionized adds to the parallel flows in the SOL, either immediately at the injection location or with a detour leading it through the main plasma. The particles, that contributed to the fuelling of the main plasma are expelled at the stagnation point, or in a toroidal view, at the stagnation ring. This causes a higher pressure in this region as compared to other regions in the SOL, thus driving the parallel flows towards the divertor, where pumps create a pressure sink.

The particles that contribute directly to the SOL flows create a second pressure peak at the injection location. The pressure profile along the magnetic field lines which run through this injection area, show two local maxima. Hence, the parallel flows are reduced in the region between these two maxima. If the pressure profile along a magnetic field line would indeed look like that, the Langmuir probe head would be located exactly in this unfavourable region.

It follows from this gedankenexperiment that the parallel velocity measured in this region would have to behave different to the one measured at the HFS, far away from these local effects. And this is exactly what the data shows. At low gas puffing rates, the Langmuir probes measure a certain radial profile of the parallel velocity in the SOL. This velocity profile is a manifestation of the pressure gradient between the local maxima at the stagnation point and in the gas injection region. Since these velocities at the low gas puffing rate agree quite well with the measurements at the HFS, it can be deduced that the local pressure maximum at the gas injection site is rather small. At higher gas puffing, the measured velocity profile is still very close to the one from the low

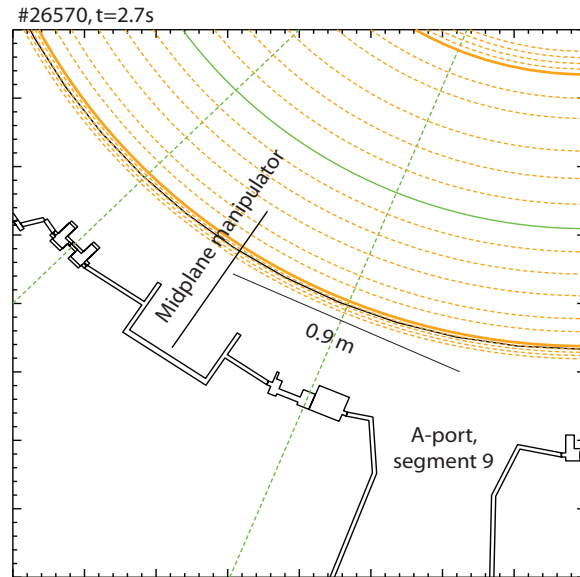


Figure 5.24: Toroidal view of the vicinity of the midplane manipulator on which the Langmuir probes are mounted. The gas is injected into the plasma via the A-ports in segments 5 (not shown) and 9. The separatrix position in the midplane is drawn as a solid orange line.

gas puffing scenario. From the velocity profiles it follows, that within this gedankenexperiment the pressure gradients between the two maxima must be nearly identical for both gas puffing scenarios. It means that the influence of the second pressure maximum becomes stronger, yet at the same time also the value of the local pressure maximum at the stagnation point increases. Globally, the increased pressure at the stagnation point leads to higher parallel velocities, just as measured at the HFS. Locally, at the measurement location of the Langmuir probe on the LFS, the missing effect of the gas puffing level on the parallel velocity would only be natural. If this gedankenexperiment is valid, it must be concluded that the Langmuir probe measurements show only locally restricted effects and therefore, they must be disregarded from a global treatment of the parallel velocity in the SOL.

This section presented the data gathered with a set of Langmuir probes on the LFS. The evaluated data was in contradiction with the measurements on the HFS regarding the effect of the gas injection rate on the parallel flow velocity. It could be argued that this contradiction might be caused by the position of the probe head which is located in the immediate vicinity of one of the gas injection sites. The measurements would therefore have only a locally very limited significance which is not of interest in the global treatment of the tungsten behaviour.

Chapter 6

Conclusion and Outlook

In the framework of this study experiments were carried out which achieved the disentanglement of two usually linked parameters: the main chamber gas injection rate and the frequency of type-I ELMs. This separation was achieved by controlling the ELM frequency via the adjustment of the plasma shape, *i.e.* the upper triangularity. Therefore, it was possible to assess the individual impact of each parameter on the tungsten concentration in the main plasma within the covered parameter space. The results are quite unexpected, since the ELM frequency showed no influence on the tungsten concentration and the sole actuator on this quantity was the gas injection rate. In order to properly interpret this finding several questions regarding the tungsten source, the tungsten influx and outflux, the ELM behaviour and the parallel flows in the SOL were addressed.

The observation of the tungsten erosion sites showed that only a small fraction of the detected change of tungsten concentration was due to a change of the tungsten source. The erosion at the source with the highest penetration factor, the ICRH limiters, was constant throughout the scanned parameter space of the gas puffing and upper triangularity. Only the divertor source showed some response to the changes in gas puffing, but even that response was only mildly influencing the main plasma tungsten concentration, due to the effective separation of the divertor plasma from the main plasma.

The tungsten influx, *i.e.* the radial transport of tungsten into the plasma, was monitored by two means. The first method measured the phase lag of a modulated tungsten signal at several locations in the main plasma and at the erosion site. In preparation of these experiments the VUV spectra of tungsten were investigated and two distinct, temperature dependent spectral features were identified. The newly added observations sites are located at the ETB, just inside the separatrix, and at the pedestal top allowing to track the tungsten signal quite closely in this important plasma region of AUG. The third observation site is located about halfway between the plasma edge and the plasma center. The modulated tungsten signal was created by applying some trace-ICRH heating with a sinusoidally modulated power pattern which lead to a sinusoidally modulated tungsten erosion at the ICRH limiters. The evaluation of the phase difference between the main plasma measurement sites and the limiter source revealed that there is no dependence of this quantity on neither gas puffing nor upper triangularity. Taking into account that simulations with the 1-D transport code STRAHL predicted the sensitivity of this method to detect changes in radial transport, the interpretation of this data was that the radial transport parameters remain unchanged by an altered gas puffing or plasma shape. This interpretation was further strengthened by secondary observations

which included the electron temperature and density. The inter-ELM radial gradients of these two quantities in the region of the ETB are not influenced by the gas injection rate or the triangularity. This finding is in agreement with the data from the phase lag evaluation, since the transport processes in the ETB are thought to be governed mainly by neoclassical transport phenomena which are strong functions of the temperature and density gradients in this region [17, 58]. Therefore it was concluded that the radial inter-ELM transport is not significantly influenced by the independent variables gas puff and triangularity and thus does not pose as an explanation of the observed tungsten behavior.

The tungsten outflux was also found to be a rather rigid quantity. This was deduced from the decay time of the tungsten concentration in the main plasma which was constant for various gas injection levels and plasma shapes. This observation means especially that the ELM frequency has no influence on the tungsten outflux from the main plasma which leads directly to the next topic: the ELM characteristics.

The ELM characteristics were studied with regard to their impact on impurities in the main plasma. It is known that ELMs expell impurities from the main plasma and the ELM induced impurity reduction inside the ETB has already been observed for carbon and other light elements [17, 18]. The expulsion process of the impurities and main ions is often regarded as diffusive, with a highly increased diffusivity for the duration of the ELM [17, 61]. However, such a diffusive expulsion model would not suffice to explain the experimental observations gathered in this work. Furthermore, it is in contradiction with the contemporary understanding of the nature of ELMs which are regarded as filamentous structures carrying away small plasma volumes from the main plasma. The expulsion of impurities from the main plasma would be the consequence, if the impurity content of the ELM filaments resembles the one of the main plasma. Since there are no diagnostic means installed at AUG to observe the tungsten loss per ELM directly, the investigation focused on the loss of electrons per ELM. The electron loss per ELM was determined to follow a $1/\nu_{ELM}$ dependency which is in agreement with previous findings [19]. Thus, on time scales larger than $1/\nu_{ELM}$, the total electron efflux from the main plasma is constant as long as the relationship above holds. These considerations were then extended to the tungsten behaviour in the main plasma by assuming that the plasma volume in the ELM filament contains the same concentration of tungsten as the main plasma. From this model follows that the ELM frequency has no impact on the tungsten concentration in the main plasma which is in good agreement with the experimental findings of this work and explains the constant tungsten decay times mentioned in the previous paragraph.

The filamentous nature of ELMs poses as a good explanation for the lacking influence of the ELM frequency on the tungsten concentration, but the question regarding the strong impact of the gas injection rate was still to be answered. This was done by establishing a simple model which balanced the tungsten influx and outflux. While the tungsten outflux was assumed to be solely caused by ELMs, the influx model was slightly more sophisticated, taking into account parallel flows in the SOL. A linear dependence between the parallel flow velocity in the SOL and the tungsten concentration emerged from this model. This prediction was then checked with a series of dedicated experiments. The spectroscopical data gathered in those experiments, even though sparse, fully supported the prediction. It was reasoned, that the SOL parallel flows indeed have a strong impact on the tungsten influx and therefore on the tungsten concentration in the main plasma. The model, however, did not cover the cause of the parallel flows in the SOL. Nevertheless, it was reasoned from the experimental data, that they are linked to the main chamber gas injection rate. Thus, the

unexpected experimental finding presented at the beginning of this chapter is fully explained by this influx/outflux model and stresses the outstanding importance of the shielding effect of the SOL.

The implications of this study are manifold. The findings of previous works, where the ELM frequency was interpreted as the main lever for impurity control [14, 78–80], might need some re-consideration. Following this line of thought, the ELM frequency should not be seen as an active impurity control mechanism for future fusion devices as long as the inverse relation between ELM size and frequency holds. Since this relation proved to be insensitive towards changes of the gas injection rate or the upper triangularity, it would be interesting to investigate other ELM control mechanisms with regard to this dependence. Some of the techniques, *e.g.* deuterium pellet injection [79], additional heating [80], application of external magnetic perturbations [81] are already quite established, but their influence on the ELM size and especially on the inter-ELM SOL flows is still to be studied. Their influence on the SOL flows are of particular interest, when investigating their impact on the impurities, since the results of this study suggest a strong link between the SOL flows and the shielding effect of the SOL.

The main plasma tungsten concentration showed a nearly inverse exponential dependence on the gas injection rate which would mean, that the shielding effect of the SOL saturates beyond a certain gas puffing level. The residual tungsten concentration found at high gas puffing levels must originate from an erosion site close to the stagnation point, where the SOL flows are weak. It would be rewarding to investigate if a proper installation of gas injection valves close to the stagnation point could reduce the tungsten influx from this delicate area by achieving a "detached" LFS limiter.

The importance of the stagnation point for the penetration capability of eroded particles should be kept in mind when choosing the wall materials in this section of the plasma vessel, since the eroded particles can easily reach the main plasma from this erosion site. Heavy elements like tungsten, nickel or iron have very benign erosion properties as compared to carbon or beryllium, but this advantage over the light elements should be carefully weighed against their radiation properties which are a major drawback for these heavy materials.

The SOL flows and their shielding effect have been shown to represent a very powerful impurity control mechanism. These flows originate from the pressure gradient between the stagnation point and the divertor, where the vacuum pumps create a particle sink. It would be interesting to investigate how the SOL flow patterns change in scenarios with a detached divertor, where a high gas injection rate is applied to the divertor and if this has any negative effect on the shielding effect of the SOL. If it should have a negative effect, then the gain of a reduced erosion in the divertor would have to be carefully balanced against the loss of a reduced SOL shielding.

Bibliography

- [1] <http://yearbook.enerdata.net>.
- [2] R. Bentley and G. Boyle, *Plasma Phys. Controlled Fusion* **31** (1989).
- [3] M. Meinshausen, N. Meinshausen, W. Hare, et al., *nature* **458** (2009).
- [4] http://www.prognos.com/fileadmin/pdf/publikationsdatenbank/130308_Prognos_Studie_Wachstumseffekte_KfW_EBS.pdf.
- [5] <http://www.eia.doe.gov/oiaf/ieo/world.html>.
- [6] http://www.bp.com/liveassets/bp_internet/globalbp/globalbp_uk_english/reports_and_publications/statistical_energy_review_2011/STAGING/local_assets/pdf/statistical_review_of_world_energy_full_report_2012.pdf.
- [7] <http://www.desertec.org>.
- [8] The Chernobyl accident: Updating of INSAG-1, Technical Report 75-INSAG-7, International Atomic Energy Agency, Vienna, Austria, 1992.
- [9] D. Fasel and M. Tran, *Fusion Eng. Design* **75–79** (2005).
- [10] <http://www.iter.org>.
- [11] R. Dux, Impurity transport in tokamak plasmas, Technical Report 10/27, Max-Planck Institut für Plasmaphysik, Garching, Germany, Dec. 2004.
- [12] <http://www.jet.efda.org>.
- [13] H.-S. Bosch and G. Hale, *Nucl. Fusion* **32**(4) (1993).
- [14] R. Dux, V. Bobkov, A. Herrmann, et al., *Journal of Nuclear Materials* **390-391**, 858–863 (2009).
- [15] R. Dux, R. Neu, A. G. Peeters, et al., *Plasma Physics and Controlled Fusion* **45**(9), 1815–1825 (2003).
- [16] R. Neu, R. Dux, A. Geier, et al., *Plasma Physics and Controlled Fusion* **44**(6), 811–826 (2002).
- [17] T. Pütterich, R. Dux, M. Janzer, et al., *Journal of Nuclear Materials* **415**(1, Supplement), S334–S339 (2011).
- [18] M. Wade, K. Burrell, J. Hogan, et al., *Phys. Plasmas* **12** (2005).

- [19] H. Urano, W. Suttrop, L. Horton, et al., *Plasma Phys. Controlled Fusion* **45** (2003).
- [20] M. Sertoli, Local Effects of ECRH on argon transport at ASDEX Upgrade, Technical Report 12056, Ludwig Maximilian Universität, Munich, Germany, July 2010.
- [21] I. Beigman, A. Pospiszczyk, G. Sergienko, et al., *Plasma Phys. Controlled Fusion* **49** (2007).
- [22] K. Behringer, H. Summers, B. Denne, et al., *Environment and Planning B* **35**(4) (2008).
- [23] T. Pütterich, Messung des Verunreinigungsflusses auf den Schutzlimitern von ASDEX Upgrade, Diplomathesis, Universität Augsburg, Germany, 2002.
- [24] M. Laengner, Eindringtiefen von injiziertem/zerstäubtem Wolfram im Randschichtplasma von TEXTOR, in Verhandlungen der Deutschen Physikalischen Gesellschaft e.V., Mar. 2012.
- [25] R. Dux, V. Bobkov, N. Fedorczak, et al., *Journal of Nuclear Materials* **363-365**, 112–116 (2007).
- [26] R. Dux, T. Pütterich, A. Janzer, et al., Flushing and Erosion of Tungsten during Edge Localised Modes, in Europhysics Conference Abstracts (CD-ROM, Proc. of the 36th EPS Conference on Plasma Physics, Sofia, Bulgaria, 2009), edited by M. Mateev and E. Benova, volume 33E of ECA, pages O–5.056, Geneva, 2009, European Physical Society.
- [27] V. Bobkov, R. Bilato, F. Braun, et al., *AIP Conference Proceedings* **933**, 83–86 (2007).
- [28] T. Pütterich, R. Neu, R. Dux, et al., *Nuclear Fusion* **50**(2), 025012 (9pp) (2010).
- [29] B. Stratton, R. Fonck, IdaK., et al., *Rev. Sci. Instrum.* **57** (1986).
- [30] H. Greiner and E. Schäffer, *Optik* **16**(5) (1959).
- [31] R. Wolf, K. Lawson, I. Coffey, et al., A Vacuum Ultra-violet Spectrometer (Double SPRED) for the Observation of the JET Divertor Plasma, Technical Report JET-P(95)34, JET Joint Undertaking, Abingdon, UK, 1995.
- [32] E. Hinnov and F. Hofmann, *J. Opt. Soc. Am.* **53**(11) (1963).
- [33] J. Klose and W. Wiese, *J. Quant. Spectrosc. Radiat. Transfer* **42**(5) (1989).
- [34] T. Pütterich, Investigations on Spectroscopic Diagnostic of High-Z Elements in Fusion Plasmas, Technical Report IPP 10/29, IPP, Garching, Germany, April 2005, PhD thesis, Universität Augsburg, 2005.
- [35] R. Isler, R. Neidigh, and R. Cowan, *Physics Letters* **63A**(3) (1977).
- [36] E. Hinnov and M. Mattioli, *Physics Letters A* **66** (1978).
- [37] R. Neu, Tungsten as a Plasma Facing Material in Fusion Devices, Technical Report 10/25, Max-Planck Institut für Plasmaphysik, Garching, Germany, Dec. 2003.
- [38] K. Asmussen, K. B. Fournier, J. M. Laming, et al., *Nuclear Fusion* **38**(7), 967–986 (1998).
- [39] E. Unger, Untersuchungen zur Absolutkalibration eines Grazing-Incidence-Spektrometers für Verunreinigungstransport an einem Fusionsexperiment, Technical Report III/187, Max-Planck Institut für Plasmaphysik, Garching, Germany, 1992.

- [40] T. Pütterich, R. Neu, R. Dux, et al., *Plasma Physics and Controlled Fusion* **50**(8), 085016 (2008).
- [41] N. Peacock, M. O'Mullane, R. Barnsley, et al., *Canadian Journal of Physics* **86** (2008).
- [42] R. Dux, R. Neu, C. F. Maggi, et al., Impurity Transport and Control in ASDEX Upgrade, in *Proc. of the 20th IAEA Conference Fusion Energy (CD-Rom)*, Vilamoura, Portugal, November 2004, volume IAEA-CSP-25/CD, pages IAEA-CN-116/EX/P6-14, Vienna, 2005, IAEA.
- [43] <http://www.cfa.harvard.edu/ampcgi/kelly.pl>.
- [44] <http://www.adas.ac.uk/>.
- [45] W. Schwanda, K. Eidmann, and M. Richardson, *Journal of X-Ray Science and Technology* **4** (1993).
- [46] B. Johnson, K. Jones, J. Cecchi, et al., *Physics Letters* **70A**(4) (1979).
- [47] M. Finkenthal, L. Huang, S. Lippmann, et al., *Physics Letters A* **127**(5) (1988).
- [48] Y.-J. Rhee and D.-H. Kwon, *International Journal of Mass Spectrometry* **271**, 45–50 (2008).
- [49] J. Yanagibayashi, T. Nakano, A. Iwamae, et al., *Nucl. Instrum. Methods Phys. Research* **623**, 741–743 (2010).
- [50] J. Clementson, P. Beiersdorfer, E. Magee, et al., *J. Phys. B: At. Mol. Opt. Phys.* **43**, 144009–8 (2010).
- [51] R. Hutton, Y. Zou, J. Reyna Almandos, et al., *Nucl. Instrum. Methods Phys. Research* **205** (2003).
- [52] M. Vilkas, Y. Ishikawa, and E. Träbert, *Phys. Rev. A* **77** (2008).
- [53] C. Biedermann, X-ray and EUV spectroscopy of highly-charged tungsten ions relevant to fusion plasmas, in *14th ADAS Workshop (Ringberg Castle, Tegernsee, Germany)*, Oct. 2009.
- [54] T. Pütterich, V. Jonauskas, R. Neu, et al., *AIP Conference Proceedings* **1545**(1), 132–142 (2013).
- [55] K. Krieger, Untersuchung des Verunreinigungstransports am Tokamak ASDEX mit spektroskopischen Methoden, Technical Report 1/257, Max-Planck Institut für Plasmaphysik, Garching, Germany, Dec. 1990.
- [56] M. Sertoli, C. Angioni, R. Dux, et al., *Plasma Physics and Controlled Fusion* **53**(3), 035024 (2011).
- [57] V. V. Bobkov, F. Braun, R. Dux, et al., *Journal of Nuclear Materials* **363-365**, 122–126 (2007).
- [58] G. Fussmann, A. Field, A. Kallenbach, et al., *Plasma Phys. Controlled Fusion* **33**(13) (1991).
- [59] R. Dux, STRAHL user manual, Technical Report 10/30, IPP, Garching, Germany, Sept. 2006.
- [60] W. Eckstein, C. Garcia-Rosales, and J. Roth, *Nucl. Instrum. Methods Phys. Res. B* **83** (1993).
- [61] R. Dux, A. Janzer, T. Pütterich, et al., *Nuclear Fusion* **51**(5), 053002 (2011).

- [62] D. Hill, *J. Nucl. Mater.* **241-243** (1997).
- [63] W. Suttrop and A. Peeters, Practical Limitations to Plasma Edge Electron Temperature Measurements by Radiometry of Electron Cyclotron Emission, Technical Report 1/306, Max-Planck Institut für Plasmaphysik, Garching, Germany, Feb. 1997.
- [64] A. Kirk, H. Wilson, and G. Counsell, *Phys. Rev. Lett.* **92**(24) (2004).
- [65] R. Sannell, A. Kirk, and N. Ben Ayed, *Plasma Phys. Controlled Fusion* **49**(9) (2007).
- [66] A. Schmid, A. Herrmann, H. W. Müller, et al., *Plasma Physics and Controlled Fusion* **50**(4), 045007 (2008).
- [67] H. Müller, J. Adamek, R. Cavazzana, et al., *Nuclear Fusion* **51**(7), 073023 (2011).
- [68] J. Boom, I. Classen, P. de Vries, et al., *Nuclear Fusion* **51**(10), 103039 (2011).
- [69] A. Pigarov, S. Krasheninnikov, B. LaBombard, et al., *J. Nucl. Mater.* **363-365** (2007).
- [70] A. Pigarov, S. Krasheninnikov, and T. Rognlien, *Phys. Plasmas* **19**(7) (2012).
- [71] R. Dux, Private communication; Max-Planck Institut für Plasmaphysik, Garching, Germany, 2010.
- [72] S. Gangadhara and B. LaBombard, *J. Nucl. Mater.* **313-316** (2003).
- [73] J. Elder, A. McLean, and P. Stangeby, *J. Nucl. Mater.* **363-365** (2007).
- [74] L. Aho-Mantila, M. I. Airila, M. Wischmeier, et al., *Physica Scripta* **T138**, 014019 (4pp) (2009).
- [75] P. Stangeby, *J. Nucl. Mater.* **415** (2011).
- [76] R. Janev and D. Reiter, *Phys. Plasmas* **9**(9) (2002).
- [77] I. Hutchinson, *Principles of Plasma Diagnostics*, Cambridge Univ. Press, 1987.
- [78] K. McCormick, M. Bessenrodt-Weberpals, E. Müller, et al., *J. Nucl. Mater.* **176 & 177** (1990).
- [79] P. T. Lang, A. Kallenbach, J. Bucalossi, et al., *Nuclear Fusion* **45**(6), 502–511 (2005).
- [80] R. Neu, R. Dux, A. Kallenbach, et al., *Nuclear Fusion* **45**(3), 209–218 (2005).
- [81] J. Canik, R. Maingi, T. Evans, et al., *Phys. Rev. Lett.* **104**(4) (2010).

Acknowledgments

The last five years were indeed challenging. On the one hand there was the very interesting work at this cutting edge research facility, on the other hand there was the wonderful experience to become a father, twice. In retrospective this combination was adventurous, but you only grow with your tasks. I would like to thank all who supported, encouraged and believed in me during these turbulent times.

First of all my direct supervisor, Dr. Ralph Dux. Thank you for being always professional, frank and direct. I have learned much from your experience and example. Thank you also for giving me the time I needed.

Thanks to Dr. Jörg Hobirk, who showed me how to play the coils of AUG so the plasma does what I want.

Prof. Dr. Hartmut Zohm for the support, the extremely interesting lectures and the possibility to do my research at the IPP.

Dr. Thomas Pütterich, for being there to answer my infinite questions and discuss my results. It was good to have somebody disagree with me.

Dr. Hans Werner Müller, who supported me with the Langmuir probe measurements and gave me some insight into the SOL physics.

The full ASDEX Upgrade team, for the great effort and assistance in each experimental session.

All my lunch mates and friends from IPP especially Marco, who introduced this habit of not talking about work at the lunch table and was a great help in the final stage of this work.

My office mates, who endured my endless fights with the computer.

Family and friends.

Sakiko, I know it was tough, but thanks for not giving up.